Multiscale Design of Polymeric Biomaterials for Reducing Epidermal Downgrowth in Percutaneous Devices

Submitted in partial fulfillment of the requirements for

the degree of

Doctor of Philosophy

in

Department of Biomedical Engineering

Pitirat Pholpabu

B.Sc., Biotechnology, Mahidol University

Carnegie Mellon University
Pittsburgh, PA

September, 2016

ACKNOWLEDGEMENTS

First and foremost, I would like to express my sincere gratitude to my advisor, Prof. Christopher J. Bettinger, for the continuous guidance and support of my Ph.D. study. Being an international student from a small country, I was overwhelmed by unfamiliar classes, cultures, languages, and community. However, he always gave me both educational and mental support to guide me through this long difficult journey. I really appreciate his expertise, kindness, and patience. I could not have imagined having a better advisor and mentor for my Ph.D. study.

I would like to extend my gratitude to my thesis committee members: Prof. Phil Campbell, Prof. Newell Washburn, and Prof. Adam Feinberg, for all of their guidance through my Ph.D. study. Their insightful comments, ideas, feedbacks, and encouragement are literally invaluable for me.

I thank my group members and my coauthors for research and academic support. I thank my officemates for making our office a fun and wonderful place. I thank my voluntary English tutor, Patrick Winschel. I acknowledge the Royal Thai Government for the full scholarship during 5 years of my Ph.D. study.

Last but not least, I would like to thank my family: my parents, my parents-in-law, and my husband, for their love, support, and encouragement during these challenging years.

ABSTRACT

Percutaneous devices are necessary tools in modern healthcare. More than one hundred fifty million percutaneous catheters have been purchased annually for various medical procedures, such as blood monitoring, urine drainage, and drug administration. However, catheter-related bloodstream infections occur in a high rate, up to 250,000 cases each year, and lead up to 25% mortality rate. One of the key causes is the skin-device incompatibility. It contributes to chronic inflammation and skin migration that generates a deep gap around the device. The lack of body outer barrier in such small area is ample for bacteria that accumulate near the insertion site to penetrate into the blood system, leading to a high risk of infections. Engineering of physical, chemical, and mechanical properties of percutaneous biomaterials is promising to improve host responses and ultimately prevent the infections. In this study, we design percutaneous biomaterials using three main approaches, i.e. surface topography, macrophage modulation, and protein-adsorption resisting materials, to attenuate the dermal downgrowth. The material in each design is characterized in in vitro environments to obtain physical, chemical, and mechanical properties, and also in in vivo milieu using a mouse model to profoundly investigate host responses. This work provides an insight of promising percutaneous material designs that reduce catheter-related complications and infections.

TABLE OF CONTENTS

LIST OF FIGURES AND ILLUSTRATIONS

CHAPTER 1

CHAPTER 2

CHAPTER 3

CHAPTER 4

CHAPTER 5

LIST OF TABLES

CHAPTER 4

CHAPTER 1 INTRODUCTION

1.1 Percutaneous Devices in Healthcare

In modern healthcare, percutaneous catheters are widely used to access patient's internal tissues and organs through dermal layers for removing of excess bodily fluids or directly feeding fluids to the blood system.[2,79] Percutaneous devices, i.e. intravascular catheters, dialysis catheters, and glucose sensors, are necessary for contemporary medical care for both adults and pediatrics.[106] The use of a catheter is to essentially avoid repeating or large surgeries that typically cause more complications, higher cost, and longer recovery time.[105] Statistically, more than 150 million percutaneous devices are purchased each year for various medical procedures. The global catheter market is expected to perpetually increase and potentially reach to nearly $42.4 billion in 2019 with a compound annual growth rate of 8.2%.[104] However, they cause nosocomial bloodstream infections between 80,000-250,000 cases annually with 12-25% mortality rate and result in up to $2.3 billion annual expense.[19,30,61,62,78,88] According to National Hospital Discharge Surveys from 1996 to 2008, catheter-related bloodstream infections also increase from 4.3 to 5.1 cases per 10,000 persons per year.[21] The bacterial accumulation around the insertion site is the main reason of these infections. The most common bacteria are human normal flora *Staphylococcus aureus*, which cause up to 75% of all catheter-related infection cases.[92] Since catheter insertion results in an injury to dermal and epidermal layers, the bacteria can access to subcutaneous layers through the open gap at the interface of skin and percutaneous devices. Proper handlings during device insertion, including use of sterile equipment,

sterile gowns, and chlorhexidine-based disinfectant solutions, are crucial that they can reduce a chance of the infections at the early period.[19] However, the catheter implantation duration usually lasts to 1-2 weeks for short-term catheters and probably more than a year for long-term catheters.[90] Thus, bacteria can continuously proliferate and accumulate in deep pockets.[86] If the interfaces lack of a stable skin barrier, only a slight move of a device while in place can result in a further penetration of bacteria into bloodstream. Bacterial invasion combined with the patient's possibly compromised immune system elevates the risk of a severe bacterial infection and sepsis (Figure 1.1).

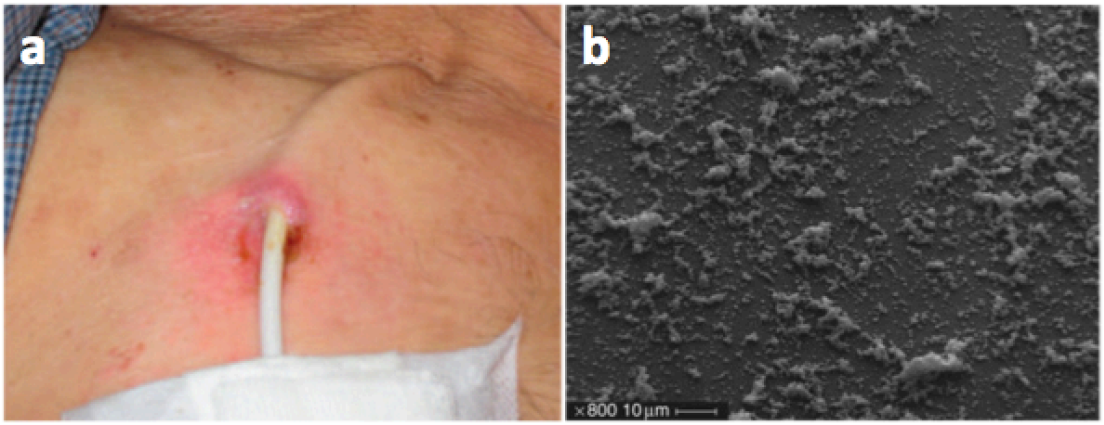

Figure 1.1 Catheter-related infection.[57] a) Exit-site infection caused from a catheter insertion. b) Micrograph of *S. aureus* biofilm on a catheter surface removed from a patient.

1.2 Tissue-Biomaterial Interaction in Percutaneous Devices

Insertion of percutaneous devices generates an injury that is resolved through a cascade of reactions resulting in dermal cell downgrowth because of incompatible physical, mechanical, and/or chemical properties between the skin and the catheter. In

wound healing, epidermal reepithelialization occurs in two phases. The first two days after wounding, keratinocytes, which are majority cells in epidermis, only migrate without proliferate to rapidly close a wound. After that, keratinocytes will strongly proliferate to fulfill the skin layer.[60] However, the insertion of percutaneous devices modifies the keratinocyte migration. Considered as an obstacle, the device is attempted to be pushed out by keratinocyte downgrowth (Figure 1.2). So, the cell migration and proliferation generate deep pockets, causing device marsupialization and implantation failure.[86] Furthermore, the deep pockets are typically a bacterial accumulation site that produces injurious reactions such as infections and fibrosis. The downgrowth might be alleviated by enhanced skin-device biointegration, tissue migration guidance, rapid dermal regeneration, anti-inflammatory agents, and protein-adsorption resistant materials. These approaches still need to be further studied.

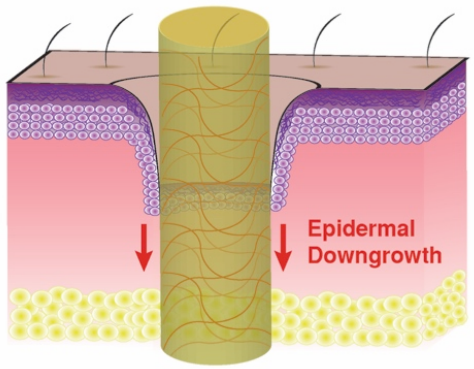

Figure 1.2 Epidermal downgrowth caused by an insertion of a percutaneous device.[75] The downgrowth is one of the host responses to a percutaneous device. It generates a deep gap around the device, leading to an accumulation of bacteria and a high risk of infections.

1.3 Current Strategies to Prevent Catheter-Related Bloodstream Infections

According to 2011 CDC Guidelines for the Prevention of Intravascular Catheter-Related Infections, an antiseptic, i.e. 70% alcohol, tincture of iodine, or chlorhexidine, is used to prepare skin before a catheter insertion to reduce bacterial accumulation on the skin and prevent infections.[70] These antiseptics are carefully chosen based upon scientific reports over the past.[13,58,64] For instance, chlorhexidin-based solutions are more widely used for skin preparation in these 10 years since they are reported to reduce catheter colonization better than alcohol-based povidone-iodine.[13,65] However, a number of catheter-related bloodstream infections still occur as previously described in Section 1.1.

Since the skin preparation with antiseptics primarily reduces infections for only short-term implants, several means have been proposed to sustainably reduce the percutaneous catheter-related infections. One of those is to incorporate antibiotics or antiseptics into a device.[39,83,84] This method does reduce the infection rate and become the treatment standard.[41,85] However, it does not effectively treat biofilms, increases drug resistance, and usually causes toxicity.[68,88] Another option that might be more desirable is to accelerate a restoration of a stable skin barrier that will prevent bacteria intrusion. Percutaneous material properties are engineered via surface compositions, surface topography, mechanical properties, and drug-controlled release.[73] These material properties are proved to be crucial in bone implants. However, researches in materials for percutaneous devices are still insufficiently developed.[73]

1.3.a Surface Topography of Percutaneous Devices

Topography of biomaterial surfaces is a crucial cue in cellular programming including cell spreading, proliferation, and migration. Engineering of micro and nano surface topography can control cell adhesion, migration, and wound closure.[20,49,71] Surface topography is promising in reduction of device-related bloodstream infections since it has been found to resist bacterium adhesion and assist skin-device integration. The surface topography is modified in various micro- and nano- features in different shapes and sizes, including micro and nanotubes, ridges and grooves, pits, and pillars.[24,81,82] For example, titanium surface with different degrees of nanorough has shown to modulate bacteria adhesion and improve osteoblast functions.[28,82] Surface topography is also bio-inspired from natural surfaces that resist microbial adhesion and integrate with other different biological tissues. Sharkskin-inspired microtopography significantly delays *S. aureus* biofilm formation for at least 7 days, compared to non-topographic control surface.[18] Surfaces of natural percutaneous devices, such as human teeth and antlers, are also studied and mimicked in synthetic materials that help tissue-device integration.[37,72,77,87] A number of researches have shown that surface topography is significant in resisting bacterial attachment; however, many research outcomes are in conflict because the chemistry of the surface that is sometimes overseen and not reported can dominate the bacterium adhesion.[24] The mechanism on how bacteria interact with the surface topography has not also elucidated yet.[80] The development of surface topography for percutaneous devices still requires more in-depth information and multidisciplinary knowledge, including immunology, biochemistry, material science and engineering, mechanical engineering, etc.

Even most studies of surface topography in percutaneous devices focus on the prevention of bacterial adhesion, several studies show that surface modification also provides suitable topographic microenvironments for cell adhesion and tissue-device integration in vivo, leading to a stable dermal barrier that protects microbial invasion.[15,32,42] A commercial STAR® Biomaterials successfully incorporate sphere-templated micropores in Figure 1.3 to implanted medical devices, resulting in enhanced biointegration, reduced foreign body response, and increased angiogenesis.[107] Regardless of polymer compositions and implant sites, porous-templated scaffolds with pore size of 30-40 μm in diameter consistently illustrate excellent healing.[10] Biological cells can essentially penetrate and regenerate inside the micropores.[10,32,95] These micropores, ~40 μm in diameter, are also found on a surface of an antler that is a natural percutaneous device, shown in Figure 1.3.[72] However, the device that completely integrates with cells and tissues requires a surgery for removal. So, this material is less suitable for patients who need to routinely replace a percutaneous device overtime.

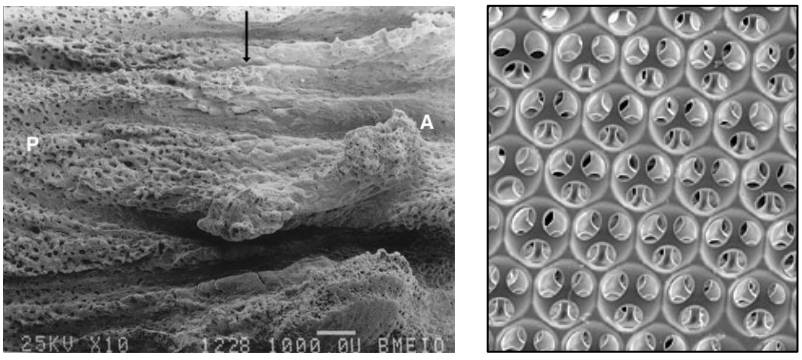

Figure 1.3 Surface topography of natural and synthetic percutaneous devices. Left: Surface topography of an antler contains two regions of different sizes of micropores, 217.22 ± 19.07 μm (P) and 40.14 ± 3.17 μm (A) in diameters.[72] Right: Commercial

sphere-templated micropores.[107] The micropores enables angiogenesis and healing while reducing foreign body response.

Microgroove-modified surfaces have been known for great controllability of cell migration for both in vitro and in vivo.[15,34,43,66,99] The cell migration rate and direction depend on the dimensions of microgrooves including wavelength, amplitude, and cell-ridge alignment.[25,45,50] Kim *et al.* reported that an array of 550 nm ridges spaced with 1100 nm grooves yielded the highest fibroblast migration speed, compared to 550:550 and 550:2750 ridge:groove spatial ratio.[50] The microgroove has also been incorporated in titanium percutaneous devices and found to significantly reduce epithelium recession.[9,15,51] The microgroove is widely used for skin healing as it resembles natural ECM networks.[100] Directional migration occurs as lamellipodium is regulated to form in a curtain direction by surface topography, as shown in Figure 1.4.[75] Since the microgroove primarily controls the cell migration, not the tissue-device integration, the microgrooved surface is promising in reducing epithelial downgrowth in percutaneous devices without a permanent skin sealing. It is considered more suitable for catheters that need a routine replacement, compared to porous materials that generate a long-term bio-integration. We hypothesize that the downward migration of the percutaneous device-inserted dermal tissue can be obstructed and delayed by microgrooves that align perpendicular to the downward migration direction, leading to a reduction of the epidermal downgrowth. In this thesis, we have studied microgrooves in both in vitro and in vivo environments as a way to control cell morphology and dermal migration, as detailed in Chapter 2 and 3.

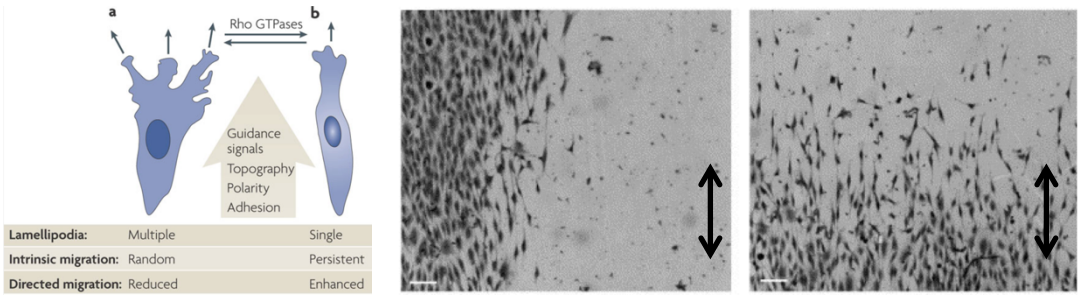

Figure 1.4 Controllable cell migration on surface topography. Left: A schematic showing the formation of lamellipodium that is controlled by surface topography. Restricted lateral lamellipodium formation results in directionally persistent intrinsic cell migration and enhanced directed migration.[75] Right: Optical micrographs of a cell population on microgrooves taken perpendicular and parallel and to the groove direction (indicated by arrows), respectively. Bar=100 μm.[55]

1.3.b Skin-Device Matched Mechanical Properties

One of prevailing strategies for tissue-device integration at the interface is matching the modulus of the material with the modulus of the local tissue.[31,38] Significant mechanical mismatch between materials and the surrounding tissue can lead to increased and chronic inflammatory responses.[29] This host response is considered a failure mode, called 'avulsion' proposed by VanRecum.[86] Avulsion occurs when mechanical difference causes a tear or break of skin, leading to detachment of skin from the device. Repeating cycles of attachment and detachment induce scarring, chronic wound, and insufficient seal.[86] The ideal biomaterial for a percutaneous device would match the mechanical properties of the dermis and epidermis ranging from 2 to 600 kPa.[48] Most of current polymeric biomaterials are made of thermoplastic polyesters such as poly(lactic acid) (PLA), poly(glycolic acid) (PGA), polycaprolactone (PCL) and

their blends or copolymers[89]; however, typically, they are not compatible with mechanical properties of biological tissues.

Elastomers or elastic polymers are a class of materials that exhibit a rapid and large reversible strain in response to a stress, typically having by low Young's modulus and high failure strain compared to other classes of materials.[53] Elastomers for medical devices has been developed since around the mid of 1890s and brought a great research progress since presented in a symposium in 1981.[16,53] They have been used in various implantable devices such as cardiovascular devices, prosthetic devices, catheters, transdermal therapeutics, and orthodontics materials.[16] Researchers successfully show that compliant implants have more biocompatibility to brain tissues by significantly reducing scar formation and inflammation in both in vitro and in vivo environments.[35,67] Nguyen *et al.* implanted stiff and compliant materials in rat cortex and found that the compliant implant can reduce neuro-inflammatory response from 2-16 weeks, as shown in Figure 1.5.[67] According to the fact that modulus matching significantly improves biocompatibility in brain implants, we speculate that biomaterials that match the modulus of skin will reduce local inflammation occurring in percutaneous device. Our group has successfully synthesized poly(glycerol-*co*-sebacate)-cinnamate (PGS-CinA) with 50.5 to 152.1 kPa range of modulus that matches the skin modulus.[103] PGS-CinA networks are suitable for biological integration because of their properties in biocompatibility, biodegradability, remodeling, and intrinsically cell adhesiveness.[4,5,103] Hence, PGS-CinA elastomers are one of promising biomaterials for use in next-generation percutaneous interfaces.

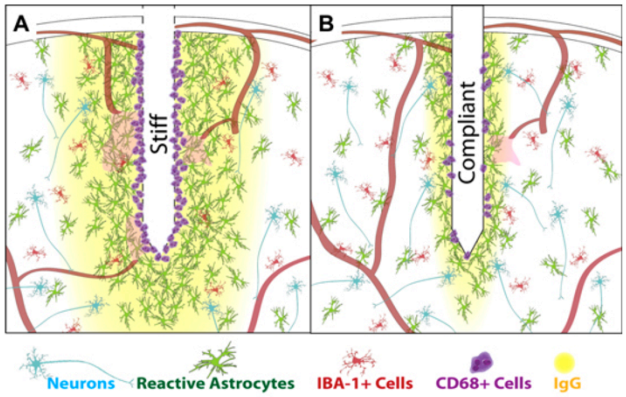

Figure 1.5 A schematic showing rat brain tissues in response to brain implants with different stiffness.[67] The stiff implant (A) induces more scar formation (green) and inflammatory cells (purple), compared to the compliant implant (B). The implant modulus dominates the host response during chronic inflammation.

1.3.c Controlling of Local Inflammation

An implantation basically injures vascularized connective tissue, initiating blood-material interactions. Thrombus or blood clot formation on the surface of a biomaterial is related to the well-known Vroman effect of protein adsorption. Initial proteins that adsorb on the material surface are replaced with fibrinogen and other proteins that have higher affinity to the surface. These proteins, known as the provisional matrix, present mitogens, chemoattractants, cytokines, growth factors, and other bioactive agents to recruit and modulate related inflammatory cells.[1] During the first several days following an injury, the predominant cell type is generally neutrophils. They are then replaced by monocytes and macrophages that basically govern the phase of wound healing: inflammation, proliferation, and maturation.

Basic ideal properties of biomaterials include inertness, unreactiveness, and non-toxicity in a host; however, current available biomaterials can sequentially cause acute and chronic inflammations, which occur following the initial blood/material interactions.[8,93,98] The acute and chronic inflammations are indicated by an accumulation of polymorphonuclear leukocytes or neutrophils, and mononuclear cells, respectively. The acute inflammation with biomaterials usually resolves in less than one week. If the inflammation lasts longer than that, it is considered the chronic inflammation.[1] The chronic inflammation lead to adverse effects such as an oxidative degradation of a biomaterial, a contraction of an implanted site, and an enzymatic attack to an implant. These biological and mechanical stresses might break or degrade the implant to reactive products that cause toxicity.[93] The chronic inflammation caused from an implant near skin tissue can also develop to skin cancer.[23] Limiting inflammatory process around an implant will help avoiding those adverse events and supporting tissue-device integration.

One of the key components that govern inflammatory processes is host macrophages. In vivo, macrophages are derived from monocytes circulating in bloodstream in the response of foreign bodies. Macrophage phenotypes are loosely classified into pro-inflammatory (M1) or wound healing (M2) phenotypes[54], mirroring the Th1 and Th2 immune responses.[36,59] M2 macrophages are further divided into different polarizations. M2a and M2b macrophages can initiate type II inflammation while M2c cells are responsible for inflammatory suppression, matrix remodeling, and tissue repair.[59] Macrophage phenotype is defined by many micro-environmental stimuli, including cytokines. For example, in the context of biomaterials, macrophages respond

to exogenous IL-1β, IL-6, and TNF-α by adopting a pro-inflammatory M1 phenotype, while exogenous IL-10 activates an M2c phenotype that attenuates inflammation, promotes matrix remodeling, and resolves late stage wound healing.[59] Cao *et al*. reports a phenotypic change of macrophages during kidney injury, as shown in Figure 1.6.[12] In acute kidney disease, macrophages firstly polarize to M1 phenotype by multiple pro-inflammatory cytokines. Those macrophages subsequently switch to M2 phenotype to resolve the inflammation. In contrast to macrophages in the acute kidney disease, M1 macrophages in the chronic one are persistent and seldom polarize to M2 phenotype. The persistent M1 macrophages cause chronic inflammation and a formation of excess fibrous connective tissue, as so called fibrosis.[12] Altogether, we hypothesize that biasing macrophage phenotypes to M2c polarities at the interface of implanted materials is promising in promoting tissue regeneration and skin-device integration, and also reducing chronic inflammation.[22,47]

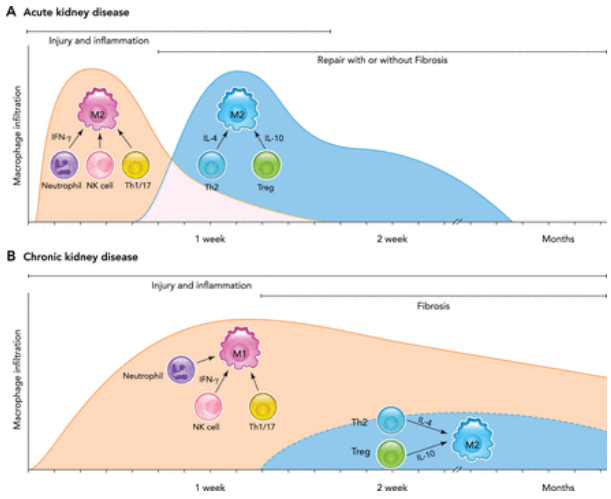

Figure 1.6 Macrophage phenotypes in acute and chronic tissue damages.[12] A schematic shows different cell density profiles of macrophage phenotypes in acute and

chronic damaged kidney. It is suggested that the higher M2 polarization in acute phase assists in resolving the inflammation and does not further cause fibrosis.

In order to modulate the host immune, delivery of anti-inflammatory agents is one of the effective strategies that can reduce inflammation and its consequently adverse effects. Even though administration of an anti-inflammatory drug can be easily done using an oral route, the concentration might not be enough for controlling inflammation at a specific local site, and side effects might occur.[7] Targeting local inflammation is then more effective to improve tissue-device interactions. Current anti-inflammatory drugs to treat local inflammation include signaling peptides and proteins, such as dexamethasone (DEX), heparin, alpha melanocyte-stimulating hormone (α-MSH), curcumin, vitamin E, etc.[7] The drug might variously target on modulation of inflammatory mechanisms or cells, i.e. neutrophils, lymphocytes, and macrophages. For example, DEX supports macrophage polarization toward anti-inflammatory phenotype and reduce pro-inflammatory cytokines, while heparin suppresses superoxide generation in neutrophils.[7,96] In order to retain the effectiveness of the modulating molecule, a material needs a system that can prolong active drug concentration at the implantation site. Several reports have conducted immobilization or encapsulation of a drug in a matrix to locally present these molecules to nearby immune cells. For example, sustained release of anti-inflammatory drug prednisolone from chitosan gel beads can reduce inflammatory responses at day 3, compared to the carriers without drug.[52] Although current local drug delivery systems successfully modulate acute

inflammation, new designs and strategies will be critical to extend the in vivo lifetime and performance of biomaterials.

1.3.d Anti-Fouling Surface Coatings for Percutaneous Devices

One of the major strategies for a design of biomaterial surfaces is to prevent fouling from proteins, cells, and bacteria.[3] The strategy includes an engineering of self-assembled mono- or multilayers, polymer brushes, surface grafting, zwitterionic polymers, hydrogels, etc. on a biomaterial surface.[11] The surface modification mostly focuses on the early step of host responses to biomaterials. Essentially, protein adsorption happens on a biomaterial surface right after an implant comes in contact with blood that leaks from destroyed vasculature system. The adsorbed protein anchors on the surface for cell attachment and induces chemotaxis for inflammatory cells.[10] Anti-fouling materials aim to prevent this initial process by creating a thermodynamically unfavorable surface for the protein adsorption.[3] When the initial process of protein adsorption cannot adsorb on the surface, the typical following host responses to foreign bodies, such as infiltration of immune cells, formation of foreign body giant cells (FBGC), and fibrosis, are consequently dampened or omitted.[3,10] This type of material can be referred as a stealth material because it can hide itself from the host immune recognition system. However, most of the currently used anti-fouling biomaterials cannot completely avoid the foreign body response. There are several reports showing foreign body reactions that occur to implants made of many biomaterials including polyurethane, silicone rubber, polyethylene, poly(methyl methacrylate), poly(2-hydroxyethyl methacrylate) (PHEMA), and even poly(ethylene glycol) (PEG), which is

the most widely used anti-fouling material.[46] PEG has been known and used to reduce protein adsorption and cell attachment for over decades. However, PEG does not well resist small protein adsorption, such as albumin (67 kD) and myoglobin (16 kD).[63] PEG is also found to degrade in the presence of oxygen and transition metal ions, leading to instability in long-term implantation in vivo.[14,91]

In view of percutaneous devices, anti-fouling surface modification has been continuously gained a great interest in these few decades. This is due to the fact that part of the percutaneous devices has to be exposed to the external environment, so there is higher risk of infections, compared to other implants. The anti-fouling surface not only resist host protein adsorption, but is also effective in reducing microbial attachment and preventing thrombosis, one of the key concerns in catheters.[26,56,69,94,101] Like other medical devices, the development of catheter surface initially focus on using hydrophilic polymers, mostly PEG-based materials, as an anti-fouling coating.[27,40] However, as described earlier, the hydrophilic coating cannot completely repel protein adsorption, and the anti-fouling property of PEG-based coating does not provide a long-term stability.[14,74] In order to resist host responses and infections, anti-fouling coating of percutaneous devices still need more understanding in material-host interactions and an improvement of a material design.

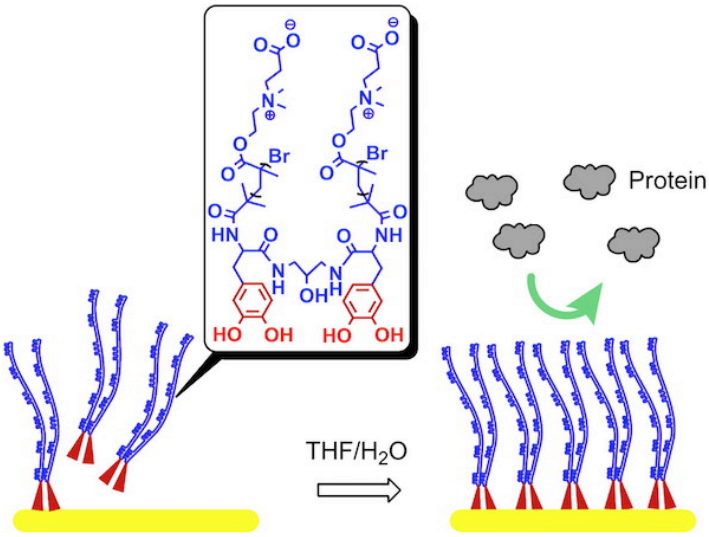

Figure 1.7 Zwitterionic coating for resisting non-specific protein adsorption (adapted from the original figure).[33] The schematic shows a design of an ultra-low fouling surface using zwitterionic polymers, providing resistance of non-specific protein adsorption from human serum and plasma.

Recently, a class of zwitterionic polymers has become a major material that provides anti-fouling property. Jiang *et al.* has published many research articles, reporting a stable anti-fouling property of zwitterionic materials, such as poly(carboxybetaine methacrylate) (pCBMA) and poly(sulfobetaine methacrylate) (pSBMA), and uses in various medical applications.[17,44,102] The zwitterionic surface is found to adsorb non-specific protein adsorption from undiluted human plasma only at 6 ng/cm^2.[6] Even thought the adsorbed protein concentration is larger than 5 ng/cm^2 adsorbed fibrinogen on biomaterial surface that is recommended to completely avoid platelet adhesion, zwitterionic materials that are subcutaneously implanted in mice can resist capsule formation for at least 3 months.[102] Research results from Wang *et al.* and Vaterrodt *et al.* also support that zwitterionic coatings can reduce bacterial attachment

and activities on silicone-based catheters in vitro (Figure 1.8).[97,101] Since zwitterionic coatings resist fibrosis and bacterial adhesion both, we herein propose that zwitterionic coatings will be suitable for modification of percutaneous devices to reduce the main medical complications: epidermal downgrowth and bloodstream infections. The use of zwitterionic coatings in percutaneous devices has not reported, so it still needs to be further studied especially in an in vivo environment that has more complexity than in vitro experiments and better provides insight knowledge.

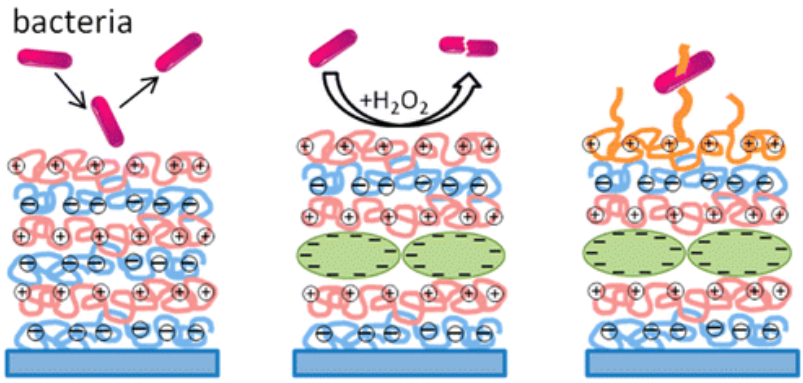

Figure 1.8 Zwitterionic coating with anti-bacterial substances.[97] Recently, Vaterrodt *et al*. design antifouling and antibacterial multifunctional polyzwitterion/enzyme coating on PDMS. The multilayer film reduces bacterial adhesion down to 40% relatively to uncoated PDMS and kills bacteria that come in contact. The results confirm the anti-fouling and functionalizable properties of zwitterionic polymers.

1.4 Thesis Objectives

The primary goal of this thesis is to design a percutaneous device that decreases dermal downgrowth, accelerates wound healing processes, and generates stable regenerative integration that will ultimately reduce bloodstream infections. We

deliberately generate and investigate three viable engineering designs of percutaneous devices. Focusing on different aspects of host-device interactions, the devices were fabricated with modified surface topography, drug release for macrophage modulation, or anti-fouling surface. In vitro device characterization describes physical, mechanical, and chemical properties that provide in-depth characteristics of each design. A mouse model is also used to observe epidermal downgrowth and other related host responses. This thesis will advance knowledge as well as technology for developing percutaneous devices.

References:

1. Anderson, J. M., A. Rodriguez, and D. T. Chang. Foreign Body Reaction To Biomaterials. *Semin. Immunol.* 20:86–100, 2008.
2. van Baal, M. C., H. C. van Santvoort, T. L. Bollen, O. J. Bakker, M. G. Besselink, and H. G. Gooszen. Systematic review of percutaneous catheter drainage as primary treatment for necrotizing pancreatitis. *Br. J. Surg.* 98:18–27, 2011.
3. Banerjee, I., R. C. Pangule, and R. S. Kane. Antifouling Coatings: Recent Developments in the Design of Surfaces That Prevent Fouling by Proteins, Bacteria, and Marine Organisms. *Adv. Mater.* 23:690–718, 2011.
4. Bettinger, C. J., J. P. Bruggeman, J. T. Borenstein, and R. S. Langer. Amino alcohol-based degradable poly(ester amide) elastomers. *Biomaterials* 29:2315–25, 2008.
5. Bettinger, C. J., K. M. Kulig, J. P. Vacanti, R. Langer, and J. T. Borenstein. Nanofabricated collagen-inspired synthetic elastomers for primary rat hepatocyte culture. *Tissue Eng. Part A* 15:1321–9, 2009.
6. Brault, N. D., A. D. White, A. D. Taylor, Q. Yu, and S. Jiang. Directly functionalizable surface platform for protein arrays in undiluted human blood plasma. *Anal. Chem.* 85:1447–1453, 2013.
7. Bridges, A. W., and A. J. García. Anti-Inflammatory Polymeric Coatings for Implantable Biomaterials and Devices. *J. Diabetes Sci. Technol.* 2:984–994, 2008.
8. Brown, B. N., and S. F. Badylak. Expanded applications, shifting paradigms and an improved understanding of host–biomaterial interactions. *Acta Biomater.* 9:4948–4955, 2013.
9. Brunette, D. M., and B. Chehroudi. The effects of the surface topography of micromachined titanium substrata on cell behavior in vitro and in vivo. *J. Biomech. Eng.* 121:49–57, 1999.
10. Bryers, J. D., C. M. Giachelli, and B. D. Ratner. Engineering biomaterials to integrate and heal: the biocompatibility paradigm shifts. *Biotechnol. Bioeng.* 109:1898–1911, 2012.
11. Campoccia, D., L. Montanaro, and C. R. Arciola. A review of the biomaterials technologies for infection-resistant surfaces. *Biomaterials* 34:8533–8554, 2013.
12. Cao, Q., D. C. H. Harris, and Y. Wang. Macrophages in Kidney Injury, Inflammation, and Fibrosis. *Physiology* 30:183–194, 2015.
13. Chaiyakunapruk, N., D. L. Veenstra, B. A. Lipsky, S. D. Sullivan, and S. Saint. Vascular Catheter Site Care: The Clinical and Economic Benefits of Chlorhexidine Gluconate Compared with Povidone Iodine. *Clin. Infect. Dis.* 37:764–771, 2003.

14. Chang, Y., S.-C. Liao, A. Higuchi, R.-C. Ruaan, C.-W. Chu, and W.-Y. Chen. A highly stable nonbiofouling surface with well-packed grafted zwitterionic polysulfobetaine for plasma protein repulsion. *Langmuir ACS J. Surf. Colloids* 24:5453–5458, 2008.
15. Chehroudi, B., and D. M. Brunette. Subcutaneous microfabricated surfaces inhibit epithelial recession and promote long-term survival of percutaneous implants. *Biomaterials* 23:229–237, 2002.
16. Chen, Q., S. Liang, and G. A. Thouas. Elastomeric biomaterials for tissue engineering. *Prog. Polym. Sci.* 38:584–671, 2013.
17. Cheng, G., G. Li, H. Xue, S. Chen, J. D. Bryers, and S. Jiang. Zwitterionic carboxybetaine polymer surfaces and their resistance to long-term biofilm formation. *Biomaterials* 30:5234–5240, 2009.
18. Chung, K. K., J. F. Schumacher, E. M. Sampson, R. A. Burne, P. J. Antonelli, and A. B. Brennan. Impact of engineered surface microtopography on biofilm formation of Staphylococcus aureus. *Biointerphases* 2:89–94, 2007.
19. Crnich, C. J., and D. G. Maki. The promise of novel technology for the prevention of intravascular device-related bloodstream infection. I. Pathogenesis and short-term devices. *Clin. Infect. Dis. Off. Publ. Infect. Dis. Soc. Am.* 34:1232–1242, 2002.
20. Dalby, M. J., D. Giannaras, M. O. Riehle, N. Gadegaard, S. Affrossman, and A. S. G. Curtis. Rapid fibroblast adhesion to 27 nm high polymer demixed nano-topography. *Biomaterials* 25:77–83, 2004.
21. Daniels, K. R., and C. R. Frei. The United States' progress toward eliminating catheter-related bloodstream infections: Incidence, mortality, and hospital length of stay from 1996 to 2008. *Am. J. Infect. Control* 41:118–121, 2013.
22. David, S., and A. Kroner. Repertoire of microglial and macrophage responses after spinal cord injury. *Nat. Rev. Neurosci.* 12:388–399, 2011.
23. Demehri, S., T. J. Cunningham, E. A. Hurst, A. Schaffer, D. M. Sheinbein, and W. M. Yokoyama. Chronic allergic contact dermatitis promotes skin cancer. *J. Clin. Invest.* 124:5037–5041, 2014.
24. Desrousseaux, C., V. Sautou, S. Descamps, and O. Traoré. Modification of the surfaces of medical devices to prevent microbial adhesion and biofilm formation. *J. Hosp. Infect.* 85:87–93, 2013.
25. Diehl, K. A., J. D. Foley, P. F. Nealey, and C. J. Murphy. Nanoscale topography modulates corneal epithelial cell migration. *J. Biomed. Mater. Res. A* 75:603–611, 2005.
26. Ding, X., C. Yang, T. P. Lim, L. Y. Hsu, A. C. Engler, J. L. Hedrick, and Y.-Y. Yang. Antibacterial and antifouling catheter coatings using surface grafted PEG-b-cationic polycarbonate diblock copolymers. *Biomaterials* 33:6593–6603, 2012.
27. Du, Y. J., J. L. Brash, G. McClung, L. R. Berry, P. Klement, and A. K. C. Chan. Protein adsorption on polyurethane catheters modified with a novel antithrombin-heparin covalent complex. *J. Biomed. Mater. Res. A* 80A:216–225, 2007.
28. Ercan, B., K. M. Kummer, K. M. Tarquinio, and T. J. Webster. Decreased Staphylococcus aureus biofilm growth on anodized nanotubular titanium and the effect of electrical stimulation. *Acta Biomater.* 7:3003–3012, 2011.
29. Fleckman, P., and J. E. Olerud. Models for the histologic study of the skin interface with percutaneous biomaterials. *Biomed. Mater. Bristol Engl.* 3:34006, 2008.
30. Frasca, D., C. Dahyot-Fizelier, and O. Mimoz. Prevention of central venous catheter-related infection in the intensive care unit. *Crit. Care Lond. Engl.* 14:212, 2010.
31. Frey, M. T., and Y. Wang. A photo-modulatable material for probing cellular responses to substrate rigidity. *Soft Matter* 5:1918–1924, 2009.
32. Fukano, Y., M. L. Usui, R. A. Underwood, S. Isenhath, A. J. Marshall, K. D. Hauch, B. D. Ratner, J. E. Olerud, and P. Fleckman. Epidermal and dermal integration into sphere-templated porous poly(2-hydroxyethyl methacrylate) implants in mice. *J. Biomed. Mater. Res. A* 94A:1172–1186, 2010.
33. Gao, C., G. Li, H. Xue, W. Yang, F. Zhang, and S. Jiang. Functionalizable and ultra-low fouling zwitterionic surfaces via adhesive mussel mimetic linkages. *Biomaterials* 31:1486–1492, 2010.
34. Garland, S. P., C. T. McKee, Y.-R. Chang, V. K. Raghunathan, P. Russell, and C. J. Murphy. A cell culture substrate with biologically relevant size-scale topography and compliance of the basement membrane. *Langmuir ACS J. Surf. Colloids* 30:2101–2108, 2014.
35. Georges, P. C., W. J. Miller, D. F. Meaney, E. S. Sawyer, and P. A. Janmey. Matrices with Compliance Comparable to that of Brain Tissue Select Neuronal over Glial Growth in Mixed Cortical Cultures. *Biophys. J.* 90:3012–3018, 2006.
36. Gordon, S. Alternative activation of macrophages. *Nat. Rev. Immunol.* 3:23–35, 2003.

37. Grosse-Siestrup, C., and K. Affeld. Design criteria for percutaneous devices. *J. Biomed. Mater. Res.* 18:357–382, 1984.
38. Gunatillake, P. A., and R. Adhikari. Biodegradable synthetic polymers for tissue engineering. *Eur. Cell. Mater.* 5:1–16; discussion 16, 2003.
39. Hanna, H. A., I. I. Raad, B. Hackett, S. K. Wallace, K. J. Price, D. E. Coyle, and C. L. Parmley. ANtibiotic-impregnated catheters associated with significant decrease in nosocomial and multidrug-resistant bacteremias in critically ill patients*. *Chest* 124:1030–1038, 2003.
40. Hazer, D. B., M. Mut, N. Dinçer, Z. Saribas, B. Hazer, and T. Özgen. The efficacy of silver-embedded polypropylene-grafted polyethylene glycol-coated ventricular catheters on prevention of shunt catheter infection in rats. *Childs Nerv. Syst.* 28:839–846, 2012.
41. Hockenhull, J. C., K. M. Dwan, G. W. Smith, C. L. Gamble, A. Boland, T. J. Walley, and R. C. Dickson. The clinical effectiveness of central venous catheters treated with anti-infective agents in preventing catheter-related bloodstream infections: a systematic review. *Crit. Care Med.* 37:702–712, 2009.
42. Isackson, D., K. J. Cook, L. D. McGill, and K. N. Bachus. Mesenchymal stem cells increase collagen infiltration and improve wound healing response to porous titanium percutaneous implants. *Med. Eng. Phys.* 35:743–753, 2013.
43. Jeon, H., H. Hidai, D. J. Hwang, K. E. Healy, and C. P. Grigoropoulos. The effect of micronscale anisotropic cross patterns on fibroblast migration. *Biomaterials* 31:4286–4295, 2010.
44. Jiang, S., and Z. Cao. Ultralow-Fouling, Functionalizable, and Hydrolyzable Zwitterionic Materials and Their Derivatives for Biological Applications. *Adv. Mater.* 22:920–932, 2010.
45. Karuri, N. W., S. Liliensiek, A. I. Teixeira, G. Abrams, S. Campbell, P. F. Nealey, and C. J. Murphy. Biological length scale topography enhances cell-substratum adhesion of human corneal epithelial cells. *J. Cell Sci.* 117:3153–3164, 2004.
46. Kenneth Ward, W. A review of the foreign-body response to subcutaneously-implanted devices: the role of macrophages and cytokines in biofouling and fibrosis. *J. Diabetes Sci. Technol.* 2:768–777, 2008.
47. Kharraz, Y., J. Guerra, C. J. Mann, A. L. Serrano, Mu&#xf1, oz-C&#xe1, and P. Noves. Macrophage Plasticity and the Role of Inflammation in Skeletal Muscle Repair. *Mediators Inflamm.* 2013:e491497, 2013.
48. Kim, D.-H., N. Lu, R. Ma, Y.-S. Kim, R.-H. Kim, S. Wang, J. Wu, S. M. Won, H. Tao, A. Islam, K. J. Yu, T. Kim, R. Chowdhury, M. Ying, L. Xu, M. Li, H.-J. Chung, H. Keum, M. McCormick, P. Liu, Y.-W. Zhang, F. G. Omenetto, Y. Huang, T. Coleman, and J. A. Rogers. Epidermal electronics. *Science* 333:838–43, 2011.
49. Kim, H. N., Y. Hong, M. S. Kim, S. M. Kim, and K.-Y. Suh. Effect of orientation and density of nanotopography in dermal wound healing. *Biomaterials* 33:8782–92, 2012.
50. Kim, H. N., Y. Hong, M. S. Kim, S. M. Kim, and K.-Y. Suh. Effect of orientation and density of nanotopography in dermal wound healing. *Biomaterials* 33:8782–8792, 2012.
51. Klymov, A., J. te Riet, P. Mulder, J. G. E. Gardeniers, J. A. Jansen, and X. F. Walboomers. Nanometer-grooved topography stimulates trabecular bone regeneration around a concave implant in a rat femoral medulla model. *Nanomedicine Nanotechnol. Biol. Med.* .doi:10.1016/j.nano.2016.06.013
52. Kofuji, K., H. Akamine, C. J. Qian, K. Watanabe, Y. Togan, M. Nishimura, I. Sugiyama, Y. Murata, and S. Kawashima. Therapeutic efficacy of sustained drug release from chitosan gel on local inflammation. *Int. J. Pharm.* 272:65–78, 2004.
53. Lal, J., and J. E. Mark. Advances in Elastomers and Rubber Elasticity. 1986.at <http://link.springer.com/openurl?genre=book&isbn=978-1-4757-1438-8>
54. Laskin, D. L. Macrophages and inflammatory mediators in chemical toxicity: a battle of forces. *Chem. Res. Toxicol.* 22:1376–1385, 2009.
55. Lenhert, S., M.-B. Meier, U. Meyer, L. Chi, and H. P. Wiesmann. Osteoblast alignment, elongation and migration on grooved polystyrene surfaces patterned by Langmuir–Blodgett lithography. *Biomaterials* 26:563–570, 2005.
56. Leslie, D. C., A. Waterhouse, J. B. Berthet, T. M. Valentin, A. L. Watters, A. Jain, P. Kim, B. D. Hatton, A. Nedder, K. Donovan, E. H. Super, C. Howell, C. P. Johnson, T. L. Vu, D. E. Bolgen, S. Rifai, A. R. Hansen, M. Aizenberg, M. Super, J. Aizenberg, and D. E. Ingber. A bioinspired omniphobic surface coating on medical devices prevents thrombosis and biofouling. *Nat. Biotechnol.* 32:1134–1140, 2014.

57. Lok, C. E., and M. H. Mokrzycki. Prevention and management of catheter-related infection in hemodialysis patients. *Kidney Int.* 79:587–598, 2011.
58. Maki, D. G., M. Ringer, and C. J. Alvarado. Prospective randomised trial of povidone-iodine, alcohol, and chlorhexidine for prevention of infection associated with central venous and arterial catheters. *Lancet Lond. Engl.* 338:339–343, 1991.
59. Mantovani, A., A. Sica, S. Sozzani, P. Allavena, A. Vecchi, and M. Locati. The chemokine system in diverse forms of macrophage activation and polarization. *Trends Immunol.* 25:677–686, 2004.
60. Marks, R., B. Bhogal, and R. P. R. Dawber. The migratory property of epidermis in vitro. *Arch. Für Dermatol. Forsch.* 243:209–220, 1972.
61. Mermel, L. A. Prevention of intravascular catheter-related infections. *Ann. Intern. Med.* 132:391–402, 2000.
62. Mermel, L. A., B. M. Farr, R. J. Sherertz, I. I. Raad, N. O'Grady, J. S. Harris, and D. E. Craven. Guidelines for the management of intravascular catheter-related infections. *Clin. Infect. Dis. Off. Publ. Infect. Dis. Soc. Am.* 32:1249–72, 2001.
63. Michel, R., S. Pasche, M. Textor, and D. G. Castner. Influence of PEG Architecture on Protein Adsorption and Conformation. *Langmuir* 21:12327–12332, 2005.
64. Mimoz, O., L. Pieroni, C. Lawrence, A. Edouard, Y. Costa, K. Samii, and C. Brun-Buisson. Prospective, randomized trial of two antiseptic solutions for prevention of central venous or arterial catheter colonization and infection in intensive care unit patients. *Crit. Care Med.* 24:1818–1823, 1996.
65. Mimoz O, Villeminey S, Ragot S, and et al. CHlorhexidine-based antiseptic solution vs alcohol-based povidone-iodine for central venous catheter care. *Arch. Intern. Med.* 167:2066–2072, 2007.
66. Miyoshi, H., T. Adachi, J. Ju, S. M. Lee, D. J. Cho, J. S. Ko, G. Uchida, and Y. Yamagata. Characteristics of motility-based filtering of adherent cells on microgrooved surfaces. *Biomaterials* 33:395–401, 2012.
67. Nguyen, J. K., D. J. Park, J. L. Skousen, A. E. Hess-Dunning, D. J. Tyler, S. J. Rowan, C. Weder, and J. R. Capadona. Mechanically-compliant intracortical implants reduce the neuroinflammatory response. *J. Neural Eng.* 11:56014, 2014.
68. Nickel, J. C., J. B. Wright, I. Ruseska, T. J. Marrie, C. Whitfield, and J. W. Costerton. Antibiotic resistance ofPseudomonas aeruginosa colonizing a urinary catheter in vitro. *Eur. J. Clin. Microbiol.* 4:213–218.
69. Noimark, S., C. W. Dunnill, M. Wilson, and I. P. Parkin. The role of surfaces in catheter-associated infections. *Chem. Soc. Rev.* 38:3435–3448, 2009.
70. O'Grady, N. P., M. Alexander, L. A. Burns, E. P. Dellinger, J. Garland, S. O. Heard, P. A. Lipsett, H. Masur, L. A. Mermel, M. L. Pearson, I. I. Raad, A. G. Randolph, M. E. Rupp, and S. Saint. Guidelines for the prevention of intravascular catheter-related infections. *Am. J. Infect. Control* 39:S1–S34, 2011.
71. Patel, S., K. Kurpinski, R. Quigley, H. Gao, B. S. Hsiao, M.-M. Poo, and S. Li. Bioactive Nanofibers: Synergistic Effects of Nanotopography and Chemical Signaling on Cell Guidance. *Nano Lett.* 7:2122–2128, 2007.
72. Pendegrass, C. J., A. E. Goodship, J. S. Price, and G. W. Blunn. Nature's answer to breaching the skin barrier: an innovative development for amputees. *J. Anat.* 209:59–67, 2006.
73. Peramo, A., and C. L. Marcelo. Bioengineering the Skin–Implant Interface: The Use of Regenerative Therapies in Implanted Devices. *Ann. Biomed. Eng.* 38:2013–2031, 2010.
74. Perrino, C., S. Lee, S. W. Choi, A. Maruyama, and N. D. Spencer. A biomimetic alternative to poly(ethylene glycol) as an antifouling coating: resistance to nonspecific protein adsorption of poly(L-lysine)-graft-dextran. *Langmuir ACS J. Surf. Colloids* 24:8850–8856, 2008.
75. Petrie, R. J., A. D. Doyle, and K. M. Yamada. Random versus directionally persistent cell migration. *Nat. Rev. Mol. Cell Biol.* 10:538–549, 2009.
76. Pholpabu, P., S. S. Yerneni, C. Zhu, P. G. Campbell, and C. J. Bettinger. Controlled Release of Small Molecules from Elastomers for Reducing Epidermal Downgrowth in Percutaneous Devices. *ACS Biomater. Sci. Eng.* , 2016.doi:10.1021/acsbiomaterials.6b00192
77. Pitkin, M. Design features of implants for direct skeletal attachment of limb prostheses. *J. Biomed. Mater. Res. A* 101:3339–3348, 2013.
78. Pittet, D., D. Tarara, and R. P. Wenzel. Nosocomial bloodstream infection in critically ill patients. Excess length of stay, extra costs, and attributable mortality. *JAMA J. Am. Med. Assoc.* 271:1598–1601, 1994.

79. Pittiruti, M., H. Hamilton, R. Biffi, J. MacFie, M. Pertkiewicz, and ESPEN. ESPEN Guidelines on Parenteral Nutrition: central venous catheters (access, care, diagnosis and therapy of complications). *Clin. Nutr. Edinb. Scotl.* 28:365–377, 2009.
80. Ploux, L., A. Ponche, and K. Anselme. Bacteria/Material Interfaces: Role of the Material and Cell Wall Properties. *J. Adhes. Sci. Technol.* 24:2165–2201, 2010.
81. Popat, K. C., M. Eltgroth, T. J. Latempa, C. A. Grimes, and T. A. Desai. Decreased Staphylococcus epidermis adhesion and increased osteoblast functionality on antibiotic-loaded titania nanotubes. *Biomaterials* 28:4880–4888, 2007.
82. Puckett, S. D., E. Taylor, T. Raimondo, and T. J. Webster. The relationship between the nanostructure of titanium surfaces and bacterial attachment. *Biomaterials* 31:706–713, 2010.
83. Raad, I., R. Darouiche, R. Hachem, M. Sacilowski, and G. P. Bodey. Antibiotics and prevention of microbial colonization of catheters. *Antimicrob. Agents Chemother.* 39:2397–2400, 1995.
84. Raad, I., J. A. Mohamed, R. A. Reitzel, Y. Jiang, S. Raad, M. A. Shuaibi, A.-M. Chaftari, and R. Y. Hachem. Improved Antibiotic-Impregnated Catheters with Extended-Spectrum Activity against Resistant Bacteria and Fungi. *Antimicrob. Agents Chemother.* 56:935–941, 2012.
85. Ramritu, P., K. Halton, P. Collignon, D. Cook, D. Fraenkel, D. Battistutta, M. Whitby, and N. Graves. A systematic review comparing the relative effectiveness of antimicrobial-coated catheters in intensive care units. *Am. J. Infect. Control* 36:104–117, 2008.
86. von Recum, A. F. Applications and failure modes of percutaneous devices: a review. *J. Biomed. Mater. Res.* 18:323–36, 1984.
87. Rodriguez, B. J., S. V. Kalinin, J. Shin, S. Jesse, V. Grichko, T. Thundat, A. P. Baddorf, and A. Gruverman. Electromechanical imaging of biomaterials by scanning probe microscopy. *J. Struct. Biol.* 153:151–159, 2006.
88. Safdar, N., D. M. Kluger, and D. G. Maki. A review of risk factors for catheter-related bloodstream infection caused by percutaneously inserted, noncuffed central venous catheters: implications for preventive strategies. *Medicine (Baltimore)* 81:466–479, 2002.
89. Seal, B. L., T. C. Otero, and A. Panitch. Polymeric biomaterials for tissue and organ regeneration. *Mater. Sci. Eng. R Rep.* 34:147–230, 2001.
90. Shah, H., W. Bosch, K. M. Thompson, and W. C. Hellinger. Intravascular Catheter-Related Bloodstream Infection. *The Neurohospitalist* 3:144–151, 2013.
91. Shen, M., L. Martinson, M. S. Wagner, D. G. Castner, B. D. Ratner, and T. A. Horbett. PEO-like plasma polymerized tetraglyme surface interactions with leukocytes and proteins: in vitro and in vivo studies. *J. Biomater. Sci. Polym. Ed.* 13:367–390, 2002.
92. Sohail, M. R., A. H. Khan, D. R. Holmes, W. R. Wilson, J. M. Steckelberg, and L. M. Baddour. Infectious Complications of Percutaneous Vascular Closure Devices. *Mayo Clin. Proc.* 80:1011–1015, 2005.
93. Tang, L., and J. W. Eaton. Inflammatory responses to biomaterials. *Am. J. Clin. Pathol.* 103:466–471, 1995.
94. Tebbs, S. E., and T. S. J. Elliott. Modification of central venous catheter polymers to prevent in vitro microbial colonisation. *Eur. J. Clin. Microbiol. Infect. Dis.* 13:111–117.
95. Underwood, R. A., M. L. Usui, G. Zhao, K. D. Hauch, M. M. Takeno, B. D. Ratner, A. J. Marshall, X. Shi, J. E. Olerud, and P. Fleckman. Quantifying the effect of pore size and surface treatment on epidermal incorporation into percutaneously implanted sphere-templated porous biomaterials in mice. *J. Biomed. Mater. Res. A* 98A:499–508, 2011.
96. Utomo, L., G. J. V. M. van Osch, Y. Bayon, J. a. N. Verhaar, and Y. M. Bastiaansen-Jenniskens. Guiding synovial inflammation by macrophage phenotype modulation: an in vitro study towards a therapy for osteoarthritis. *Osteoarthr. Cartil. OARS Osteoarthr. Res. Soc.* , 2016.doi:10.1016/j.joca.2016.04.013
97. Vaterrodt, A., B. Thallinger, K. Daumann, D. Koch, G. M. Guebitz, and M. Ulbricht. Antifouling and Antibacterial Multifunctional Polyzwitterion/Enzyme Coating on Silicone Catheter Material Prepared by Electrostatic Layer-by-Layer Assembly. *Langmuir ACS J. Surf. Colloids* 32:1347–1359, 2016.
98. Vishwakarma, A., N. S. Bhise, M. B. Evangelista, J. Rouwkema, M. R. Dokmeci, A. M. Ghaemmaghami, N. E. Vrana, and A. Khademhosseini. Engineering Immunomodulatory Biomaterials To Tune the Inflammatory Response. *Trends Biotechnol.* 34:470–482, 2016.
99. Walboomers, X. F., and J. A. Jansen. Cell and tissue behavior on micro-grooved surfaces. *Odontology* 89:0002–0011.

100. Wang, J. H.-C., F. Jia, T. W. Gilbert, and S. L.-Y. Woo. Cell orientation determines the alignment of cell-produced collagenous matrix. *J. Biomech.* 36:97–102, 2003.
101. Wang, R., K. G. Neoh, E.-T. Kang, P. A. Tambyah, and E. Chiong. Antifouling coating with controllable and sustained silver release for long-term inhibition of infection and encrustation in urinary catheters. *J. Biomed. Mater. Res. B Appl. Biomater.* 103:519–528, 2015.
102. Zhang, L., Z. Cao, T. Bai, L. Carr, J.-R. Ella-Menye, C. Irvin, B. D. Ratner, and S. Jiang. Zwitterionic hydrogels implanted in mice resist the foreign-body reaction. *Nat. Biotechnol.* 31:553–556, 2013.
103. Zhu, C., S. R. Kustra, and C. J. Bettinger. Photocrosslinkable biodegradable elastomers based on cinnamate-functionalized polyesters. *Acta Biomater.* 9:7362–70, 2013.
104. Global Markets for Catheters. BCC Research, 2014.
105. Vascular Access Overview: Overview, Indications, Types of Catheters. , 2015.at <http://emedicine.medscape.com/article/1018395-overview>
106. Peripheral arterial line : MedlinePlus Medical Encyclopedia Imageat <http://www.nlm.nih.gov/medlineplus/ency/imagepages/19871.htm>
107. Healionics - We help. You heal. - We provide biomaterial solutions to research institutions and medical device manufacturersat <http://www.healionics.com/index.html>

CHAPTER 2 METHODS

The content in this chapter in whole or in part has been previously published in *Biomaterials* and *ACS Biomaterials Science & Engineering*. [Pholpabu, P., S. Kustra, H. Wu, A. Balasubramanian, and C. J. Bettinger. Lithography-free fabrication of reconfigurable substrate topography for contact guidance. *Biomaterials* 39:164–172, 2015.][25]; [Pholpabu, P., S. S. Yerneni, C. Zhu, P. G. Campbell, and C. J. Bettinger. Controlled Release of Small Molecules from Elastomers for Reducing Epidermal Downgrowth in Percutaneous Devices. *ACS Biomater. Sci. Eng.*, 2016.][26]

2.1 Methods for Studying Cell-Topography Interactions

One of the biological cues that can determine cell and tissue behaviors, e.g. migration, adhesion, proliferation, and migration, is environmental topography.[9,11,17,28,29] Studying in cell-topography interactions reveal how in-depth topography influences those processes. Static surfaces can in vitro extract many complex mechanisms that underpin cell-materials interactions such as contact guidance. However, static topography has limitation in investigating dynamic biological processes such as during wound healing, tissue development, and disease. Substrates that present topography with spatiotemporal control are advantageous in simulating and studying cell-materials interactions, including contact guidance, in dynamic milieu.[16,18] In addition, the dynamic topography can be used to match in vivo experiments where topography is dynamically changed upon an insertion of topographic implants. In this study, we generated dynamic surface topography that can decouple contact guidance responses from other

confounding processes such as cell attachment and spreading.[25] The following delineates how we modified PDMS surface with a simple tool to obtain switchable topography.

2.1.a Fabrication and Characterization of Programmable Dynamic Topography

Microfabrication has become a crucial technique in the field of biology, medicine, and biomedical engineering for various applications over the past two decades.[15,21] For studying cell-topography interaction, the most common technique to fabricate surface topography on polydimethylsiloxane (PDMS) substrates, using photolithography that can generate ordered structures, such as grooves, pillars, pits, and wells.[5,20,23,27] However, photolithography requires expensive and precise instrumentation, and an extremely clean room.[12] Here, we designed an easy strain device (Figure 2.1) to use with a thermal evaporator, one of the simplest of the physical vapor deposition techniques, or a UV ozone cleaner to generate buckling surface from the modulus mismatch between PDMS substrate and SiO_x thin film. The strain device can be easily replicated with proper metal cutting and drilling tools. It is also easy to operate, suitable for adjusting strain back and forth during the study.

Briefly, the device can be manually manipulated as following. Firstly, remove mounting plates and screws to place a PDMS substrate to the loading stand. The width of the substrate should be cut to fit in between two mounting screws. After neatly placing the substrate on the loading stands, put the two loading plates and screws back in place. Adjust and measure the initial length of the substrate. Apply desired pre-strain before coating the substrate with SiO_x thin film. The length after applying the pre-strain

can be referred as ε=0. The pre-strain and SiO_x film thickness will dictate buckling patterns, as shown in Eqn. 3.2. The method used to generate and switch microgrooves in this particular study is further detailed as the following.

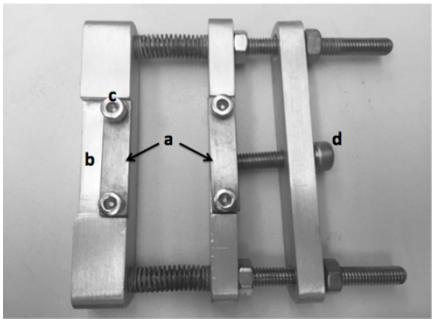

Figure 2.1 Strain device. The strain device is used to adjust strain applied to PDMS substrate. The main parts of the device include a) mounting plates, b) loading stand, c) mounting screw, and d) adjusting knob.

Elastomeric substrates were prepared using polydimethylsiloxane (PDMS, Sylgard 184, Dow Corning, Midland, MI USA) cured in a 10:1 ratio at 75 °C. Rectangular PDMS coupons (W x L x H = 1.5 cm x 3.5 cm x 600 μm) were mounted in a custom fixation device and strained to the desired amount. Pre-strained substrates were coated with 100 nm of silicon oxide (SiO_x) deposited by thermal evaporation. Briefly, silicon monoxide (SiO) was thermally deposited at a rate of 1 Å/sec at 10^{-6} Torr (NexDep, Angstrom Engineering, Kitchener, ON Canada). All substrates were processed in an identical manner with the exception that the thickness of the bi-layer membrane was set at either 10 or 100 nm. Dynamic topography sequences were switched between states in less than 3 sec. Microstructures of bilayer membranes were characterized using optical microscopy (Olympus BH2 microscope, Olympus America Inc., Center Valley, PA USA) and atomic force microscopy (AFM, Dimension 3100 SPM,

Veeco, Plainville, NY USA). Fourier transforms of optical micrographs were prepared using ImageJ (National Institute of Health, USA, available at http://rsb.info.nih.gov/ij).

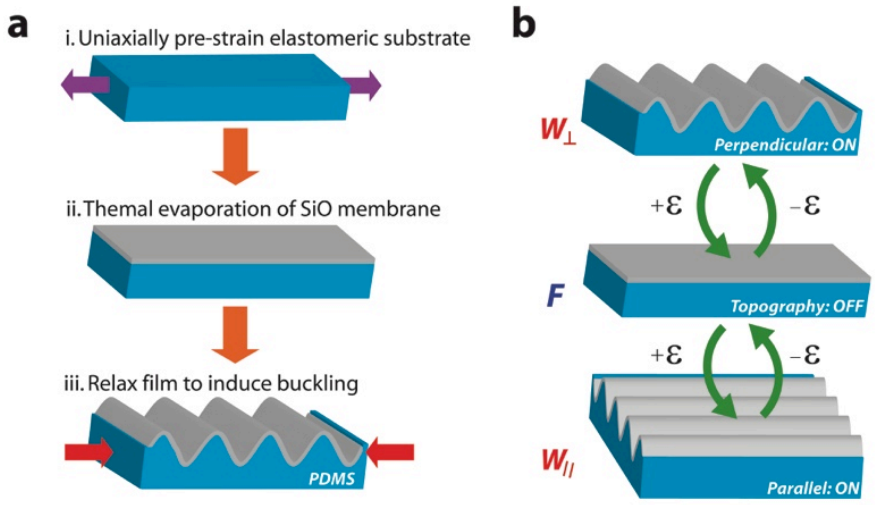

Figure 2.2 Fabrication scheme and actuation of reconfigurable dynamic topography. a) The fabrication flow is shown: (i) PDMS substrates are strained to a prescribed amount and (ii) SiO_2 membranes are deposited on the surface using thermal evaporation. (iii) The pre-strain is released to create wavy grating arrays via spontaneous buckling. b) Programmable topography consists of three discrete strain-dependent states that depend on the difference between the pre-strain and applied strain $\Delta\varepsilon$: $\Delta\varepsilon$ < 0% produces perpendicular wavy gratings $(W_\perp)$; $\Delta\varepsilon$ = 0% produces flat substrates (F); $\Delta\varepsilon$ > 0% produces parallel wavy gratings $(W_\parallel)$. These states are shown sequentially from top to bottom as the value of $\Delta\varepsilon$ becomes more positive.

In our study, the substrate with switchable microgrooves was used to investigate cell morphodynamics of fibroblasts in vitro. The method of cell culture and measurement of cell morphology components are described below.

2.1.b Fibroblast Culture and Imaging

All cell culture supplies were purchased from Invitrogen (Carlsbad, CA USA) unless otherwise stated. Bi-layer membranes were sterilized in ethanol (70% v/v) and irradiated with UV for 30 min. Bi-layer membranes were incubated with RGD solution (50 μg/cm^2) for 40 min and rinsed with 3x PBS. NIH 3T3 fibroblasts (ATCC, Monassas, VA USA) were seeded at densities of 25,000 cells/cm^2 and incubated in DMEM medium supplemented with 10% fetal bovine serum (FBS) and 1% penicillin/streptomycin (P/S) at 37 °C. Live cell images were performed by culturing cells for 24 h prior to dynamic topography sequences. Cells were cultured in en environmentally controlled chamber set at 37 °C with >90% relative humidity and 5% CO_2 (BioImager, Mississauga, ON Canada). FB were imaged in phase contrast and analyzed using NIH ImageJ to measure morphology and relative orientation. Cell circularity was calculated using the following expression.

$$C_{cell} = \frac{4\pi A_{proj}}{P^2} \qquad \text{Eqn. 2.1}$$

where A_{proj} and P are the projected surface area and perimeter of the cell, respectively. The axial ratio R_{axis} was calculated from the length of the major axis divided by the length of the minor axis (Figure 2.3).[7]

Cells were fixed in 4% formaldehyde for 20 min, stained using 20 μL of Alexa Fluor® 488 Phalloidin (200 U/mL), and counterstained with SlowFade® Gold Antifade Reagent with DAPI. Phase contrast and fluorescent images were recorded using an EvosFL microscope (Advanced Microscopy Group, Bothell, WA USA). FB on a static substrate were also imaged using confocal fluorescence microscopy (LSM 510 META DuoScan, Carl Zeiss, Heidelberg Germany) and scanning electron microscopy (SEM)

(PhilipsXL-30 FEG, FEI, Hillsboro, OR, USA). Cells dedicated for SEM imaging were fixed in 4% formaldehyde for 20 min, washed with distilled water for 3 times, and dehydrated in a series of mixtures containing ethanol and hexamethyldisilazane (HDMS), as previously described.[30] Dehydrated samples were coated with 4 nm of platinum prior to imaging (Emtech K575X, Quorum Technologies, Guelph, ON, Canada).

2.1.c Measurement of Cell Components on a Substrate with Gratings

Since most of fibroblast cells are in an irregular shape, it is necessary to define morphology using shape components. Here, we measured cell perimeter (P), projected area (A_{proj}), length of major and minor axes, and alignment angle (θ_{align}), as shown in Figure 2.3. We also calculated cell shape factors, dimensionless shape quantities, including circularity (C_{cell}) using Eqn. 2.1, and axial ratio (R_{axis}) from the length of the major axis divided by the length of the minor axis. The value of C_{cell} is equal to one for circular cells, and is less than 1 or approaches to zero for elongated cells. R_{axis} is equal to 1 for circular cells, and is larger for more elongated cells. These quantifications were used to determine fibroblast morphology on static and dynamic topographic substrates at designated times up to 6 h in order to obtain fibroblast morphodynamics. The results are described in Chapter 3.

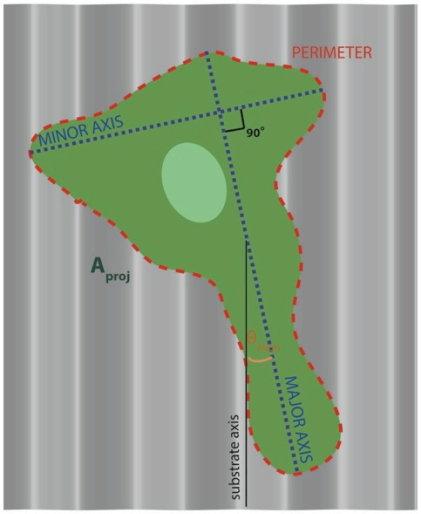

Figure 2.3 Measurement of cell components on a substrate with gratings.[25] The cell components include cell perimeter (P), projected area (A_{proj}), length of major and minor axes, and alignment angle (θ_{align}). P and A_{proj} are indicated in red dotted line and green area, respectively. Major axis is the longest straight line located within a cell. Minor axis is the longest straight line that is perpendicular with the major axis. θ_{align} is an angle between substrate and major axes.

In addition to generating switchable substrates for in vitro studies, PDMS substrates were surface-modified using the strain device to serve as a replica mold for fabricating elastomeric rods from PGS-CinA elastomers (described in 2.2) for in vivo studies. Instead of treating PDMS substrates with thermal evaporation of SiO, SiO_x thin film on PDMS substrates were generated using UV-ozone treatment for 30 min and 30% applied pre-strain. Larger pre-strain, compared to the above-mentioned method, is required to generate stable buckling pattern when using UV-ozone treatment. The different alignments of microgrooves were generated using two different rolling directions as shown in Figure 2.4.

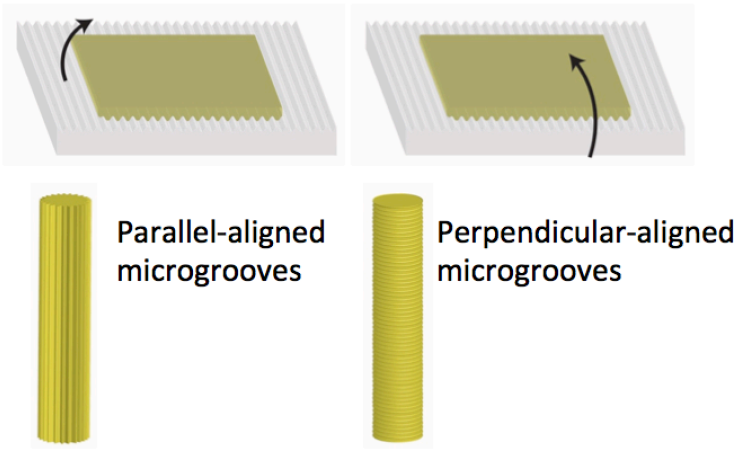

Figure 2.4 Fabrication of polymeric cylinders with microgrooves. Pre-polymers were spread on topographic PDMS mold. After polymerization, microgroove alignment can be determined by the rolling direction.

The cylinders were used for in vivo experiments as described below.

2.1.d In Vivo Implantation and Skin Bridge Measurement

All surgical procedures described in this chapter were performed in accordance with the National Institute of Health standards and approved by the Carnegie Mellon Institutional Animal Care and Use Committee (IACUC) and the National Institute of Health Guide for the Care and Use of Laboratory Animals (NIH Publication #85-23 Rev.1985). PGS-CinA cylinders with and without microgrooves were sterilized in 70% ethanol for 2 hr. Percutaneous devices were implanted percutaneously in anesthetized male mice (C57BL/6; 20-25 weeks; Harlan Laboratories, Indianapolis, IN) transversely through dorsal skin flaps as previously described.[10] Briefly, the mouse dorsal skin was shaved and clipped to have two small exit sites ~0.5 cm apart midline. PGS-CinA implants were inserted through the exit sites and fixed in place with 3M Vetbond™.

Each mouse was implanted with two percutaneous implants and housed separately. The skin bridge length was measured immediately after surgery and at 1 and 2 weeks. Observations were conducted over 4 mice per each treatment each time point. Implanted mice were taken care in separate cages to avoid sample lost from eating and fighting.

2.1.e Statistical Methods

Cell morphodynamic measurements were based on at least 100 cells per each data point and all experiments were repeated in triplicate. All data is shown as mean ± s. e. m. unless otherwise stated. A student's t-test with p-value of 0.05 was performed to consider significant difference of two groups with statistical significance set at p-values of < 0.05. One-way ANOVA with Tukey post-hoc criterion was used to assess the significance across more than 2 groups. The results and discussion are included in Chapter 3.

Preparation and characterization of the elastomer used in this study are described below.

2.2 Synthesis and Characterization of PGS-CinA

2.2.a Synthesis of PGS-CinA Pre-Polymer

A preparation of PGS-CinA pre-polymers and films was adopted from a previously reported method.[35] PGS-CinA precursors were synthesized from PGS

precursors to achieve 26% degree of substitution (DS) of cinnamate groups. 5 g of PGS pre-polymer, received from and described by Zhu *et al.*[35], was dehydrated in a three-neck round bottom flask at 100 °C under vacuum for 2 h. The dried PGS was then dissolved in 30 ml anhydrous chloroform and stirred under nitrogen for 3 h. 20 mg of 4-dimethylaminopyridine and triethylamine (50% mol/mol of pendant hydroxyl groups) were added to serve as a catalyst and a pH neutralizer, respectively. The reaction mixture was cooled in an ice bucket and gradually charged with cinnamoyl chloride (50% mol/mol of pendant hydroxyl groups). After 24 h of the reaction, the mixture was filtrated and put in a rotary evaporator to remove chloroform. 30 ml ethyl acetate was added to precipitate salts. The salt and ethyl acetate were removed by filtration and rotary evaporation, respectively. The product was dissolved in chloroform and repeated with the substitution reaction for two more rounds by using less amount of triethylamine and cinnamoyl chloride (30% mol/mol of pendant hydroxyl groups) to yield DS26%.

2.2.b Preparation of PGS-CinA in Cylindrical Shape

In order to prepare PGS-CinA in cylindrical shape, we have conducted two-step polymerization: photo- and thermal- polymerizations. The two-step polymerization provides more polymeric homogeneity because it avoids distance limitation of UV penetration. Briefly, PGS-CinA films were prepared from PGS-CinA precursors with a degree of a substitution (DS) of 26% using photopolymerization with UV light (λ_{max} = 315 nm; Intensity = 115 mW/cm^2; polymerization time = 3 hr). Solid PGS-CinA cylinders were fabricated by creating “jelly rolls” from coupons (*W x L x t* = 1.5 cm *x* 1.5 cm *x* 100 μm) followed by additional curing at 120 °C for 12 hr in vacuum (<2 Torr). A schematic

of the fabrication of a cylindrical tube is shown in Figure 2.5. PGS-CinA films dedicated for a study of tissue-topography interactions were photopolymerized on the above-mentioned topographic PDMS substrates to obtain buckling patterns. The alignment of microwavy pattern depends on a rolling direction.

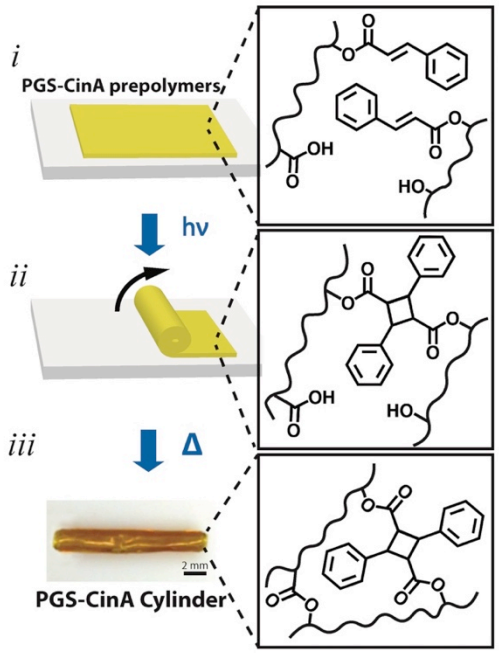

Figure 2.5 Fabrication scheme of a PGS-CinA cylinder. (*i*) PGS-CinA pre-polymers are spread on a quartz slide. (*ii*) The pre-polymers are first partially crosslinked by photodimerization and then rolled into cylindrical form feature. (*iii*) The cylinder is thermally cured and fixed into the final shape by polycondensation reactions.

In this study, PGS-CinA cylinders were also used as matrices for a release of small molecules, so we characterize PGS-CinA mechanical and physical properties that might dictate both release kinetics and tissue-material interactions, as the following.

2.2.c Measurements of Mechanical and Swelling Properties of PGS-CinA

Matrices dedicated for mechanical measurements were delaminated from quartz slides in 70 °C water and sectioned into rectangular coupons (*W x L x t* = 5 mm *x* 10 mm *x* 100 μm). Uniaxial tensile tests (n=3) were conducted using a 10 N load cell at strain rates of 1 mm/min (Instron 5943 equipped with Bluehill 3 software, Norwood, MA). For calculation of volume swelling ratio, PGS-CinA films were replica-molded on PDMS with 5 *x* 5 *x* 0.1 mm^3 square depressions. Patterned films were dehydrated at 60 °C, <2 Torr for 24 hr prior to measuring the dry length L_d. Films were incubated in DI water for 24 hr to measure the swollen length L_s. The dimensional swelling ratio was determined by $Q_{dim} = \left({L_s}/{L_d}\right)^3$ (n=4). The gravitational swelling ratio was determined by weighing PGS-CinA cylinders before and after incubation in DI water at 60 °C for 24 hr, and calculating $Q_{grav} = {M_s}/{M_d}$. The mass density (ρ) was measured using a 25 ml pycnometer.

2.2.d Estimation of PGS-CinA Crosslink Density

The following is a method we used to estimate crosslink density of Photo+Thermal PGS-CinA ($n_{PGS\text{-}CinA\text{-}DS26\%,Photo+Thermal}$ = 7.31 ± 0.8 mol/m^3) reported in Chapter 4. The PGS-CinA crosslink density was estimated based on the linear relationship of Young's modulus and crosslink density that was previously reported for both PGS and PGS-CinA networks.[6,19,35] Zhu *et al.* also reported elastic modulus of photocrosslink PGS-CinA films as a function of the degree of substitution and crosslinking process.[35] PGS-CinA films, in this study, were prepared from PGS-CinA precursors with a degree of substitution (DS) of DS = 26%, using Photo+Thermal

polymerization. The modulus of PGS-CinA films prepared by successive photocrosslinking and thermal curing steps is $E_{PGS\text{-}CinA\text{-}DS26\%,Photo+Thermal}$ = 54.33 ± 0.96 kPa (Photo+Thermal). The elastic modulus and crosslink density of DS26% photocrosslinked PGS-CinA (Photo) was previously reported to be $E_{PGS\text{-}CinA\text{-}DS26\%,Photo}$ = 50.48 ± 3.7 kPa.[35] So, most of the crosslinking networks (92.91 ± 7.0 %) were attributed to the photopolymerization. The results suggest that almost all crosslinkable units were consumed by the first polymerization step. In this study, the thermal polymerization mostly played a role in just assisting a PGS-CinA film fixed into a cylinder. Since the relationship between the elastic modulus E and crosslink density n is linear, the crosslink density of Photo+Thermal PGS-CinA can be estimated from previously reported $n_{PGS\text{-}CinA\text{-}DS26\%,Photo}$ = 6.79 ± 0.5 mol/m^3 to $n_{PGS\text{-}CinA\text{-}DS26\%,Photo+Thermal}$ = 7.31 ± 0.8 mol/m^3.[35]

2.2.e Swelling Ratios for Calculation of Diffusion Coefficient

Swollen hydrogels classically have one swelling ratio Q that is a function of the chemistry and topology of the polymer network along with the solvent, which in this case is water. The swelling is manifested by both an increase in the physical size of the polymer network (since water and polymer are both incompressible) and the mass of network, both of which are attributed to the infiltration of the network with an additional solvent. Since the mass density of the polymer and solvent (water) are known, the calculated value of Q can be measured either geometrically or gravimetrically. Both measurement techniques are widely used to characterize polymers for use as matrices in controlled release systems.[32,34] However, in this work, PGS-CinA belongs to a class

of biodegradable elastomeric networks that is both less hygroscopic and more microporous than a traditional hydrogel precursor (e.g. polyethyleneglycol). Therefore, the infiltration of the micropores of PGS-CinA networks with water might increase the apparent swelling ratio measured by gravimetry, but not necessarily increase the swelling ratio that is measured geometrically. A model of PGS-CinA networks, as shown in Figure 2.3, illustrate PGS-CinA dense and loose network sections that govern measurement of swelling ratio and drug release. Therefore, these two parameters, i.e. gravimetric swelling ratio (Q_{grav}) and volumetric swelling ratio (Q_{dim}), must be measured independently to account for these separate contributions. In this study, PGS-CinA gravimetric swelling ratio was measured by a conventional method, while the volumetric swelling ratio was measured from the dimensions of PGS-CinA microstructures in dried and wet states (Figure 4.2). Both values were used in the calculation of diffusion coefficient of CLA from PGS-CinA matrices, described in Chapter 3.

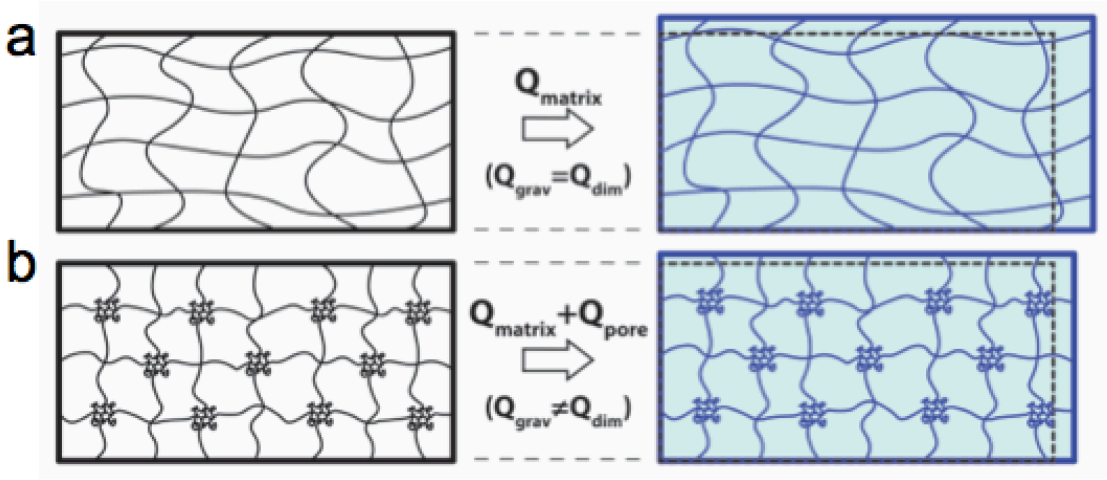

Figure 2.6 Model of typical hydrogel (a) and PGS-CinA (b) networks in dry and swelling states. PGS-CinA networks are not homogenous, containing both dense and loose

network sections. Different swelling behaviors in dense and loose sections cause the difference between volumetric (Q_{dim}) and gravimetric (Q_{grav}) swelling ratios. Consequently, both swelling ratios should be independently measured.

2.3 Macrophages Modulation for Reduction of Dermal Downgrowth

In this study, we used PGS-CinA networks as matrices for a release of small molecules to modulate macrophage phenotypes. The following includes methods we conducted to select anti-inflammatory small molecules and quantified skin downgrowth as a host response to implanted matrices.

2.3.a In vitro Assessment of Anti-Inflammatory Response of Small Molecules

In this study, small molecules for modulating macrophages were selected based on in vitro anti-inflammatory activity. We compared LA and CLA that was previously reported to alter inflammatory response of macrophages in vitro and in vivo by oral administration. RAW-Blue™ cells (InvivoGen, San Diego, CA) were cultured in DMEM (Invitrogen, Carlsbad, CA) supplemented with 10% fetal bovine serum (FBS), 1% penicillin/streptomycin (P/S), 100 μg/ml Normocin™, and 100 μg/ml Zeocin™ at 37 °C. Cells were collected and resuspended in DMEM supplemented with 10% heat-inactivated FBS and 100 μg/ml Normocin™. Cells (1.0×10^5 total) were seeded to 96-well plates and incubated with stimulating agents at the following concentrations: 0.1 μg/ml lipopolysaccharide (LPS); 0.1 μg/ml interleukin-10 (IL-10); 30 μg/ml LA; 30 μg/ml CLA (Nu-Chek-Prep, Inc., Elysian, MN); 0.1 μg/ml LPS with LA or CLA at

concentrations ranging from 0.003 to 30 μg/ml. After incubation at 37 °C for 24 hr, 50 μl of the supernatant (n=3 per each well) was collected into a 96-well plate, quantified using QUANTI-Blue™ using UV-vis (λ_{abs} = 620 nm) detection medium. All stimulating agents were purchased from Sigma-Aldrich (St. Louis, MO) unless otherwise stated. The results are shown in Figure 4.3.

The following explains quantification of dermal downgrowth that was induced by an insertion of PGS-CinA matrices with or without drug loading. The detail of in vivo experiments is described in Chapter 4.

2.3.b Characterization of Drug-Eluting Matrices

PGS-CinA cylinders (*D x L* = 1.5 mm *x* 15 mm) dedicated to measure release kinetics were incubated in 70% ethanol for 2 hr to remove sol and loaded with LPS (lipopolysaccharide), CLA, or LPS+CLA solutions in methanol overnight at the following concentrations: [LPS] = 0.5 mg/ml, [CLA] = 1-100 mg/ml. PGS-CinA matrices incubated with CLA were briefly rinsed in sterile water for 10 min prior to in vitro and in vivo controlled release studies. LPS-loaded matrices were briefly washed for 2 sec to remove excess LPS on the surface while minimizing premature release of LPS from the matrix. Release assays were performed in 2 ml of 0.5% tween in PBS at 37 °C. Eluted LPS was quantified using EndoZyme® recombinant Factor C Assay (Endotoxin Testing Solutions LLC, Athens, GA). The concentration of CLA released was measured using UV-vis (λ_{abs} = 260 nm).

2.3.c In Vivo Implantation and Gross Anatomical Assessment

PGS-CinA cylinders were sterilized in 70% ethanol for 2 hr and loaded with 0.5 mg/ml LPS, 100 mg/ml CLA, or both. PGS-CinA devices were dried in ambient conditions for 18 hr to ensure complete evaporation of methanol solvent. Percutaneous devices were implanted percutaneously in anesthetized male mice (C57BL/6; 20-25 weeks; Harlan Laboratories, Indianapolis, IN) transversely through dorsal skin flaps as previously described.[10] Briefly, the mouse dorsal skin was shaved and clipped to have two small exit sites ~0.5 cm apart midline. PGS-CinA implants were inserted through the exit sites and fixed in place with 3M Vetbond™. Each mouse was implanted with two percutaneous implants and housed separately. The skin bridge length was measured immediately after surgery and at prescribed times as previously reported by Fleckman et al.[10] Observations were conducted over 4 mice per each treatment each time point. Implanted mice were taken care in separate cages to avoid sample lost from eating and fighting. Two rods of the PGS-CinA matrices were well fit on the mouse back as shown in 3.11. The glue dried out within 1-2 days and detached from the skin, while all rods stayed in place. There was no sign of irritation or infection over the experimental period.

2.3.d Histological Assessment

Dermal explants were fixed in 10% formalin, embedded in paraffin, sectioned, and stained with hematoxylin and eosin (H&E). Immunohistochemistry was also performed using CD163 antibodies (Biorbyt, San Francisco, CA). CD163 was used as marker for M2 macrophages.[1] Micrographs were recorded using a Leica DM IL LED microscope (Buffalo Grove, IL) and analyzed using NIH ImageJ (National Institute of Health, USA, available at http://rsb.info.nih.gov/ij). The density of M2 macrophages was

measured by counting the number of CD163+ cells in four randomly selected areas along the tissue-device interface (a user defined area of *L x W* = 192 μm *x* 40 μm) in each skin sample. The characteristic distance from the implant was chosen based on previous studies.[4,31,33] The downgrowth measurements are described as followed.

2.3.e Quantification of Dermal Downgrowth

In a study of percutaneous devices, dermal downgrowth is one of the most important factors that indicate biomaterial biocompatibility and skin-device interactions. Even though several researches have reported the reduction of dermal downgrowth using different types of materials, there is still no exact universal way to measure it. The measurement of dermal downgrowth can be defined in different ways. Pendegrass *et al*. measured dermal downgrowth by the line transection method. They essentially measured the line that is drawn from the highest point of skin-device interface to an intersecting skin line, as shown in Figure 2.4 (Left panel).[24] Mitchell *et al*. instead calculated the dermal downgrowth as a percentage of the exposed coating length to the total fixation length, as shown in Figure 2.4 (Right panel).[22] However, both methods can be used for only when skin integrates to a device so firmly that sample sectioning cannot tear those two apart. Studying percutaneous devices that do not aim to provide complete biointegration might need other methods for the quantification.

In this study, we propose a method for measuring dermal downgrowth, as shown in Figure 2.5. This method can be applied to H&E skin samples that might not come with an implanted material. Briefly, an image of skin sample was processed to eliminate all part of subcutaneous adipose tissue by adjusting picture contrast. The image was

then skeletonized to have a middle line. This line was used to calculate average skin half thickness that was used to normalize the downgrowth because the skin thickness is not equal among samples. The average skin thickness was measured from 8 random positions in each sample. The dermal downgrowth was measured as a distance from the turning line to the end of dermal layer minus the average half thickness.

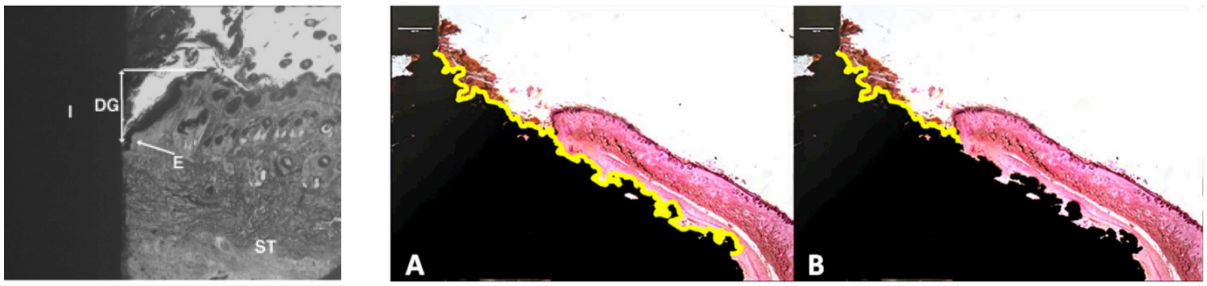

Figure 2.7 Representative micrographs showing methods for quantifying dermal downgrowth in researches from Pendegrass *et al*. and Mitchell *et al*.[22,24]

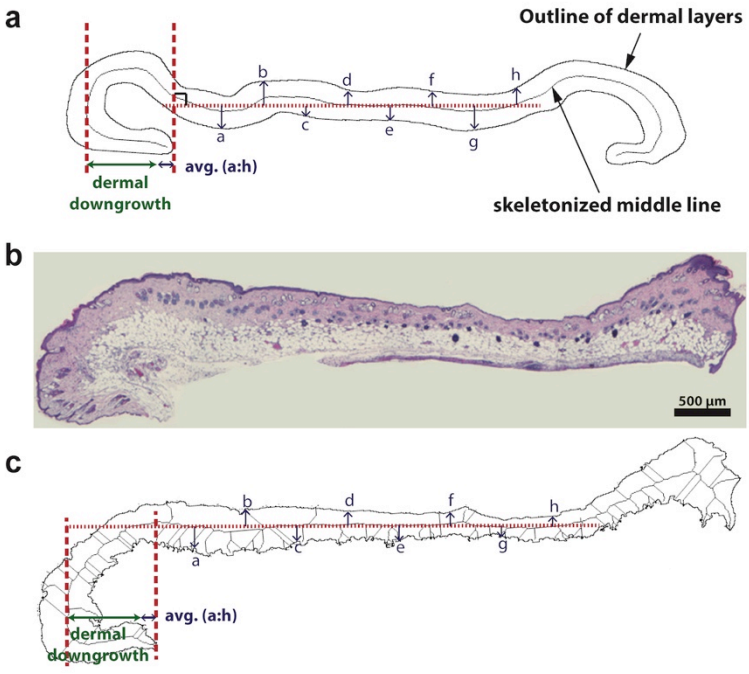

Figure 2.8 Quantifying dermal downgrowth.[26] (a) Schematic of a dermal layer model for quantification. Dermal downgrowth is calculated from the overlapped skeletonized

length at an end subtracted with average half dermal thickness (a to h). The area above the straight horizontal dermal axis to the skeletonized middle line is equal to the area under the dermal axis to the middle line. (b) Representative actual mouse skin sample. (c) Example of a skeletonized image from the actual sample. The dermal downgrowth is calculated as described.

2.3.f Statistical Analysis

Data sets were analyzed using one-way ANOVA followed by Tukey's post hoc test, or two-way ANOVA followed by Bonferroni correction, and/or Kruskal-Wallis test followed by Conover post hoc test. All statistical analysis was performed using Medcalc statistical software. Confidence intervals for diffusion coefficients were determined using the Monte Carlo method.[14] The results and discussion are included in Chapter 4.

Other than the two above-mentioned approaches: topographical cues and macrophage modulation, anti-fouling hydrogels were prepared in a cylindrical shape to investigate tissue responses using the same in vivo mouse model. The preparation and characterization is described down below.

2.4 Preparation and Characterization of Hydrogels

2.4.a Preparation of Hydrogels

PCBMA was prepared from PCBMA monomers and PCBMX crosslinkers as following. Briefly, PCBMA and PCBMAX with varying %mol were well mixed together

(total concentration of 1 M). 10 mmol ammonium persulphate (APS) and 10 mmol tetramethylethylenediamine (TEMED) as an initiator and catalyzer were added right before loading the mixture into a cylindrical silicone mold (*D* x *L* = 3 mm x 30 mm). The gel formation could be seen within about one minute. The reaction was allowed to continue for 2 h at ambient condition. PCBMA hydrogels dedicated for rheological measurements were prepared between two glass slides with 750 μm spacer to get a disc with ~16 mm in diameter. PHEMA hydrogels were prepared from HEMA monomers using 5 %mol ethyleneglycol dimethacrylate (EGDMA), as a crosslinker. The total concentration of monomers and crosslinkers was 3 and 5 M. PHEMA polymerization was done using the same procedure as PCBMA.

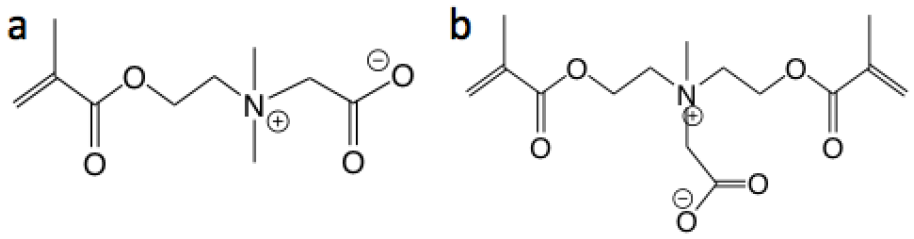

Figure 2.9 Chemical structures of (a) CBMA monomers and (b) CBMAX crosslinkers.

One of the challenges in this study is to prepare hydrogels in cylindrical shape. Since PCBMA and PHEMA are not tough elastomers, they cannot be prepared from a thin film in the similar way we prepared PGS-CinA rods. Also, although photopolymerization would benefit in its non-toxicity since it does not require additional chemicals, it is limited in penetration depth. So, redox polymerization using APS and TEMED was conducted to prepare PCBMA and PHEMA hydrogels. The cytotoxicity of APS and TEMED was reported[8], but rigorous washing (7 days in sterile PBS that was changed at least twice daily) can solve the issue.[3,13] The procedure is also

uncomplicated, and the reaction mixture can easily fit into a cylindrical mold, as shown in Figure 2.10.

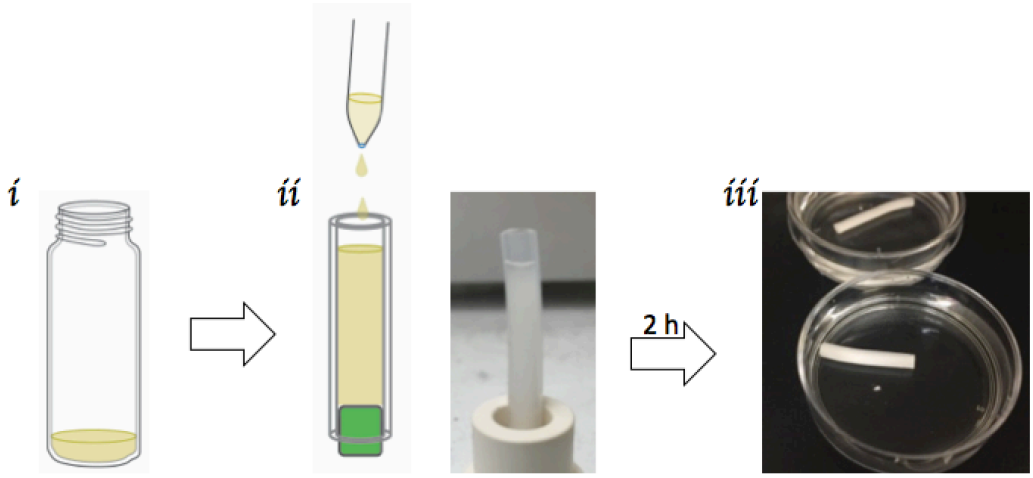

Figure 2.10 A schematic of hydrogel preparation in a cylindrical mold. (i) Reaction mixture, including monomers, crosslinkers, APS, and TEMED, was well mixed before (ii) adding into a cylindrical mold. The mixture was polymerized for 2 h to obtain a cylindrical hydrogel (iii).

2.4.b Measurements of Mechanical Properties and Swelling of Hydrogels

PCBMA and PHEMA hydrogels were washed in DI water and phosphate buffered saline (PBS) for 1 and 7 d, respectively. The washing step was done similarly to the hydrogels dedicated for implantation. The cylindrical gels were cut to ~2.5 mm in thickness. The diameter of each sample was measured using a micrometer. Uniaxial compressive tests (n=8) were conducted using a 10 N load cell at strain rates of 1 mm/min (Instron 5943 equipped with Bluehill 3 software, Norwood, MA). For rheological measurements, the hydrogel discs were washed and swollen in DI water until the water content reached equilibrium. The mechanical properties of hydrogels (n=4) were

measured using a rheometer (HR-2, TA Instruments, New Castle, DE). The viscoelastic region for each hydrogel was determined by a strain sweep experiment at 1 rad s^{-1} frequency and 25 °C. A frequency sweep test was conducted at 0.5% strain and 25 °C. The strain is constant for all hydrogels for use in comparison. The hydrogels used for determining swelling ratio were also washed and swollen in water. The increase in hydrogel weight was monitored until there was no further change in weight. Mass swelling ratio was determined by the following equation.

$$\text{Mass swelling ratio} = (\text{Mass}_{\text{swollen}} - \text{Mass}_{\text{dry}})/\text{Mass}_{\text{dry}}. \qquad \text{Eqn. 2.2}$$

PCBMA and PHEMA hydrogels were also prepared into a disc for rheological measurement that was conducted using a rheometer (HR-2, TA Instruments, New Castle, DE). It is recommended that a hydrogel disc should be at least 800 μm but not more than 1000 μm in thickness, and more than 15 mm in diameter, to obtain consistent and reliable results. We prepared each hydrogel using the total volume of reaction mixture (monomers+crosslinker+APS+TEMED) at 200 μL and pipetted the mixture into space between two glass slides with 750 μm spacers, as shown in Figure 2.11. After swelling in DI water for 3-4 days, the hydrogel became in the recommended size. All hydrogels were measured using a strain sweep test at 1 rad s^{-1} frequency and 25 °C, and a frequency sweep test at 0.5% strain and 25 °C. The results are shown in Chapter 5.

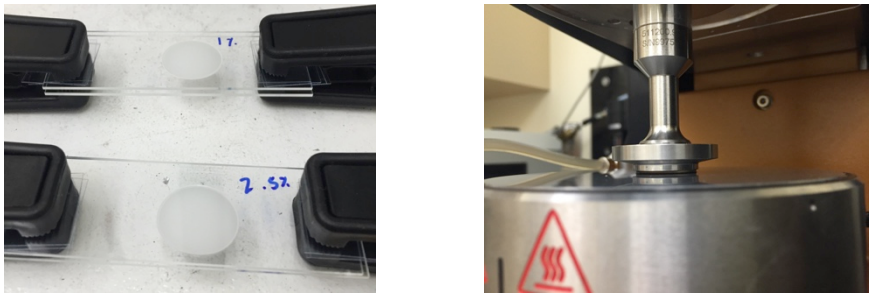

Figure 2.11 Preparation of hydrogel discs and Rheological measurement setup. Left: Hydrogel circular discs were prepared between two glass slides with 750 μm spacers for rheology measurement. Right: A hydrogel disc is placed between two smooth flat plates in a rheometer.

2.4.c In vivo Percutaneous Implantation of Cylindrical Hydrogels

PCBMA and PHEMA hydrogels were transferred from the cylindrical mold to sterile DI water in a biological cabinet to avoid bacterial contamination. The hydrogels were further washed in PBS that was changed twice a day for 7 d. The hydrogels were air-dried in a biological cabinet for 18 h and put in normal saline for one minute right before a surgery. Percutaneous devices were implanted percutaneously in anesthetized male mice (C57BL/6; 7-10 weeks; Harlan Laboratories, Indianapolis, IN) transversely through dorsal skin flaps as previously described.[10,26] Briefly, the mouse dorsal skin was shaved and clipped to have two small exit sites ~0.8 cm apart midline. PCBMA and PHEMA implants were inserted through the exit sites and fixed in place with 3M Vetbond™. Each mouse was implanted with two percutaneous implants and housed separately. The skin bridge length was measured immediately after surgery (0 d) and in a daily manner up to 20 d.

2.4.d Histology and Immunohistochemistry

Implanted mouse skins were collected at designated times: 5, 10, 15, and 20 d (n=4, each treatment each time point). Dermal explants were fixed in 10% formalin, embedded in paraffin, sectioned, and stained with hematoxylin and eosin (H&E) and Masson's trichrome. Immunohistochemistry was also performed using CD68/pStat1 and CD68/CD163 antibodies (Biorbyt, San Francisco, CA) for fluorescent double staining. CD68/pStat1 and CD68/CD163 was used as marker for M1 and M2 macrophages, respectively.[1,2] Analysis of the histological samples will be performed in this near future.

2.4.e Statistical Analysis

Data sets were analyzed using one-way ANOVA followed by Tukey-Kramer post hoc test, or repeated measures ANOVA followed by Bonferroni correction. The tests of within-subjects effects in repeated measures ANOVA were based on sphericity assumed and Huynh-Feldt corrections. Statistical analyses were performed using either SPSS or Medcalc statistical software. The results and discussion are included in Chapter 5.

References:

1. Badylak, S. F., J. E. Valentin, A. K. Ravindra, G. P. McCabe, and A. M. Stewart-Akers. Macrophage phenotype as a determinant of biologic scaffold remodeling. *Tissue Eng. Part A* 14:1835–1842, 2008.
2. Barros, M. H. M., F. Hauck, J. H. Dreyer, B. Kempkes, and G. Niedobitek. Macrophage Polarisation: an Immunohistochemical Approach for Identifying M1 and M2 Macrophages. *PLoS ONE* 8:, 2013.
3. Bencherif, S. A., R. W. Sands, D. Bhatta, P. Arany, C. S. Verbeke, D. A. Edwards, and D. J. Mooney. Injectable preformed scaffolds with shape-memory properties. *Proc. Natl. Acad. Sci.* 109:19590–19595, 2012.

4. Bettinger, C. J., J. P. Bruggeman, J. T. Borenstein, and R. S. Langer. Amino alcohol-based degradable poly(ester amide) elastomers. *Biomaterials* 29:2315–2325, 2008.
5. Cao, Y., J. Chen, M. O. Adeoye, and W. O. Soboyejo. Investigation of the spreading and adhesion of human osteosarcoma cells on smooth and micro-grooved polydimethylsiloxane surfaces. *Mater. Sci. Eng. C* 29:119–125, 2009.
6. Chen, Q., X. Yang, and Y. Li. A comparative study on in vitro enzymatic degradation of poly(glycerol sebacate) and poly(xylitol sebacate). *RSC Adv.* 2:4125, 2012.
7. den Braber, E. T., J. E. de Ruijter, L. A. Ginsel, A. F. von Recum, and J. A. Jansen. Quantitative analysis of fibroblast morphology on microgrooved surfaces with various groove and ridge dimensions. *Biomaterials* 17:2037–2044, 1996.
8. Desai, E. S., M. Y. Tang, A. E. Ross, and R. A. Gemeinhart. Critical factors affecting cell encapsulation in superporous hydrogels. *Biomed. Mater. Bristol Engl.* 7:24108, 2012.
9. Ferrari, A., M. Cecchini, M. Serresi, P. Faraci, D. Pisignano, and F. Beltram. Neuronal polarity selection by topography-induced focal adhesion control. *Biomaterials* 31:4682–94, 2010.
10. Fleckman, P., M. Usui, G. Zhao, R. Underwood, M. Maginness, A. Marshall, C. Glaister, B. Ratner, and J. Olerud. Cutaneous and inflammatory response to long-term percutaneous implants of sphere-templated porous/solid poly(HEMA) and silicone in mice. *J. Biomed. Mater. Res. A* 100A:1256–1268, 2012.
11. Han, L., Z. Mao, J. Wu, Y. Guo, T. Ren, and C. Gao. Unidirectional migration of single smooth muscle cells under the synergetic effects of gradient swelling cue and parallel groove patterns. *Colloids Surf. B Biointerfaces* 111C:1–6, 2013.
12. Han, X., X. Liu, L. Tian, H. Zhang, and Z.-G. Mao. A Non-Photolithography Fabrication for a Microfluidic Chip Based on PMMA Polymer. *Machines* 3:107–122, 2015.
13. Hong, Y., Z. Mao, H. Wang, C. Gao, and J. Shen. Covalently crosslinked chitosan hydrogel formed at neutral pH and body temperature. *J. Biomed. Mater. Res. A* 79A:913–922, 2006.
14. Hu, W., J. Xie, H. W. Chau, and B. C. Si. Evaluation of parameter uncertainties in nonlinear regression using Microsoft Excel Spreadsheet. *Environ. Syst. Res.* 4:1–12, 2015.
15. Khademhosseini, A., R. Langer, J. Borenstein, and J. P. Vacanti. Microscale technologies for tissue engineering and biology. *Proc. Natl. Acad. Sci. U. S. A.* 103:2480–2487, 2006.
16. Kim, J., and R. C. Hayward. Mimicking dynamic in vivo environments with stimuli-responsive materials for cell culture. *Trends Biotechnol.* 30:426–39, 2012.
17. Kolind, K., D. Kraft, T. Bøggild, M. Duch, J. Lovmand, F. S. Pedersen, D. A. Bindslev, C. E. Bünger, M. Foss, and F. Besenbacher. Control of proliferation and osteogenic differentiation of human dental-pulp-derived stem cells by distinct surface structures. *Acta Biomater.* 10:641–50, 2014.
18. Lam, M. T., W. C. Clem, and S. Takayama. Reversible on-demand cell alignment using reconfigurable microtopography. *Biomaterials* 29:1705–12, 2008.
19. Liang, S.-L., X.-Y. Yang, X.-Y. Fang, W. D. Cook, G. A. Thouas, and Q.-Z. Chen. In Vitro enzymatic degradation of poly (glycerol sebacate)-based materials. *Biomaterials* 32:8486–8496, 2011.
20. Mata, A., C. Boehm, A. J. Fleischman, G. Muschler, and S. Roy. Growth of connective tissue progenitor cells on microtextured polydimethylsiloxane surfaces. *J. Biomed. Mater. Res.* 62:499–506, 2002.
21. Mata, A., C. Boehm, A. J. Fleischman, G. Muschler, and S. Roy. Analysis of Connective Tissue Progenitor Cell Behavior on Polydimethylsiloxane Smooth and Channel Micro-Textures. *Biomed. Microdevices* 4:267–275.
22. Mitchell, S. J., S. Jeyapalina, F. R. Nichols, J. Agarwal, and K. N. Bachus. Negative pressure wound therapy limits downgrowth in percutaneous devices: NPWT limits epithelial downgrowth. *Wound Repair Regen.* 24:35–44, 2016.
23. Nikkhah, M., F. Edalat, S. Manoucheri, and A. Khademhosseini. Engineering microscale topographies to control the cell–substrate interface. *Biomaterials* 33:5230–5246, 2012.
24. Pendegrass, C. J., A. E. Goodship, J. S. Price, and G. W. Blunn. Nature's answer to breaching the skin barrier: an innovative development for amputees. *J. Anat.* 209:59–67, 2006.
25. Pholpabu, P., S. Kustra, H. Wu, A. Balasubramanian, and C. J. Bettinger. Lithography-free fabrication of reconfigurable substrate topography for contact guidance. *Biomaterials* 39:164–172, 2015.
26. Pholpabu, P., S. S. Yerneni, C. Zhu, P. G. Campbell, and C. J. Bettinger. Controlled Release of Small Molecules from Elastomers for Reducing Epidermal Downgrowth in Percutaneous Devices. *ACS Biomater. Sci. Eng.* , 2016.doi:10.1021/acsbiomaterials.6b00192

27. Rao, C., T. Prodromakis, L. Kolker, U. A. R. Chaudhry, T. Trantidou, A. Sridhar, C. Weekes, P. Camelliti, S. E. Harding, A. Darzi, M. H. Yacoub, T. Athanasiou, and C. M. Terracciano. The effect of microgrooved culture substrates on calcium cycling of cardiac myocytes derived from human induced pluripotent stem cells. *Biomaterials* 34:2399–2411, 2013.
28. Seo, C. H., H. Jeong, K. S. Furukawa, Y. Suzuki, and T. Ushida. The switching of focal adhesion maturation sites and actin filament activation for MSCs by topography of well-defined micropatterned surfaces. *Biomaterials* 34:1764–71, 2013.
29. Sheets, K., S. Wunsch, C. Ng, and A. S. Nain. Shape-dependent cell migration and focal adhesion organization on suspended and aligned nanofiber scaffolds. *Acta Biomater.* 9:7169–77, 2013.
30. Slízová, D., O. Krs, and B. Pospísilová. Alternative method of rapid drying vascular specimens for scanning electron microscopy. *J. Endovasc. Ther. Off. J. Int. Soc. Endovasc. Spec.* 10:285–7, 2003.
31. Sussman, E. M., M. C. Halpin, J. Muster, R. T. Moon, and B. D. Ratner. Porous Implants Modulate Healing and Induce Shifts in Local Macrophage Polarization in the Foreign Body Reaction. *Ann. Biomed. Eng.* 42:1508–1516, 2013.
32. Tomić, S. L., M. M. Mićić, J. M. Filipović, and E. H. Suljovrujić. Swelling and drug release behavior of poly(2-hydroxyethyl methacrylate/itaconic acid) copolymeric hydrogels obtained by gamma irradiation. *Radiat. Phys. Chem.* 76:801–810, 2007.
33. Zhang, L., Z. Cao, T. Bai, L. Carr, J.-R. Ella-Menye, C. Irvin, B. D. Ratner, and S. Jiang. Zwitterionic hydrogels implanted in mice resist the foreign-body reaction. *Nat. Biotechnol.* 31:553–556, 2013.
34. Zhang, X.-Z., D.-Q. Wu, and C.-C. Chu. Synthesis, characterization and controlled drug release of thermosensitive IPN–PNIPAAm hydrogels. *Biomaterials* 25:3793–3805, 2004.
35. Zhu, C., S. R. Kustra, and C. J. Bettinger. Photocrosslinkable biodegradable elastomers based on cinnamate-functionalized polyesters. *Acta Biomater.* 9:7362–7370, 2013.

CHAPTER 3 LITHOGRAPHY-FREE FABRICATION OF RECONFIGURABLE SUBSTRATE TOPOGRAPHY USING SUB-THRESHOLD STRAIN STIMULI

The content in this chapter in whole or in part has been previously published in *Biomaterials*. [Pholpabu, P., S. Kustra, H. Wu, A. Balasubramanian, and C. J. Bettinger. Lithography-free fabrication of reconfigurable substrate topography for contact guidance. *Biomaterials* 39:164–172, 2015.][45]

3.1 Abstract

Mammalian cells detect and respond to topographical cues presented in natural and synthetic biomaterials both in vivo and in vitro. Micro- and nano-structures influence the adhesion, morphology, proliferation, migration, and differentiation of many phenotypes. Although the mechanisms that underpin cell-topography interactions remain elusive, synthetic substrates with well-defined micro- and nano-structures are important tools to elucidate the origin of these responses. Substrates with reconfigurable topography are desirable because programmable cues can be harmonized with dynamic cellular responses. Here we present a lithography-free fabrication technique that can reversibly present topographical cues using an actuation mechanism that minimizes the confounding effects of applied stimuli. This method utilizes strain-induced buckling instabilities in bi-layer substrate materials with rigid uniform silicon oxide membranes that are thermally deposited on elastomeric substrates. The resulting surfaces are capable of reversible of substrates between

three distinct states: flat substrates (A = 1.53 ± 0.55 nm, Rms = 0.317 ± 0.048 nm); parallel wavy grating arrays ($A_{\parallel}$ = 483.6 ± 7.8 nm and $\lambda_{\parallel}$ = 4.78 ± 0.16 mm); perpendicular wavy grating arrays ($A_{\perp}$ = 429.3 ± 5.8 nm; $\lambda_{\perp}$ = 4.95 ± 0.36 mm). The cytoskeleton dynamics of 3T3 fibroblasts in response to these surfaces was measured using optical microscopy. Fibroblasts cultured on dynamic substrates that are switched from flat to topographic features (FLAT-WAVY) exhibit a robust and rapid change in gross morphology as measured by a reduction in circularity from 0.30 ± 0.13 to 0.15 ± 0.08 after 5 min. Conversely, dynamic substrate sequences of FLAT-WAVY-FLAT do not significantly alter the gross steady-state morphology. Taken together, substrates that present topographic structures reversibly can elucidate dynamic aspects of cell-topography interactions.

3.2 Introduction

Mammalian cells can detect the topography of biomaterials in both natural and synthetic microenvironments.[7,12,15,22,32] Topography plays an important role in determining the collective cell behavior in many complex biological processes in development, wound healing, and tissue regeneration.[7,22,23,32,40,43,53,55] Topographical cues control fundamental cellular functions including adhesion, migration, proliferation, and differentiation.[19,25,35,47,48] Most phenomenological studies that correlate cell function with feature geometry and size employ substrates with static structures.[4,8,14,21,36,41,43,56,57,65] Static surfaces can extract many complex mechanisms that underpin cell-materials interactions such as contact guidance. However, there is a

limit to the insight that can be gained by interrogating dynamic systems with static cues. Substrates that present topography with spatiotemporal control are advantageous in studying cell-materials interactions including contact guidance. They can potentially decouple contact guidance responses from other confounding processes such as cell attachment and spreading.[33,37]

Controlled presentation of topographical cues has improved through recent advances in stimuli-responsive materials[34,62] precise delivery of stimuli such as temperature changes, light, or mechanical strain.[4,7,19,23,34,40,54] This strategy has been used for dynamic microstructure presentation to study cell-materials interactions in numerous contexts.[7,15,28,33] Programmable topography can also be engineered using stimuli-responsive polymers including those that respond to cues such as electric fields, temperature changes, and enzymes.[15,29,33,38,62]

The introduction of external stimuli may affect baseline metabolism, viability, or proliferation of cell populations.[59] For example, changes in temperature, the presence of enzymes, or irradiated light can impact basal cell function.[15,59] Mechanical stimuli via direct application of strain is advantageous for topographic feature formation because it is rapid, robust, and facile.[7,33] Most currently available methods that use strain-induced topography require uniaxial strains of greater than 10%.[7,31,37] Mammalian cells can detect strains of the underlying substrate as small as 3.5% and respond to these stains by altering their morphology.[51,58] Therefore, inducing topographic features using mechanical strains >3.5% may convolve contact guidance with responses to substrate deformation. Strain-induced topography will ideally utilize mechanical stimuli that are below the lower limit of detection for mammalian cells. Furthermore, mechanical stimuli

can be coupled with materials that can reversibly present homogeneous topographical cues in various orientations. Herein we report a lithography-free fabrication technique that is capable of producing strain-induced topography using sub-threshold uniaxial strains. Cytoskeleton morphodynamics in fibroblasts are measured using these model surfaces.

3.3 Materials and Methods

Materials and methods of this chapter are described in Chapter 2.

3.4 Results and discussion

3.4.a Microstructural Characterization of Dynamic Topography

Strain-induced feature formation is a convenient strategy for rapid programmable presentation of topographic cues. Ordered buckling is an energy-relief mechanism that occurs when a thin rigid membrane on an elastomeric substrate is compressed.[5,6] Releasing the pre-strain of bi-layer substrates produces grating arrays composed of ridge-groove features with short-range order (Figure 3.1).[60] This phenomenon has been used as a non-conventional microfabrication technique.[46] Rigid silicon oxide (SiO_2) membranes on polydimethylsiloxane (PDMS) substrates are commonly fabricated by exposing PDMS to O_2 plasma.[2,64] PDMS-SiO_2 bilayers fabricated in this manner typically require large uniaxial strains (ε > 10%) to create grating arrays.[49,64] One possible explanation is that the minimum thickness of SiO_2 membranes processed

using O_2 plasma is large because a significant depth of the PDMS must be converted into SiO_2 before a strain-sensitive percolating network of oxide structures is formed within the substrate. The alternative method described herein uses thermal evaporation of SiO to deposit homogeneous SiO_x (with $1.5 < x < 2$) film apical to PDMS substrates.[1] This approach reduces the effective critical strain required for feature formation via compression. Although the exact composition of SiO_x rigid membranes depends upon the deposition procedure, the composition will hereby be referred to as SiO_2 for simplification.

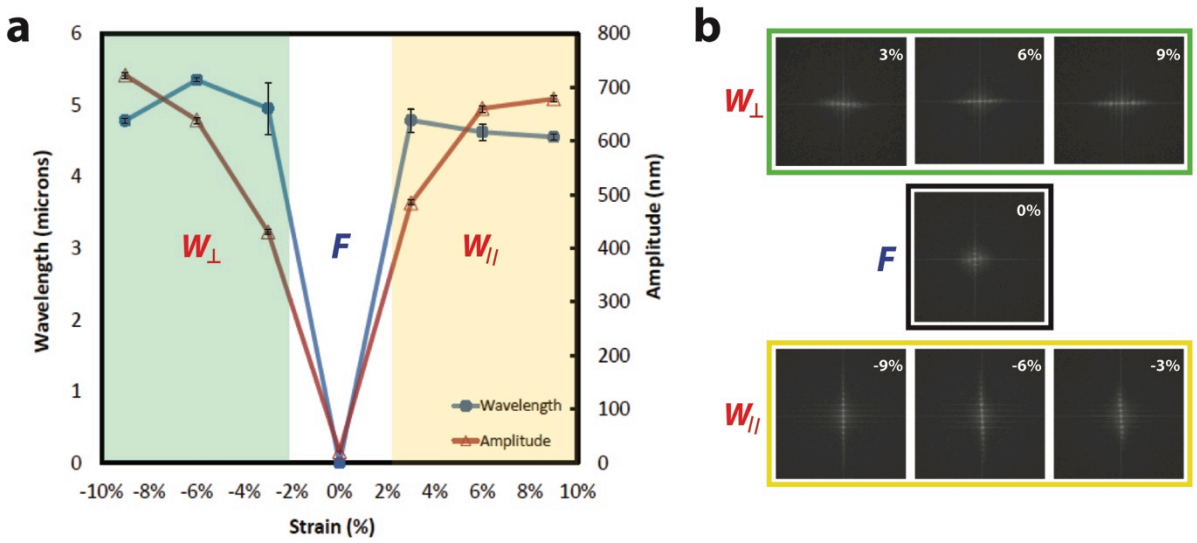

Figure 3.1 PDMS-SiO_2 bilayer substrates produce reconfigurable programmable topography. PDMS-SiO_2 bilayer substrates are pre-strained to ε_{pre} = 9% and coated with SiO_2 layers of h_f = 100 nm. a) Wavelengths and amplitudes of the surface features are measured as a function of $\Delta\varepsilon = \varepsilon_{app} - \varepsilon_{pre}$. Values of $\Delta\varepsilon < 0\%$, $\Delta\varepsilon = 0\%$ and $\Delta\varepsilon > 0\%$ generate perpendicular wavy gratings ($W_\perp$), featureless flat substrates (F), and parallel wavy gratings ($W_\parallel$) features, respectively. b) Fast Fourier Transforms (FFT) of PDMS-SiO_2 bilayer substrates with the for $-9\% < \Delta\varepsilon < +9\%$. The intensity and relative

orientation of FFT signals confirm the presence (absence) of distinguishable features and the orientation of wavy grating arrays in the following discrete states: $W_{\perp}$, F, and $W_{\parallel}$.

The morphologies of PDMS-SiO_2 bilayers in flat (*F*) and wavy ($W_{\perp}$) configurations are shown in Figure 3.2. Cycling the strain forms microstructures reversibly as indicated by optical and scanning probe microscopy. AFM images of bilayers in flat configuration (ε = 0%) contain features with characteristic peak-to-trough amplitudes of approximately 2 nm. This feature height is an order of magnitude smaller than the minimum detection limit for mammalian cells.[4,10] The size of the microstructure of the grating is a strong function of the intensive mechanical properties of the two materials: the thickness of the membrane h_f, and the amount of pre-strain ε_{pre}.[30,44] The anticipated values for average peak-to-through amplitude A_0 and wavelength of the features λ_0 in grating arrays with net compressive strains can be predicted using the following relationships:

$$\lambda_0 = 2\pi h_f \left(\frac{E_f}{3E_s}\right)^{1/3} \qquad \text{Eqn. 3.1}$$

$$A_0 = h_f \sqrt{\frac{\varepsilon_{pre}}{\varepsilon_c} - 1} \qquad \text{Eqn. 3.2}$$

The parameters in each equation are as follows: h_f is the thickness of the rigid membrane; E_f and E_s are Young's moduli of substrate and rigid membrane, respectively; ε_{pre} is amount of uniaxial pre-strain; ε_c is critical buckling strain given by:[30]

$$\varepsilon_c = \frac{1}{4}\left(\frac{3E_s}{E_f}\right)^{2/3} \qquad \text{Eqn. 3.3}$$

A buckling pattern is established only when the applied strain exceeds ε_c. Values for l_0 are predicted to be largely independent of the amount of pre-strain. However, experimentally observed values of λ_0 are reduced for uniaxial strains greater than

10%.[26,30,52] Relationships that describe feature sized formed via spontaneous buckling are valid if certain criteria are satisfied. The intensive properties and extensive geometry of the film must be such that $E_f >> E_f$ and $h_f << t_s$ where t_s is the substrate thickness. The net strain *De* is defined as the difference between the resulting applied strain e_{app} and the pre-strain via $\Delta\varepsilon = \varepsilon_{app} - \varepsilon_{pre}$. Feature formation either by compression or tension ($|\varepsilon_{app}| > \varepsilon_{pre}$) yields grating features with peak-to-trough amplitudes of A > 400 nm. Topographic features produced from pre-strained PDMS-SiO_2 bilayer substrates in this study were consistent with constitutive relationships in Eqns. 3.1-3.3. Releasing the pre-strain produces a net compressive strain $\varepsilon_{app} < \varepsilon_{pre}$ and a uniaxial grating array that is oriented orthogonally to the axis of the applied strain. Orthogonal features have an average amplitude of $A_\perp = 429.3 \pm 5.8$ nm and $\lambda_\perp = 4.95 \pm 0.36$ mm (Figure 3.2). Applying a strain ε_{app} such that $\Delta\varepsilon$ = 0% abolishes the grating. Tensile strains of $\Delta\varepsilon = \varepsilon_{app} - \varepsilon_{pre} > 3\%$ produce grating arrays parallel to the axis of applied strain. Parallel features have an average amplitude of $A_\parallel = 483.6 \pm 7.8$ nm and $\lambda_\parallel = 4.78 \pm 0.16$ mm. Features emerge for strains as small as $\Delta\varepsilon = |\varepsilon_{app} - \varepsilon_{pre}| = 3\%$. Fast Fourier Transforms (FFT) of optical micrographs are shown in Figure 3.1b. The intensity and orientation of these data confirm the presence (absence) and orientation of grating arrays under compression, tension, and zero-strain states. The feature amplitude A is also a strong function of the SiO_2 membrane thickness h_f. Optical and scanning probe micrographs of PDMS-SiO_2 bilayer substrates with h_f = 10 nm, pre-strain of ε_{pre} = +3%, and an applied strain of $\Delta\varepsilon$ = -3% produce random isotropic features with no short-range order and an Rms roughness of 0.317 ± 0.048 nm (Figure 3.2). Strain-dependent topography can be cycled without any observed hysteresis in feature size. “Strain cycles could likely be

repeated dozens of times without any fatigue or fracture of the SiO_2 membrane or mechanical failure of the PDMS substrate." PDMS-SiO_2 bilayer substrates formed by thermal evaporation of SiO_2 membranes offer additional advantages for use in dynamic presentation of substrate topography. First, the minimum critical strain ε_c is reduced, which minimizes crosstalk from mechanical stimuli during quantification of cytoskeleton remodeling.[27] Second, small strains can alter the surface topography between three discrete states: flat (*F*), orthogonal wavy ($W_\perp$), and parallel wavy ($W_\parallel$). The precise selection of the SiO_2 membrane permits facile fabrication of control substrates that are identical to dynamic topography substrates in terms of surface chemistry and applied strain. Lastly, topography can be presented both rapidly (~5 sec) and reversibly without indirectly impacting feature geometry.

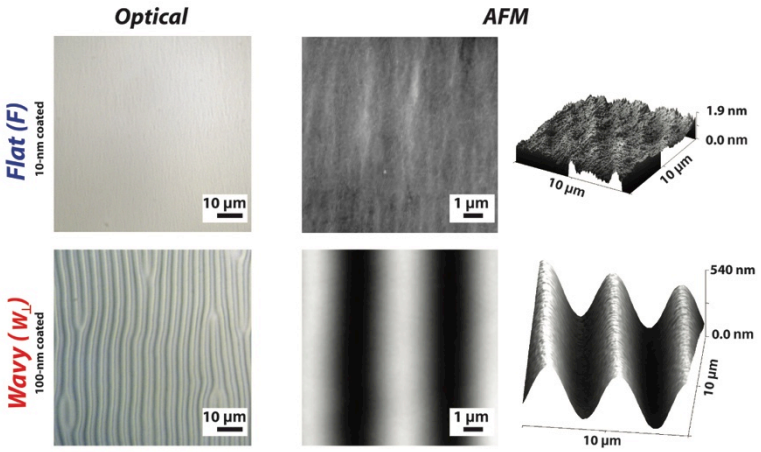

Figure 3.2 PDMS coupons are pre-strained to ε_{pre} = +3% and SiO_2 membranes of thickness h_f are deposited on elastomeric substrates. The pre-strain is released such that $\Delta\varepsilon$ = -3% prior to characterization. SiO_2 membranes with h_f = 100 nm generate flat (F) surfaces, while SiO_2 membranes with h_f = 100 nm generate substrates with perpendicular gratings ($W_\perp$).

3.4.b Morphological Responses of Fibroblasts to Static Topography

FB cultured on static flat (Static *F*) exhibit a more rounded morphology and random spreading compared to the aligned morphologies of fibroblasts cultured on static grating arrays (Wavy *W*) as assessed by fluorescent microscopy (Figure 3.3). Four parameters were used to quantify FB morphology: circularity C_{cell}, ratio of major-to-minor axes R_{axis}, projected area A_{proj}, and angle of major axis to grating direction θ_{align}.[17,24] FB cultured on flat substrates exhibit a larger average cell circularity (0.30 ± 0.13 versus 0.15 ± 0.08; $p<0.001$) and a higher average angle between the major axis of the cell and the features compared to topographic substrates (43.25° ± 23.40° versus 15.22° ± 13.10°; *** p <0.001) (Figure 3.4). These results suggest that static surfaces with grating topography can recapitulate the highly conserved morphological response of mammalian cells to grating features that is associated with contact guidance.[16] These measurements produce a baseline to compare the evolution of FB cytoskeleton morphology on substrates with dynamic topography.

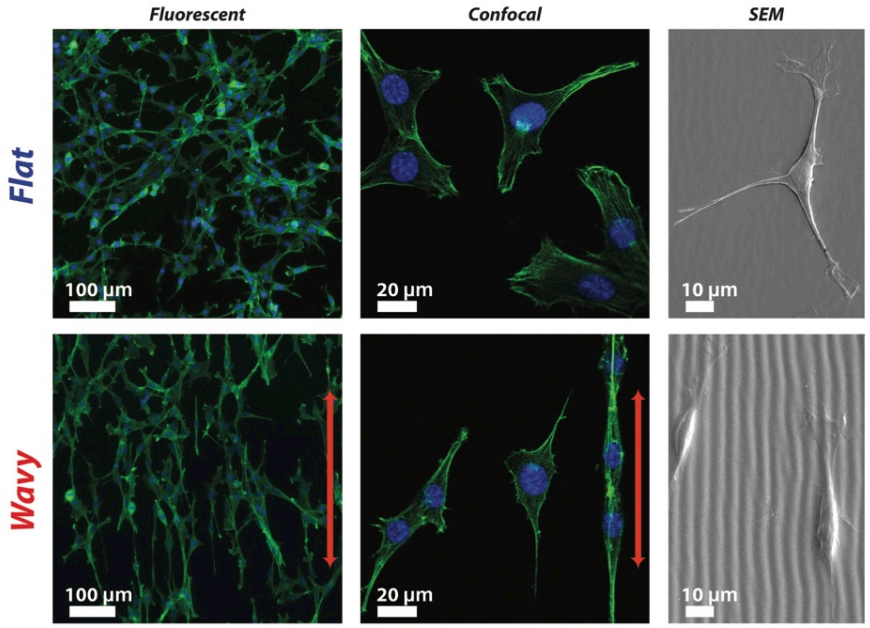

Figure 3.3 Fibroblast morphology and orientation on static flat (*F*) and static wavy gratings (*W*). Fibroblasts are fixed on PDMS-SiO_2 bilayers for 24 h prior to characterization. Micrographs suggest that fibroblasts were randomly oriented on static flat (*F*) substrates and aligned to wavy gratings (*W*). The direction of the grating is indicated by the red arrows. Actin and nuclei are shown in green and blue, respectively.

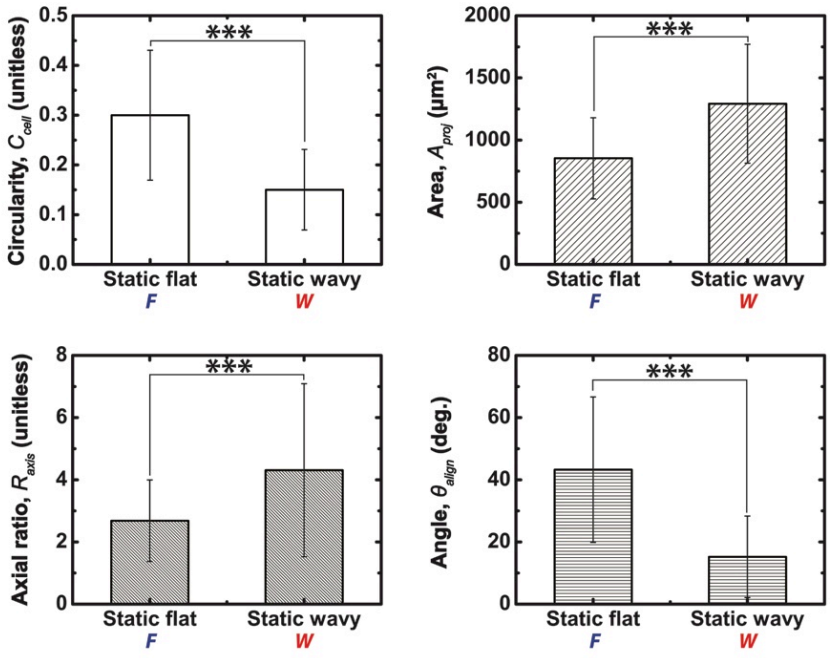

Figure 3.4 Quantification of fibroblast morphology and orientation on substrates with static flat (*F*) and static perpendicular gratings ($W_{\perp}$). Values of circularity C_{cell}, projected area A_{proj}, axial ratio R_{axis}, and alignment angle θ_{align} confirm that fibroblasts exhibit reduced spreading and increased alignment and orientation when cultured on $W_{\perp}$ substrates compared to *F* substrates (*** $p<0.001$).

3.4.c Cell Culture on Substrates with Programmable Topography

Many mammalian cell phenotypes respond to dynamic topographical features through cytoskeleton reorganization.[37] The strain detection threshold for mammalian cells in response to uniaxial stretching is ε_{cycle} = 3.5% as inferred by gross morphological characterization.[51,58] This threshold provides a benchmark to limit the maximum applies strains to $|\Delta\varepsilon| < 3.5\%$. Nevertheless, applying strain in sub-threshold regimes may still impact other as of yet unknown aspects of cell-materials interactions. Therefore, several substrate topography sequences were utilized to assess the potential

impact of strains in the sub-threshold regime. Static substrates that are either Flat (*F*) or Wavy (*W*) are mapped to corresponding dynamic substrates with the following sequences: $FW_{\perp}F$ and $FW_{\perp}$. Substrates with $FW_{\perp}F$ sequences are critical control conditions to measure the potential impact of the transient strain on the downstream cytoskeleton morphodynamics. Furthermore, a direct comparison between sequences of $FW_{\perp}F$ and $FW_{\perp}$ can isolate the direct impact of dynamic topography presentation on cytoskeleton morphology. FB morphology was largely preserved immediately after applied strains of $\Delta\varepsilon$ = ±3% (Figure 3.5). The orthogonal and parallel axes refer to the relative orientation of the grating features to the direction of applied strain. The morphology of FB cultured on PDMS substrates coated with 10 nm SiO_2 membranes was measured for $t \leq 6$ h (Figure 3.6). PDMS substrates with SiO_2 membranes of h_f = 10 nm , ε_{pre} = +3%, and $\Delta\varepsilon$ = -3% exhibit random gratings with feature sizes of A = 1.53 ± 0.55 nm and l = 1.8 ± 0.1 μm. These features do not significantly alter FB morphology via contact guidance mechanisms since the feature heights are smaller than 35 nm, the previously reported detection limit for contact guidance.[11] PDMS substrates with 10 nm SiO_2 membranes serve as valuable control materials since the strain and chemistry of the substrate are identical to PDMS-SiO_2 bilayers that with thicker SiO_2 membranes. Maintaining constant material properties in dynamic substrates can be challenging.[33] Thin film deposition and precise strains achieve dynamic programmable topography while preserving many of the other physicochemical aspects of the cellular microenvironment.

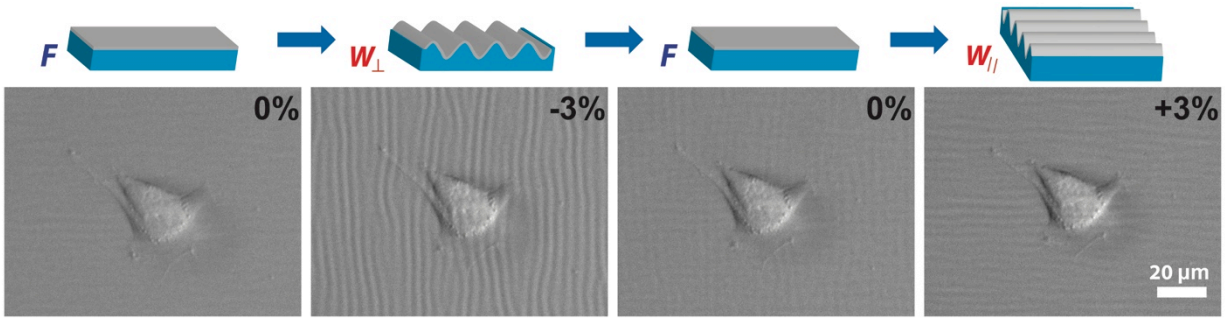

Figure 3.5 Transient response of isolated fibroblast in response to PDMS-SiO_2 bilayers cycled through discrete states of substrate topography. The applied strain is applied rapidly to achieve the following configurations: The strain is sequentially and quickly applied across the following values: $\Delta\varepsilon$ = 0% generates flat substrates (F) with no grating features; $\Delta\varepsilon$ = +3% produces perpendicular wavy grating arrays $(W_{\perp})$; $\Delta\varepsilon$ = -3% produces wavy grating arrays that are parallel to the axis of applied strain $(W_{\parallel})$. The rapid switching of substrate topographies does not induce observable morphological changes in FB over the span of 30 sec.

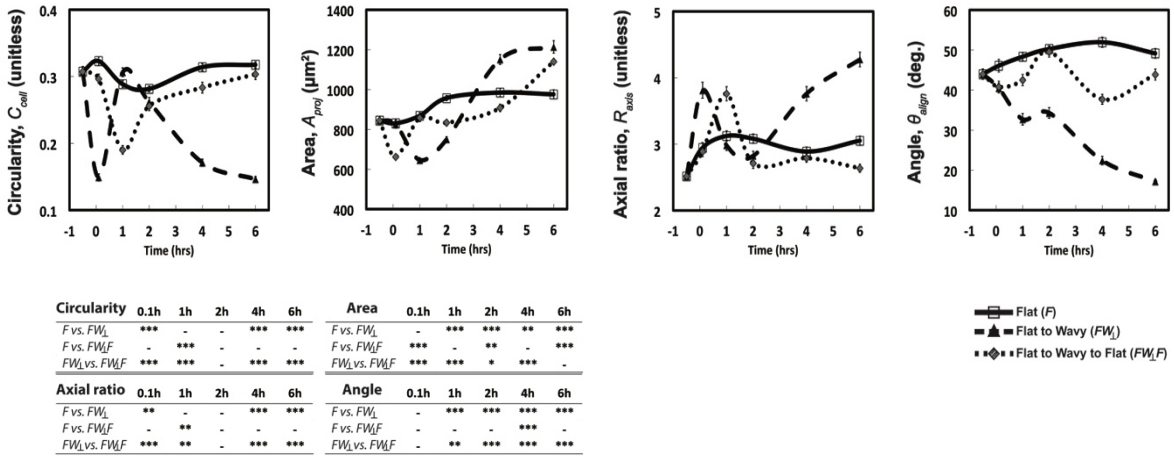

Circularity	0.1h	1h	2h	4h	6h
F vs. $FW_{\perp}$	***	-	-	***	***
F vs. $FW_{\perp}F$	-	***	-	-	-
$FW_{\perp}$ vs. $FW_{\perp}F$	***	***	-	***	***

Area	0.1h	1h	2h	4h	6h
F vs. $FW_{\perp}$	-	***	***	**	***
F vs. $FW_{\perp}F$	***	-	**	-	***
$FW_{\perp}$ vs. $FW_{\perp}F$	***	***	*	***	-

Axial ratio	0.1h	1h	2h	4h	6h
F vs. $FW_{\perp}$	**	-	-	***	***
F vs. $FW_{\perp}F$	-	**	-	-	-
$FW_{\perp}$ vs. $FW_{\perp}F$	***	**	-	***	***

Angle	0.1h	1h	2h	4h	6h
F vs. $FW_{\perp}$	-	***	***	***	***
F vs. $FW_{\perp}F$	-	-	-	***	-
$FW_{\perp}$ vs. $FW_{\perp}F$	-	**	***	***	***

Figure 3.6 Cytoskeleton morphodynamics for FB cultured on substrates over the course of 6 h with the following sequences are shown: Static flat (F), dynamic flat to wavy

grating ($FW_{\perp}$), and dynamic flat to wavy grating back to flat ($FW_{\perp}F$). Results of one-way ANOVA with Tukey post hoc tests are summarized in the table.

After 24 h of cell seeding (*t* = 0 h), the surface topography is switched either from flat to wavy ($FW_{\perp}$) or flat to wavy to flat ($FW_{\perp}F$) in rapid succession. The dynamic presentation of substrate topography induces alterations in FB morphology that initiate within 6 min and persist for *t* > 6 h (Figure 3.6). The circularity and ratio of major/minor axes of the $FW_{\perp}$ both exhibit a significant change within 5 min of substrate actuation (** *p* < 0.01), while the average projected area *A* and major axis angle exhibit significant differences within 1 hour (** *p* < 0.001). Substrates with $FW_{\perp}F$ programs present gratings briefly (5 ± 3 sec). FB cultured on $FW_{\perp}F$ programs exhibit cytoskeleton dynamics that are substantially different compared to Static *F* substrates. $FW_{\perp}F$ sequences induce transient alterations in the following parameters that are associated with elongated morphologies: circularity C_{cell}, projected area A_{proj}, and axial ratio R_{axis}. Values for C_{cell} and R_{axis} in FB populations cultured on substrates with $FW_{\perp}F$ sequences converge to values observed in cells on Static *F* substrates for *t* ≤ 2 h. These results suggest that sub-threshold strains induce transient fluctuations in morphological response. Temporary presentation of topographical cues may engage memory mechanisms in mammalian cells that have been previously reported in the context of other types of dynamic cell-materials interactions.[61]

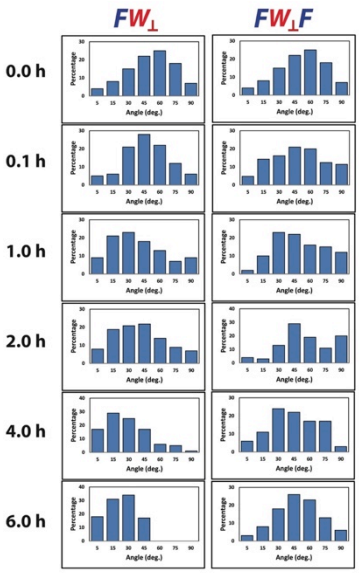

Figure 3.7 Dynamic change in the average alignment angle θ_{align} of fibroblasts over 6 h on substrates with the following topographic sequences: dynamic flat to wavy grating ($FW_\perp$); dynamic flat to wavy grating back to flat ($FW_\perp F$). These data demonstrate the gradual shift in alignment for $FW_\perp$ sequences compared to unperturbed distributions in $FW_\perp F$ sequences.

Substrates with $FW_\perp$ sequences yield morphological changes in FB that are internally consistent with other observations within this study. Substrate actuation via compressive strains is comparable between $FW_\perp$ and $FW_\perp F$ sequences. FB cultured on substrates with $FW_\perp$ sequences adopt a temporary rounded morphology that is manifested by a transient decrease in A_{proj} for t = 1 h (*** $p < 0.001$), a decrease in C_{cell} at t = 0.1 h (*** $p < 0.001$), and an increase in R_{axis} at t = 0.1 h (** $p < 0.01$) compared to Static *F* substrates (Figure 3.6). The morphology of FB cultured on substrates with $FW_\perp$ sequences for $t \geq 6$ h compared to Static *F* substrates approximate that of Static *W*

compared to Static *F.* These results suggest that steady state FB morphology is achieved within 6 h.

3.4.d Single Cell Sensing on Programmable Substrates

Programmable substrates can measure the cytoskeleton morphology of individual FB to transiently altered strain-induced topography. Isolated FB alter their shape and orientation for $t \leq 1$ h. Single cell morphological responses observed in FB populations cultured on substrates with $FW_{\perp}$ and $FW_{\perp}F$ sequences are shown in Figure 3.8. FB alignment and elongation occurs for $t < 2$ h for $FW_{\perp}$ sequences. FB cultured on substrates with $FW_{\perp}F$ sequences extend lamellipodia in seemingly random directions within $t < 2$ h. Single-cell morphodynamics are consistent with morphological observations made in FB populations. A notable observation is that both $FW_{\perp}$ and $FW_{\perp}F$ sequences induce an initial temporary phase of cell rounding immediately after substrate actuation. This observation is curious because the minimum apparent strain detection threshold during cyclic stretching is $\varepsilon_{cycle} = 3.5\%$. Furthermore, the strains applied in this system are approximately 1 order of magnitude smaller than other experiments that employ dynamic strain. Typical cyclic strain experiments require uniaxial substrate strains of $\varepsilon_{cycle} > 10\%$.[42] Furthermore, the impact of mechanical stress on cytoskeleton dynamics typically results in strains of $\gamma \sim 20\%$.[18,66] It is unlikely that the application of transient strains will directly impact binding between integrins and adhesion-promoting peptides because of the strength of these bonds.[39] Typical dissociation constants for this specific kind of receptor-ligand interaction is on the order of $K_D = 10^{-9}$ M, which corresponds to a characteristic binding distance of $r_0 = 3$ nm.[39]

Considering the characteristic dimension of integrins is ~10 nm[9], it is likely that 3% strains will not dissociate integrin-peptide coupling. Dynamic topography presentation may, however, alter other downstream effectors of cell-matrix interactions. Transient substrate strains may disrupt focal adhesions or cytoskeleton proteins that induce an altered state in which the cell rapidly interrogates the local chemical and topographical microenvironments by forming nascent integrins.[3] This topic is the subject of ongoing research.

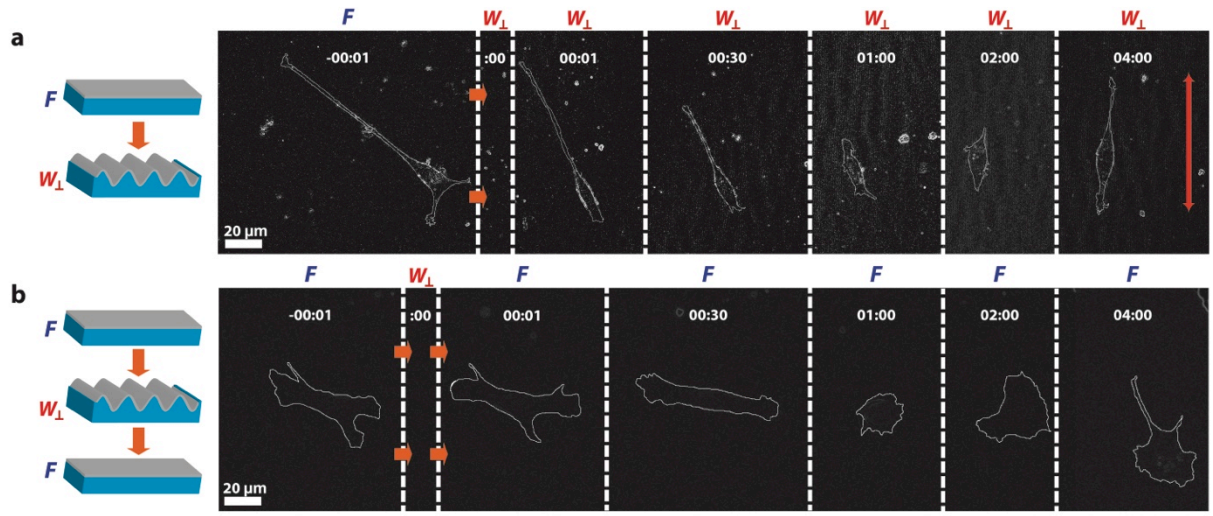

Figure 3.8 Morphodynamics of a single FB in response to substrate perturbations. Single cells are captured before and after topographical switching, indicated at zero time point (:00). Phase contrast micrographs are processed using ImageJ to depict changes of cellular shape and orientation. Substrates are programmed with the following sequences: (a) flat to perpendicular wavy grating ($FW_{\perp}$); (b) flat to perpendicular wavy grating back to flat substrates ($FW_{\perp}F$).

3.4.e Topographic Elastomeric Cylinders

Microgrooves were successfully generated on PDMS substrates and elastomeric cylinders. The mechanical pre-strain at 30% and UV ozone produce wavy patterns that have wavelength of 6.97 ± 0.21 μm and amplitude of 36.47 ± 1.44 μm on PDMS. The pattern was replicated on PGS-CinA cylinder, as shown in Figure 3.9.

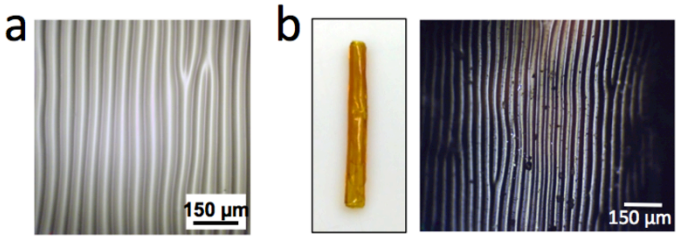

Figure 3.9 Topographic PDMS and PGS-CinA cylinders. Microwavy pattern was successfully transferred from PDMS (a) to PGS-CinA cylinders (b).

3.4.f Contraction of Skin Bridge Length in Mouse Model

In addition to the control of in vitro cell morphodynamics, topographic patterns were incorporated to percutaneous device to investigate host response. Our preliminary results in Figure 3.10 show that the topographic percutaneous implants significantly changed the contraction rate of skin bridge length in two weeks after a surgery, compared to implants with smooth surface (Kruskal-Wallis, $p < 0.05$). The higher rate of skin bridge contraction might be attributed to tissue-topography interactions that accelerate tissue migration disregarding of the microgroove alignment. The higher migration rate disagrees with many in vitro experiments that reported slower migration rate using microgrooves aligned perpendicular to cell migration direction.[13,61] The result suggests that in vitro collective cell migration might not well represent actual in vivo tissue migration, and microgrooves might not be a promising way to control epidermal downgrowth in percutaneous devices.

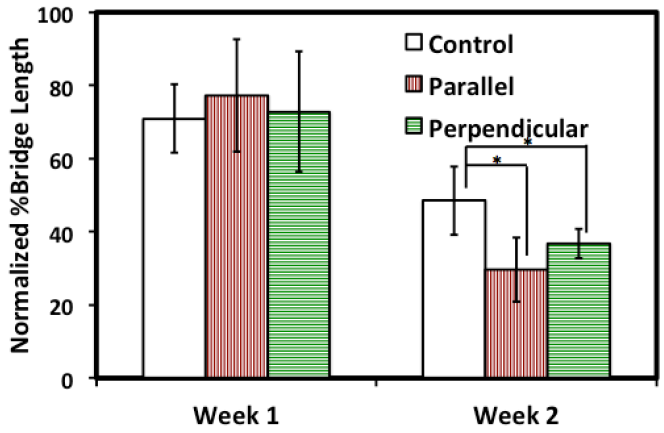

Figure 3.10 Normalized percentage of skin bridge length. Bars and error bars represent means and standard deviation. (*p <0.05, Kruskal-Wallis) (n=4)

3.5 Conclusions

We describe a lithography-free approach to fabricate dynamic substrate topography for measuring morphodynamics of cells during contact guidance. This substrate is advantageous because it presents ordered topographical cues in a manner that decouples potential contributions from other stimuli including substrate chemistry and large mechanical strains. Homogeneous surface chemistry (SiO_2) and small required extensive strains (~3%) are key features of the approach described herein. Although the substrate cannot completely eliminate the effect of external mechanical stimuli on in vitro cell-topography interactions, using small strains minimizes the impact of the applied stimulus. This work represents a strategy to better isolate the effect of dynamic programmable topography on living cells. Furthermore, this technique permits rapid and reversible presentation of topographic cues with precise temporal precision. Dynamic substrate topography afforded by the strategy described herein could be

further applied to studying signal transduction pathways that original from transient cell-matrix interactions and propagate to downstream pathways that control cytoskeleton reorganization. Thus, programmable substrate topography is a promising strategy to elucidate cytoskeleton remodeling dynamics in many cell phenotypes in the context of cell-biomaterials interactions.

References:

1. Barranco, A., F. Yubero, J. P. Espinós, P. Groening, and A. R. González-Elipe. Electronic state characterization of SiOx thin films prepared by evaporation. *J. Appl. Phys.* 97:113714, 2005.
2. Béfahy, S., P. Lipnik, T. Pardoen, C. Nascimento, B. Patris, P. Bertrand, and S. Yunus. Thickness and elastic modulus of plasma treated PDMS silica-like surface layer. *Langmuir ACS J. Surf. Colloids* 26:3372–5, 2010.
3. Beningo, K. A., M. Dembo, I. Kaverina, J. V. Small, and Y. Wang. Nascent Focal Adhesions Are Responsible for the Generation of Strong Propulsive Forces in Migrating Fibroblasts. *J. Cell Biol.* 153:881–888, 2001.
4. Biela, S. A., Y. Su, J. P. Spatz, and R. Kemkemer. Different sensitivity of human endothelial cells, smooth muscle cells and fibroblasts to topography in the nano-micro range. *Acta Biomater.* 5:2460–6, 2009.
5. Bowden, N., S. Brittain, A. G. Evans, J. W. Hutchinson, and G. M. Whitesides. Spontaneous formation of ordered structures in thin films of metals supported on an elastomeric polymer. 393:146–149, 1998.
6. Box, F., R. Bowman, and T. Mullin. Dynamic compression of elastic and plastic cellular solids. *Appl. Phys. Lett.* 103:151909, 2013.
7. Cheng, C.-M., R. L. Steward, and P. R. LeDuc. Probing cell structure by controlling the mechanical environment with cell-substrate interactions. *J. Biomech.* 42:187–92, 2009.
8. Chua, J. S., C.-P. Chng, A. A. K. Moe, J. Y. Tann, E. L. K. Goh, K.-H. Chiam, and E. K. F. Yim. Extending neurites sense the depth of the underlying topography during neuronal differentiation and contact guidance. *Biomaterials* 35:7750–7761, 2014.
9. Comisar, W. A., D. J. Mooney, and J. J. Linderman. Integrin Organization: Linking Adhesion Ligand Nanopatterns with Altered Cell Responses. *J. Theor. Biol.* 274:120–130, 2011.
10. Dalby, M. J., M. O. Riehle, H. Johnstone, S. Affrossman, and A. S. G. Curtis. Investigating the limits of filopodial sensing: a brief report using SEM to image the interaction between 10 nm high nano-topography and fibroblast filopodia. *Cell Biol. Int.* 28:229–36, 2004.
11. Dalby, M. J., M. O. Riehle, H. J. H. Johnstone, S. Affrossman, and A. S. G. Curtis. Polymer-Demixed Nanotopography: Control of Fibroblast Spreading and Proliferation. *Tissue Eng.* 8:1099–1108, 2002.
12. Dalby, M. J., M. O. Riehle, D. S. Sutherland, H. Agheli, and A. S. G. Curtis. Changes in fibroblast morphology in response to nano-columns produced by colloidal lithography. *Biomaterials* 25:5415–5422, 2004.
13. Dalton, B. A., X. F. Walboomers, M. Dziegielewski, M. D. M. Evans, S. Taylor, J. A. Jansen, and J. G. Steele. Modulation of epithelial tissue and cell migration by microgrooves. *J. Biomed. Mater. Res.* 56:195–207, 2001.

14. Davidson, P., M. Bigerelle, B. Bounichane, M. Giazzon, and K. Anselme. Definition of a simple statistical parameter for the quantification of orientation in two dimensions: application to cells on grooves of nanometric depths. *Acta Biomater.* 6:2590–8, 2010.
15. Davis, K. A., K. A. Burke, P. T. Mather, and J. H. Henderson. Dynamic cell behavior on shape memory polymer substrates. *Biomaterials* 32:2285–93, 2011.
16. van Delft, F. C. M. J. M., F. C. van den Heuvel, W. A. Loesberg, J. te Riet, P. Schön, C. G. Figdor, S. Speller, J. J. W. A. van Loon, X. F. Walboomers, and J. A. Jansen. Manufacturing substrate nano-grooves for studying cell alignment and adhesion. *Microelectron. Eng.* 85:1362–1366, 2008.
17. den Braber, E. T., J. E. de Ruijter, L. A. Ginsel, A. F. von Recum, and J. A. Jansen. Quantitative analysis of fibroblast morphology on microgrooved surfaces with various groove and ridge dimensions. *Biomaterials* 17:2037–2044, 1996.
18. Ehrlicher, A. J., F. Nakamura, J. H. Hartwig, D. A. Weitz, and T. P. Stossel. Mechanical strain in actin networks regulates FilGAP and integrin binding to filamin A. *Nature* 478:260–263, 2011.
19. Ferrari, A., M. Cecchini, M. Serresi, P. Faraci, D. Pisignano, and F. Beltram. Neuronal polarity selection by topography-induced focal adhesion control. *Biomaterials* 31:4682–94, 2010.
20. Flemming, R. G., C. J. Murphy, G. A. Abrams, S. L. Goodman, and P. F. Nealey. Effects of synthetic micro- and nano-structured surfaces on cell behavior. *Biomaterials* 20:573–88, 1999.
21. Franco, D., F. Milde, M. Klingauf, F. Orsenigo, E. Dejana, D. Poulikakos, M. Cecchini, P. Koumoutsakos, A. Ferrari, and V. Kurtcuoglu. Accelerated endothelial wound healing on microstructured substrates under flow. *Biomaterials* 34:1488–97, 2013.
22. Guvendiren, M., and J. A. Burdick. Engineering synthetic hydrogel microenvironments to instruct stem cells. *Curr. Opin. Biotechnol.* 24:841–6, 2013.
23. Hakkinen, K. M., J. S. Harunaga, A. D. Doyle, and K. M. Yamada. Direct comparisons of the morphology, migration, cell adhesions, and actin cytoskeleton of fibroblasts in four different three-dimensional extracellular matrices. *Tissue Eng. Part A* 17:713–24, 2011.
24. Han, L., Z. Mao, J. Wu, Y. Guo, T. Ren, and C. Gao. Unidirectional migration of single smooth muscle cells under the synergetic effects of gradient swelling cue and parallel groove patterns. *Colloids Surf. B Biointerfaces* 111C:1–6, 2013.
25. Harrison, C., C. M. Stafford, W. Zhang, and A. Karim. Sinusoidal phase grating created by a tunably buckled surface. *Appl. Phys. Lett.* 85:4016–4018, 2004.
26. Houtchens, G. R., M. D. Foster, T. A. Desai, E. F. Morgan, and J. Y. Wong. Combined effects of microtopography and cyclic strain on vascular smooth muscle cell orientation. *J. Biomech.* 41:762–9, 2008.
27. Hui, E. E., and S. N. Bhatia. Micromechanical control of cell–cell interactions. *Proc. Natl. Acad. Sci.* 104:5722–5726, 2007.
28. Idota, N., T. Tsukahara, K. Sato, T. Okano, and T. Kitamori. The use of electron beam lithographic graft-polymerization on thermoresponsive polymers for regulating the directionality of cell attachment and detachment. *Biomaterials* 30:2095–101, 2009.
29. Jiang, H., D.-Y. Khang, J. Song, Y. Sun, Y. Huang, and J. A. Rogers. Finite deformation mechanics in buckled thin films on compliant supports. *Proc. Natl. Acad. Sci. U. S. A.* 104:15607–12, 2007.
30. Kaunas, R., P. Nguyen, S. Usami, and S. Chien. Cooperative effects of Rho and mechanical stretch on stress fiber organization. *Proc. Natl. Acad. Sci. U. S. A.* 102:15895–900, 2005.
31. Kim, H. N., A. Jiao, N. S. Hwang, M. S. Kim, D. H. Kang, D.-H. Kim, and K.-Y. Suh. Nanotopography-guided tissue engineering and regenerative medicine. *Adv. Drug Deliv. Rev.* 65:536–58, 2013.
32. Kim, J., and R. C. Hayward. Mimicking dynamic in vivo environments with stimuli-responsive materials for cell culture. *Trends Biotechnol.* 30:426–39, 2012.
33. Kloxin, A. M., M. W. Tibbitt, and K. S. Anseth. Synthesis of photodegradable hydrogels as dynamically tunable cell culture platforms. *Nat. Protoc.* 5:1867–87, 2010.
34. Kolind, K., D. Kraft, T. Bøggild, M. Duch, J. Lovmand, F. S. Pedersen, D. A. Bindslev, C. E. Bünger, M. Foss, and F. Besenbacher. Control of proliferation and osteogenic differentiation of human dental-pulp-derived stem cells by distinct surface structures. *Acta Biomater.* 10:641–50, 2014.
35. Koo, S., R. Muhammad, G. S. L. Peh, J. S. Mehta, and E. K. F. Yim. Micro- and nanotopography with extracellular matrix coating modulate human corneal endothelial cell behavior. *Acta Biomater.* 10:1975–84, 2014.

36. Lam, M. T., W. C. Clem, and S. Takayama. Reversible on-demand cell alignment using reconfigurable microtopography. *Biomaterials* 29:1705–12, 2008.
37. Lamb, B. M., and M. N. Yousaf. Redox-switchable surface for controlling peptide structure. *J. Am. Chem. Soc.* 133:8870–3, 2011.
38. Lauffenburger, D. A. Receptors: Models for Binding, Trafficking, and Signaling. New York: Oxford University Press, 1996, 376 pp.
39. Leclerc, A., D. Tremblay, S. Hadjiantoniou, N. V Bukoreshtliev, J. L. Rogowski, M. Godin, and A. E. Pelling. Three dimensional spatial separation of cells in response to microtopography. *Biomaterials* 34:8097–104, 2013.
40. Lü, D., C. Luo, C. Zhang, Z. Li, and M. Long. Differential regulation of morphology and stemness of mouse embryonic stem cells by substrate stiffness and topography. *Biomaterials* 35:3945–55, 2014.
41. Morioka, M., H. Parameswaran, K. Naruse, M. Kondo, M. Sokabe, Y. Hasegawa, B. Suki, and S. Ito. Microtubule Dynamics Regulate Cyclic Stretch-Induced Cell Alignment in Human Airway Smooth Muscle Cells. *PLoS ONE* 6:e26384, 2011.
42. Nikkhah, M., F. Edalat, S. Manoucheri, and A. Khademhosseini. Engineering microscale topographies to control the cell–substrate interface. *Biomaterials* 33:5230–5246, 2012.
43. Ohzono, T., and H. Monobe. Microwrinkles: shape-tunability and applications. *J. Colloid Interface Sci.* 368:1–8, 2012.
44. Pholpabu, P., S. Kustra, H. Wu, A. Balasubramanian, and C. J. Bettinger. Lithography-free fabrication of reconfigurable substrate topography for contact guidance. *Biomaterials* 39:164–172, 2015.
45. Quero, J. M., F. Perdigones, and C. Aracil. Smart Sensors and Mems. Elsevier, 2014.doi:10.1533/9780857099297.2.281
46. Seo, C. H., H. Jeong, K. S. Furukawa, Y. Suzuki, and T. Ushida. The switching of focal adhesion maturation sites and actin filament activation for MSCs by topography of well-defined micropatterned surfaces. *Biomaterials* 34:1764–71, 2013.
47. Sheets, K., S. Wunsch, C. Ng, and A. S. Nain. Shape-dependent cell migration and focal adhesion organization on suspended and aligned nanofiber scaffolds. *Acta Biomater.* 9:7169–77, 2013.
48. Shih, T.-K., J.-R. Ho, H.-Y. Liao, C.-F. Chen, and C.-Y. Liu. Fabrication of optical gratings by shrinkage of a rubber material. *Thin Solid Films* 516:5339–5343, 2008.
49. Song, G., Y. Ju, X. Shen, Q. Luo, Y. Shi, and J. Qin. Mechanical stretch promotes proliferation of rat bone marrow mesenchymal stem cells. *Colloids Surf. B Biointerfaces* 58:271–7, 2007.
50. Song, J., H. Jiang, Y. Huang, and J. A. Rogers. Mechanics of stretchable inorganic electronic materials. *J. Vac. Sci. Technol. A* 27:1107–1125, 2009.
51. Spivey, E. C., Z. Z. Khaing, J. B. Shear, and C. E. Schmidt. The fundamental role of subcellular topography in peripheral nerve repair therapies. *Biomaterials* 33:4264–76, 2012.
52. Straley, K. S., and S. C. Heilshorn. Dynamic, 3D-Pattern Formation Within Enzyme-Responsive Hydrogels. *Adv. Mater.* 21:4148–4152, 2009.
53. Tzvetkova-Chevolleau, T., A. Stéphanou, D. Fuard, J. Ohayon, P. Schiavone, and P. Tracqui. The motility of normal and cancer cells in response to the combined influence of the substrate rigidity and anisotropic microstructure. *Biomaterials* 29:1541–51, 2008.
54. Walboomers, X. F., W. Monaghan, A. S. Curtis, and J. A. Jansen. Attachment of fibroblasts on smooth and microgrooved polystyrene. *J. Biomed. Mater. Res.* 46:212–20, 1999.
55. Watari, S., K. Hayashi, J. A. Wood, P. Russell, P. F. Nealey, C. J. Murphy, and D. C. Genetos. Modulation of osteogenic differentiation in hMSCs cells by submicron topographically-patterned ridges and grooves. *Biomaterials* 33:128–36, 2012.
56. Winston, F. K., E. J. Macarak, S. F. Gorfien, and L. E. Thibault. A system to reproduce and quantify the biomechanical environment of the cell. *J. Appl. Physiol. Bethesda Md 1985* 67:397–405, 1989.
57. Wong, J. Y., J. B. Leach, and X. Q. Brown. Balance of chemistry, topography, and mechanics at the cell–biomaterial interface: Issues and challenges for assessing the role of substrate mechanics on cell response. *Surf. Sci.* 570:119–133, 2004.
58. Wu, H., S. Kustra, E. M. Gates, and C. J. Bettinger. Topographic substrates as strain relief features in stretchable organic thin film transistors. *Org. Electron.* 14:1636–1642, 2013.
59. Yang, C., M. W. Tibbitt, L. Basta, and K. S. Anseth. Mechanical memory and dosing influence stem cell fate. *Nat. Mater.* 13:645–52, 2014.

60. Yang, P., R. M. Baker, J. H. Henderson, and P. T. Mather. In vitro wrinkle formation via shape memory dynamically aligns adherent cells. *Soft Matter* 9:4705, 2013.
61. Yim, E. K. F., R. M. Reano, S. W. Pang, A. F. Yee, C. S. Chen, and K. W. Leong. Nanopattern-induced changes in morphology and motility of smooth muscle cells. *Biomaterials* 26:5405–5413, 2005.
62. Yu, C., and H. Jiang. Forming wrinkled stiff films on polymeric substrates at room temperature for stretchable interconnects applications. *Thin Solid Films* 519:818–822, 2010.
63. Zhao, G., A. L. Raines, M. Wieland, Z. Schwartz, and B. D. Boyan. Requirement for both micron- and submicron scale structure for synergistic responses of osteoblasts to substrate surface energy and topography. *Biomaterials* 28:2821–9, 2007.
64. Zhu, X., K. L. Mills, P. R. Peters, J. H. Bahng, E. H. Liu, J. Shim, K. Naruse, M. E. Csete, M. D. Thouless, and S. Takayama. Fabrication of reconfigurable protein matrices by cracking. *Nat. Mater.* 4:403–406, 2005.

CHAPTER 4 CONTROLLED RELEASE OF SMALL MOLECULES FROM ELASTOMERS FOR REDUCING EPIDERMAL DOWNGROWTH IN PERCUTANEOUS DEVICES

The content in this chapter in whole or in part has been previously published in *ACS Biomaterials Science & Engineering*. [Pholpabu, P., S. S. Yerneni, C. Zhu, P. G. Campbell, and C. J. Bettinger. Controlled Release of Small Molecules from Elastomers for Reducing Epidermal Downgrowth in Percutaneous Devices. *ACS Biomater. Sci. Eng.*, 2016.][42]

4.1 Abstract

The elevated infection rise associated with indwelling devices can compromise the performance of percutaneous devices and increase the risk of complications. High infection rates are associated with both the high bacterial load on the skin and epidermal downgrowth at the interface of the indwelling material. Here we propose a drug-eluting material that promotes local dermal regeneration to reduce epidermal downgrowth. Mesoporous elastomeric matrices composed of naturally occurring monomers were prepared by a combination of photo- and thermal- crosslinking. Elastomeric devices loaded with conjugated linoleic acids (CLA), a class of small molecules that promotes local anti-inflammatory responses, can deliver these compounds for 7 d ($D_{CLA\text{-}elastomer}$ = 3.94 x 10^{-9} cm^2/s, 95% CI [3.12 x 10^{-9}, 4.61 x 10^{-9}]). In a mouse model, CLA-eluting elastomeric matrices increase the M2 population (5.0 x 10^3 ± 1.4 x 10^3 cells/cm^2), compared to blank devices (3.8 x 10^3 ± 2.2 x 10^3 cells/cm^2), and also reduce skin contraction (98.9 ± 6.4 %), compared to blank devices (70.9 ± 9.3 %) at 7 d. Dermal downgrowth is also attenuated at 14 d (60.4 ± 32.4 μm) compared to

blank devices (171.7 ± 93.8 μm). CLA-eluting elastomers are therefore a viable strategy to reduce epidermal downgrowth in percutaneous devices.

4.2 Introduction

Indwelling catheters are important in healthcare because they provide transcorporal egress.[2,41] However, these medical devices are a major source of nosocomial bloodstream infection that gives rise to notable morbidity and mortality.[15,55] Percutaneous devices induce dermal migration downward along the skin-device interface and create recessed tissue circumferentially arranged about the device.[42] Dermal downgrowth and high bacterial loads increase the risk of bloodstream infection.[32] Previous strategies to reduce the skin-device mismatch primarily focus on microporous catheters to promote dermal integration.[18,52] Modulating local macrophage populations may offer another strategy for reducing epidermal downgrowth. Macrophages serve as a key component to regulate inflammation, regeneration, and remodeling. Attenuating pro-inflammatory (M1) macrophages and increasing regenerative (M2) macrophages may accelerate the healing processes and reduce epidermal downgrowth.[7,8] Local delivery of linoleic acid (LA) and its isomer, conjugated linoleic acid (CLA), is a viable approach for biasing macrophage populations. LA and CLA are small molecule agonists that polarize macrophages toward M2 phenotypes.[35,43,57] Furthermore, LA and CLA have molecular weight 280 g/mol and hydrodynamic radii between 2.8-3.1 Å.[22,23] thereby permitting delivery from mesoporous elastomeric matrices. Here we design the design and characterization of drug-eluting

elastomers for local delivery of macrophage modulating small molecules to reduce epidermal downgrowth in percutaneous devices.

4.3 Materials and Methods

Materials and Methods of this chapter are described in Chapter 2.

4.4 Results and discussion

4.4.a Mechanical Properties of PGS-CinA

Seamless tissue-device integration can attenuate epidermal downgrowth and reduce catheter-related bloodstream infections.[11,17,36] Elastomers composed of naturally occurring monomers are ideal because they are non-toxic and exhibit mechanical properties that match the dermis.[28,45,51,54,56] Cylindrical matrices were prepared from coupons composed of poly(glycerol-*co*-sebacate)-cinnamate (PGS-CinA), a photocrosslinkable elastomer that supports cell attachment and proliferation.[11,60] The Young's modulus of PGS-CinA prepared from sequential photocrosslinking and thermal crosslinking is $E_{PGS\text{-}CinA}$ = 54.33 ± 0.96 kPa, which is comparable to the dermis modulus (E_{dermis} ~ 56 kPa).[19,29] Elastomeric PGS-CinA matrices improve the mechanical matching at the tissue-device interface, which may reduce local injury due to micromotion artifacts and subsequently reduce the risk of device failure when compared to more rigid device materials such as medical grade silicone ($E_{silicone}$ = 8.7 ± 0.5 MPa) and polyvinylchloride (PVC; E_{PVC} = 17.8 ± 1.2 MPa).[12] The crosslink density of PGS-

CinA films that undergo successive photocrosslinking and thermal curing was calculated to be $n_{PGS\text{-}CinA}$ = 7.31 ± 0.77 mol/m^3, as described in Chapter 2.

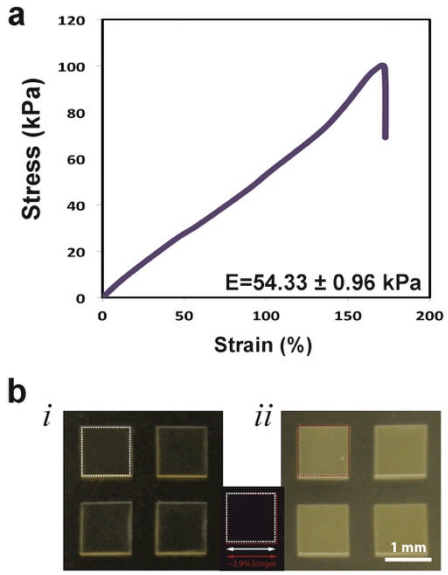

Figure 4.1 Mechanical and physical characterization of PGS-CinA elastomer. (a) The elastic modulus is calculated from the stress-strain plot of a PGS-CinA film. (b) Swelling ratio of PGS-CinA is quantified using microstructures with square geometries. The width of the microstructures is measured before (*i*) and after (*ii*) incubation in DI water for 24 hr at 37 °C to obtain values for L_d and L_s, respectively. The swelling ratio is calculated from $Q_{dim} = \left({}^{L_s}/_{L_d}\right)^3$ is 1.13 ± 0.01.

4.4.b Mesh Size

The release kinetics of small molecules is dependent upon the mesh size.[30,49] The mesh size ξ of crosslinked PGS-CinA networks is estimated to be $\xi_{PGS\text{-}CinA}$ = 37.3 ±

0.4 nm based upon the elastic modulus using the following equation described by Canal and Peppas.[10]

$$\xi = \phi^{-1/3} \left(\frac{15 C_n M_c}{M_r}\right)^{1/2} l \qquad \text{Eqn. 4.1}$$

In this expression, ϕ is the volume fraction of polymer in the equilibrium swollen polymer (reciprocal of the swelling ratio, $\phi^{-1} = Q_{dim}$ = 1.13 ± 0.01, calculated as described in Chapter 2), C_n is the characteristic ratio of the polymer (estimated to be 6 for polyesters composed primarily of alkyl chains)[16], M_r is the molecular weight of the repeat unit of the copolymer estimated from the PGS-CinA chemical structure ($M_{r,PGS\text{-}CinA}$ = 241 g/mol), l is the average C-C bond length, and M_c is the molecular weight of the repeat units between crosslinks ($M_{c,PGS\text{-}CinA}$ = 1.45 x 10^5 ± 0.10 x 10^5 g/mol). The value of M_c is determined by the following equation.[53]

$$N = \frac{E_{PGS-CinA}}{3RT} = \frac{\rho}{M_c} \qquad \text{Eqn. 4.2}$$

The parameter R is the universal gas constant, T is the absolute temperature, and ρ is the mass density of the PGS-CinA (1.06 ± 0.07 g/cm^3).

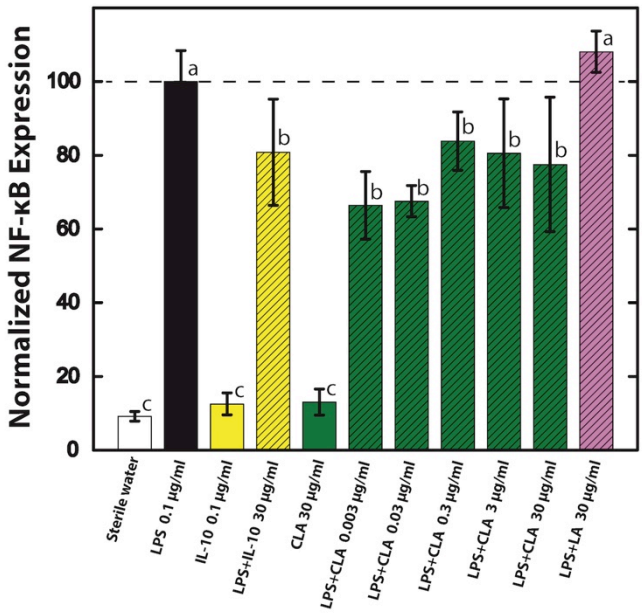

Figure 4.2 Inhibition of NF-κB activation by IL-10, CLA, and LA, measured by SEAP reporter assay. IL-10 and CLA have a comparable ability to dampen NF-κB expression induced by LPS. LA does not significantly reduce NF-κB expression level. Bars represent the mean ± SD, n=9. Different groups of values (a-c) are determined by one-way ANOVA and Tukey post-hoc test.

4.4.c Release Kinetics of LPS and CLA from Elastomeric Matrices

The release kinetics of CLA, LPS, and LPS+CLA from PGS-CinA matrices were measured. CLA was chosen as a macrophage-modulating agent because it is a small molecule that exhibits comparable NF-κB inhibition to IL-10, an anti-inflammatory cytokine and agent that biases macrophages toward M2 polarization (Figure 4.2).[14,33] In contrast, LA does not significantly reduce the macrophage inflammatory response. This is consistent with previous studies, which suggest LA cannot act as a ligand to peroxisome proliferator-activated receptor γ (PPARγ), a nuclear receptor the promotes

M2 macrophage differentiation.[4,6,44,46] LPS was included to this study to activate pro-inflammatory cytokines and recruit macrophages to the implantation site.[25,34] Local co-delivery of both LPS and CLA was tested to assess the potential increase in both overall macrophages and macrophages with M2 phenotypes when compared to CLA delivery alone. The release kinetics of LPS and CLA from solid cylindrical elastomeric PGS-CinA matrices is shown in Figure 4.3. LPS-loaded matrices release 986 ± 23 pg of LPS within 1 hr, which represents more than 95% of the total releasing LPS. The observed rapid LPS release is attributed to the amphiphilicity of this molecule.[1] The diffusivity of CLA in PGS-CinA matrices is concentration-dependent (Table 4.1). PGS-CinA matrices with nominal loading of 100 mg/ml CLA exhibit maximum loadings at 1,437 ± 17 μg where M_t/M_∞= 0.5 at t = 16 hr. The parameters M_t and M_∞ refer to the instantaneous amounts of CLA released at time t and the total amount of CLA loaded in the PGS-CinA matrix, respectively. CLA-loaded PGS-CinA matrices with nominal loading of 100 mg/ml were further investigated in vivo. The diffusivity of CLA in PGS-CinA was determined by fitting the CLA release profile to analytical models derived from Fick's second law of diffusion in cylindrical coordinates under the perfect sink conditions and $\frac{dc(r,t)}{dz} = \frac{dc(r,t)}{d\theta} = 0$ for all t where $c(r,t)$ is the instantaneous CLA concentration in the matrix.[47] This expression can be approximated by the following analytical expressions for the regimes of both $\frac{M_t}{M_\infty} < 0.4$ and $\frac{M_t}{M_\infty} > 0.4$, respectively.[47]

$$\frac{M_t}{M_\infty} = 4\sqrt{\frac{Dt}{\pi r^2}} - \frac{Dt}{r^2} \qquad \text{Eqn. 4.3}$$

$$\frac{M_t}{M_\infty} = 1 - 0.62 \times exp\left(\frac{-5.78Dt}{r^2}\right) \qquad \text{Eqn. 4.4}$$

D is the diffusivity of the solute in the matrix; *r* is the radius of the cylinder. A diffusion coefficient of 3.94 x 10^{-9} cm^2/s, 95% CI [3.12 x 10^{-9}, 4.61 x 10^{-9}] cm^2/s was extracted from release curves (Figure 4.3d). The mechanism of controlled release of CLA in PGS-CinA can be explained using Korsmeyer-Peppas model (Figure 4.3c).[27] The exponent *n* in Korsmeyer-Peppas' equation is 0.61 ± 0.05 (r^2=0.94), 0.76 ± 0.04 (r^2=0.97), and 0.59 ± 0.03 (r^2=0.98), for 100, 10, and 1 μg/ml loading, respectively. Values of 0.45 < *n* < 0.89 for cylindrical matrices suggest that the diffusion mechanism is anomalous non-Fickian transport that combines contributions from both diffusion in the hydrated matrix and relaxation of the polymer matrix.[61]

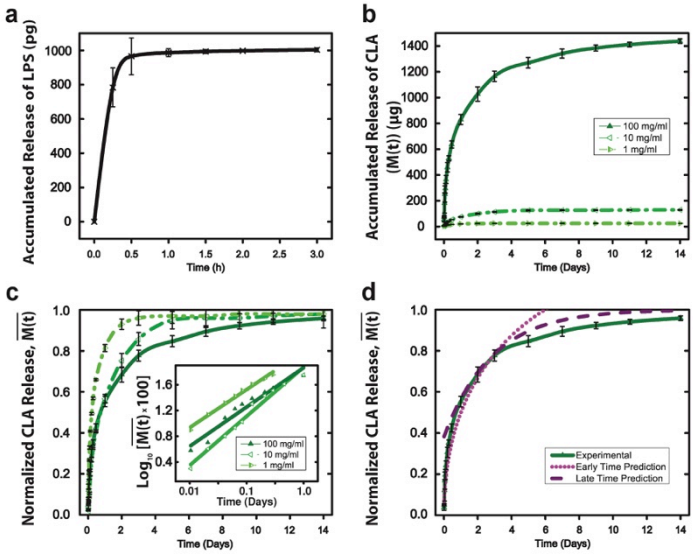

Figure 4.3 In vitro release profiles of LPS and CLA from PGS-CinA matrices. (a) More than 95% of total released LPS is released from matrices within 1 h. (b) CLA with different nominal loading concentrations is released from matrices within 2-7 d. (c) Analysis of CLA release is illustrated in a relative released CLA plot and a Korsmeyer-Peppas plot. (d) The release profile of CLA from PGS-CinA matrices with nominal loading of 100 mg/ml is fit to early and late time predictions. CLA diffusivity in hydrated

PGS-CinA networks is calculated to be D_{eff} = 3.94 x 10^{-9} cm^2/s, 95% CI [3.12 x 10^{-9}, 4.61 x 10^{-9}] cm^2/s. Data points and errors represent the mean and SD, respectively (n=4).

Table 4.1 Loading Concentrations and Release Kinetics

Nominal Loading (mg/ml)	Theoretical Loading (μg)	Actual Maximum Released* (μg)	Diffusivity (cm^2/s)
1	2.65 x 10^1	24.5	1.63 x 10^{-8}
10	2.65 x 10^2	174.6	4.87 x 10^{-9}
100	2.65 x 10^3	1437	3.94 x 10^{-9}

* The actual maximum released CLA is obtained from the release plateau.[14,17,21]

The extracted value of the diffusion coefficient (3.94 x 10^{-9} cm^2/s, 95% CI [3.12 x 10^{-9}, 4.61 x 10^{-9}] cm^2/s) is consistent with D_{eff}, calculated to be 4.12 x 10^{-9} ± 2.06 x 10^{-9} cm^2/s based on a theoretical model developed by Lustig and Peppas that relates solute diffusivity and the physical parameters of crosslinked networks.[31]

$$D_{eff} = D_{sol}\left(1 - \frac{R_h}{\xi}\right)e^{-\frac{1}{Q-1}}, \qquad \text{Eqn. 4.5}$$

The parameters D_{eff} and D_{sol} refer to the effective and solute diffusion coefficients, respectively, R_h is the hydrodynamic radius, and Q is the swelling ratio. Values of D_{sol} and R_h for CLA are adopted from values measured in fatty acids with 18-carbon chains.[22] PGS-CinA networks contain unknown portions of micropores that contribute to different dimensional and gravimetric swelling, so both dimensional (Q_{dim}) and gravimetric (Q_{grav}) swelling ratios are measured to determine D_{eff}.[48,57,58] The measured value of dimensional swelling is Q_{dim} = 1.13 ± 0.01 (See Supporting Information) while the measured value for gravimetric swelling is Q_{grav} = 1.08 ± 0.02. These two swelling

ratios predict different values for D_{eff} based on inserting Eqn. 4.1 into Eqn. 4.5 (Figure 4.4a). Experimentally determined values for D_{eff} are in close agreement with swelling ratios extracted from dimensional measurements Q_{dim}. Experimental values for D_{eff} and Q_{dim} extracted from Eqn. 4.5 also generate a value for mesh size $\xi_{PGS\text{-}CinA}$ that is internally consistent with that calculated using the Canal and Peppas model (Eqn. 4.1) (Figure 4.4b). These data suggest that CLA diffusion through PGS-CinA networks is governed by the mesoscale structure of the crosslinks.

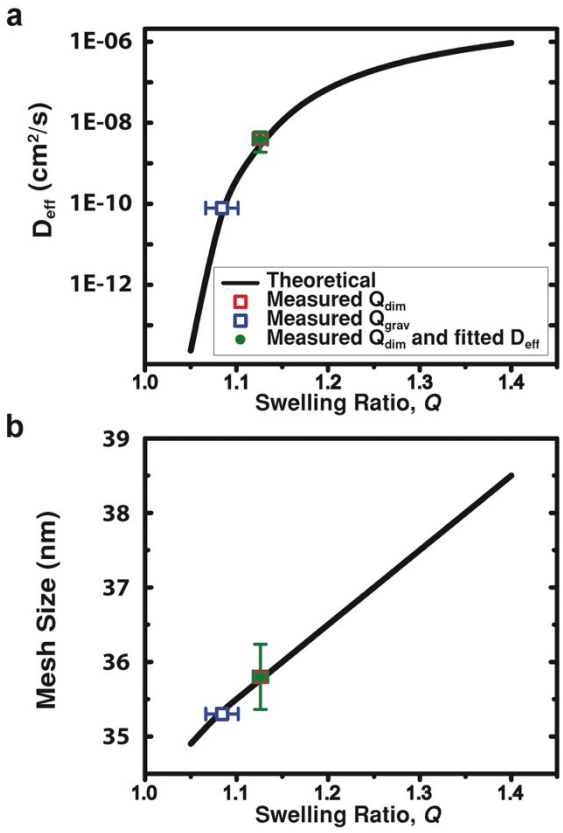

Figure 4.4 (a) Plot of effective diffusion coefficient (D_{eff}) and (b) mesh size (ξ) versus swelling ratio (Q). Continuous lines indicate predicted values of D_{eff} and ξ as a function of a hypothetical Q (Eqn. 4.5). Experimentally determined values of Q_{dim} and Q_{eff} generate two corresponding values for D_{eff} and ξ. The value of Q_{dim} produces a value

of D_{eff} that is consistent with analytical models derived from Fick's second law (Eqn. 4.3 and Eqn. 4.4.).

4.4.d Histological Analysis of Mouse Skin Inserted with Elastomeric Matrices

Drug-eluting PGS-CinA matrices bias local macrophage populations to an M2 phenotype (CD163+) depending on the small molecule that is delivered (Figure 4.5). M2 macrophage densities at *t* = 3, 7, 10, and 14 d exhibit significant statistical interaction between the treatments (LPS, CLA, or LPS+CLA) and time (two-way ANOVA, F=4.627, $p < 0.001$). Both blank and CLA-eluting PGS-CinA matrices produce comparable trends in M2 macrophage density at 3 d. These observations are attributed to the fact that the effect of CLA may be dwarfed by the pro-inflammatory signals at the implantation site during early stages of wound healing.[9,26,37] The results are consistent with previous studies that found local injections of M2 macrophages at 3 d does not shorten wound closure time even though M2 macrophages are associated with regenerative healing.[24] CLA-eluting matrices, however, significantly increase the local M2 macrophage density ($5.0 \times 10^3 \pm 1.4 \times 10^3$ cells/cm^2) compared to blank PGS-CinA matrices ($3.8 \times 10^3 \pm 2.2 \times 10^3$ cells/cm^2) at 7 d (Kruskal-Wallis, *** $p < 0.001$). Transient increases in M2 macrophage population for CLA-eluting matrices at 7 d are consistent with the characteristic time scale for CLA release. These results corroborate previous findings that suggest CLA is a bioactive small molecule that polarizes M2 macrophages in vivo.[35,40]

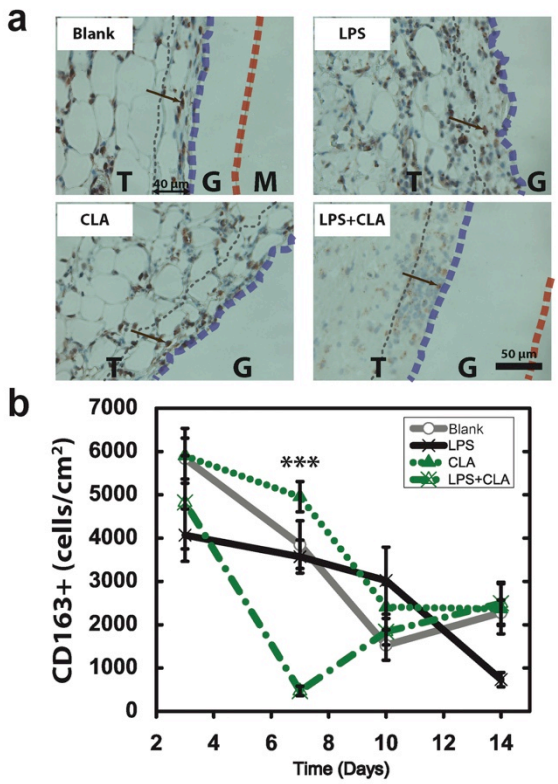

Figure 4.5 CD163+ cells at the interface of mouse dermal tissues and implanted PGS-CinA matrices. (a) Representative histological micrographs at 7 d post-implantation. The density of CD163+ cells (stained in brown indicated by arrow) was determined within 40 μm from the interface (thick dark blue to thin grey dotted lines). T, G, and M stand for tissue, gap, and matrix, respectively. The red dotted line indicates an edge of a cylindrical matrix. (b) Quantified CD163+ cell density collected at designated times after surgery. An asterisk indicates significant difference of the cell density using CLA, compared to all other treatments at 7 d (Kruskal Wallis, *** $p < 0.001$, n=4). Two-way ANOVA with Bonferroni also shows that CLA treatments are statistically distinct from LPS and LPS+CLA (* $p < 0.05$, n=4).

Drug-eluting PGS-CinA matrices loaded with different bioactive small molecules exhibit significant differences in dermal downgrowth as shown in Figure 4.6 (two-way ANOVA, F=6.024, *** $p < 0.001$). CLA-eluting matrices and the blank PGS-CinA matrices reduce epidermal downgrowth at 14 d compared to PGS-CinA devices loaded with LPS (Bonferroni correction, * $p < 0.05$). The epidermal downgrowth of CLA-eluting matrices and the blank matrices at 14 d are 60.4 ± 32.4 μm and 171.7 ± 93.8 μm, respectively. CLA-eluting PGS-CinA matrices therefore reduce epidermal downgrowth for time lines beyond the presumed local presence of CLA. These data temporally correlate M2 macrophage density with reduced epidermal downgrowth. The supply of CLA is exhausted after 3 d (>70% released), yet the M2 macrophage density is increased and downgrowth is decreased at 7 d compared to other treatments. These data suggest that there is temporal coordination between CLA release kinetics, M2 macrophage density, and dermal downgrowth. Furthermore, the local M2 macrophage density is correlated with reduced downgrowth. CLA-eluting elastomeric matrices are therefore suitable as coatings for catheters that need regular weekly replacement. The 7-day time period exceeds minimum intravenous catheter replacement time (72–96 hours) that the US Centers for Disease Control and Prevention (CDC) currently recommend.[38] This approach can therefore extend the use of catheters in a prospective clinical setting. The fibrous capsule thickness surrounding percutaneous elastomeric implants were measured (two-way ANOVA, F=0.0872, $p < 0.001$) (Appendix, Figure 4.8). Fibrous capsule thickness surrounding CLA-eluting matrices and the blank matrices at 14 d were measured to be 88.99 ± 28.31 μm and 60.49 ± 7.54 μm,

respectively. The fibrous capsule is well within the nominal 200-250 μm threshold that is suggested for implanted biomaterials.[21]

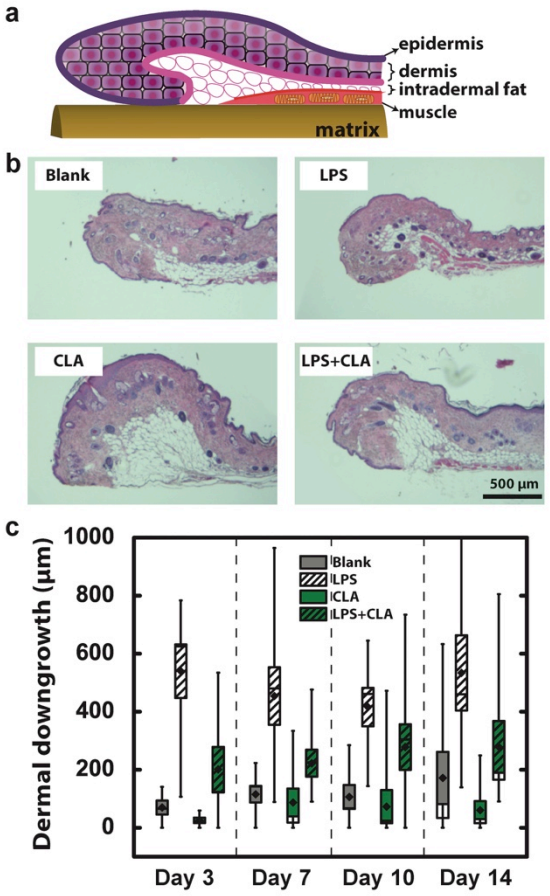

Figure 4.6 Dermal downgrowth at the insertion site. (a) Schematic of sectioned mouse skin layers with the percutaneous device at bottom. (b) Representative H&E histology image of mouse skin at the tube insertion site at 7 d post-surgery. (c) Quantified dermal downgrowth (Two-way ANOVA, *** $p < 0.001$, n=4). Boxes and whiskers show SEMs with medians and 90^{th}-10^{th} percentiles, respectively. Diamonds represent the mean.

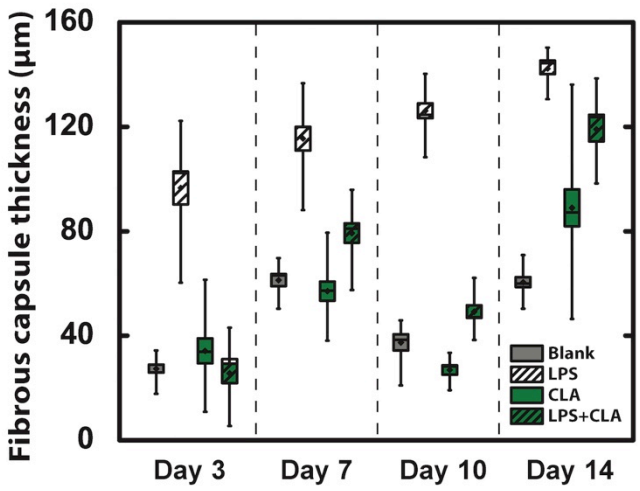

Figure 4.7 The fibrous capsule thickness at the skin-device interface (two-way ANOVA, *** $p < 0.001$). Boxes and whiskers show SEMs with medians and 90^{th}-10^{th} percentiles, respectively. Diamonds represent the means (n=4).

4.4.e Contraction of Mouse Skin over Inserted Elastomeric Matrices

Skin over the percutaneous implants or a skin bridge (Figure 4.8a) was contracted over time after a surgery. Prior work suggests that contraction correlates with dermal migration around a percutaneous device in a mouse model and should be assessed for long term implants.[18] However, in this study, dermal contraction occurs within one week for all matrices (Figure 4.8). These finding suggest that skin bridge length and dermal downgrowth are decoupled. CLA-eluting matrices best preserve the bridge length (98.9 ± 6.4 %) at 7 d, compared to other matrices (Kruskal-Wallis, $p < 0.05$). As mentioned earlier, the density of M2 macrophages around CLA-eluting PGS-CinA implants is also the highest compared to all other conditions at 7 d. We cautiously

speculate that CLA-eluting matrices increases the local density of M2 macrophages, which ultimately contributes to reduced dermal contraction.

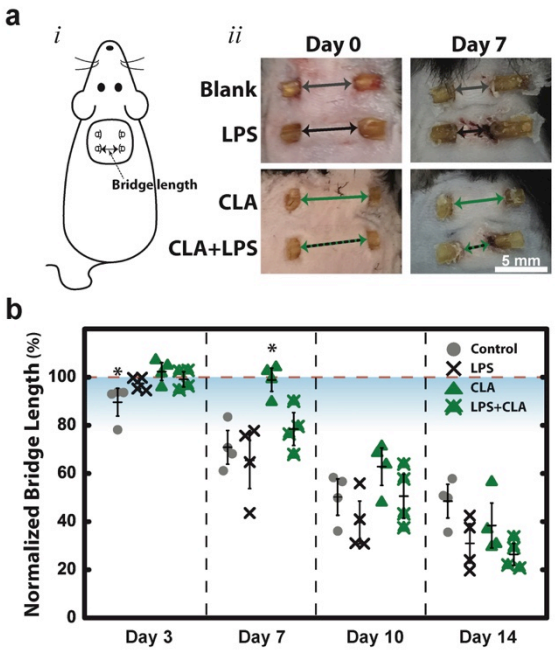

Figure 4.8 Measurement of skin bridge length. (a, *i*). Schematic showing two cylindrical PGS-CinA matrices that are implanted percutaneously through the back skin of murine animal subjects. An arrow indicates skin bridge length that measures the length between two insertion sites. (a, *ii*) Representative skin bridges of each treatment at 0 and 7 d. (b) Normalized percentage of skin bridge length. An asterisk indicates significant difference using Kruskal-Wallis (* $p < 0.05$).

4.5 Conclusions

Here, we design cylindrical percutaneous matrices to provide a controlled release of small molecules that alter macrophage expressions. Our results show that PGS-CinA

exhibits suitable properties of biomaterials for percutaneous devices: (1) a Young's modulus in the elastomeric regime that matches that of the native epidermis; (2) a crosslinked polymeric networks with a mesh size that controls the release of small molecules; and (3) an attenuated fibrous capsule response. PGS-CinA matrices achieve controlled release CLA for 7 d, which increases the local density of macrophages with M2 phenotypes in vivo. CLA-mediated macrophage polarization is concomitant with reduced dermal downgrowth and skin contraction. Taken together, CLA-eluting PGS-CinA elastomers represent a viable coating strategy to reduce epidermal downgrowth in percutaneous devices.

References:

1. Aurell, C. A., and A. O. Wistrom. Critical Aggregation Concentrations of Gram-Negative Bacterial Lipopolysaccharides (LPS). *Biochem. Biophys. Res. Commun.* 253:119–123, 1998.
2. van Baal, M. C., H. C. van Santvoort, T. L. Bollen, O. J. Bakker, M. G. Besselink, and H. G. Gooszen. Systematic review of percutaneous catheter drainage as primary treatment for necrotizing pancreatitis. *Br. J. Surg.* 98:18–27, 2011.
3. Baker, P. R. S., Y. Lin, F. J. Schopfer, S. R. Woodcock, A. L. Groeger, C. Batthyany, S. Sweeney, M. H. Long, K. E. Iles, L. M. S. Baker, B. P. Branchaud, Y. E. Chen, and B. A. Freeman. Fatty Acid Transduction of Nitric Oxide Signaling MULTIPLE NITRATED UNSATURATED FATTY ACID DERIVATIVES EXIST IN HUMAN BLOOD AND URINE AND SERVE AS ENDOGENOUS PEROXISOME PROLIFERATOR-ACTIVATED RECEPTOR LIGANDS. *J. Biol. Chem.* 280:42464–42475, 2005.
4. Bouhlel, M. A., B. Derudas, E. Rigamonti, R. Dièvart, J. Brozek, S. Haulon, C. Zawadzki, B. Jude, G. Torpier, N. Marx, B. Staels, and G. Chinetti-Gbaguidi. PPARγ Activation Primes Human Monocytes into Alternative M2 Macrophages with Anti-inflammatory Properties. *Cell Metab.* 6:137–143, 2007.
5. Brown, B. N., R. Londono, S. Tottey, L. Zhang, K. A. Kukla, M. T. Wolf, K. A. Daly, J. E. Reing, and S. F. Badylak. Macrophage Phenotype as a Predictor of Constructive Remodeling following the Implantation of Biologically Derived Surgical Mesh Materials. *Acta Biomater.* 8:978–987, 2012.
6. Brown, B. N., B. D. Ratner, S. B. Goodman, S. Amar, and S. F. Badylak. Macrophage polarization: An opportunity for improved outcomes in biomaterials and regenerative medicine. *Biomaterials* 33:3792–3802, 2012.
7. Brown, B. N., B. M. Sicari, and S. F. Badylak. Rethinking Regenerative Medicine: A Macrophage-Centered Approach. *Front. Immunol.* 5:, 2014.
8. Canal, T., and N. A. Peppas. Correlation between mesh size and equilibrium degree of swelling of polymeric networks. *J. Biomed. Mater. Res.* 23:1183–1193, 1989.
9. Casey, M. E., and S. S. Jedlicka. Neuronal Outgrowth and Differentiation on Poly(glycerol sebacate). , 2012.
10. Cervera, M., M. Dolz, J. V. Herraez, and R. Belda. Evaluation of the elastic behaviour of central venous PVC, polyurethane and silicone catheters. *Phys. Med. Biol.* 34:177–183, 1989.

11. Chehroudi, B., and D. M. Brunette. Subcutaneous microfabricated surfaces inhibit epithelial recession and promote long-term survival of percutaneous implants. *Biomaterials* 23:229–237, 2002.
12. Cipolla, D., H. Wu, S. Eastman, T. Redelmeier, I. Gonda, and H.-K. Chan. Development and Characterization of an In Vitro Release Assay for Liposomal Ciprofloxacin for Inhalation. *J. Pharm. Sci.* 103:314–327, 2014.
13. Deng, B., M. Wehling-Henricks, S. A. Villalta, Y. Wang, and J. G. Tidball. IL-10 triggers changes in macrophage phenotype that promote muscle growth and regeneration. *J. Immunol. Baltim. Md 1950* 189:3669–3680, 2012.
14. Edgeworth, J. D., D. F. Treacher, and S. J. Eykyn. A 25-year study of nosocomial bacteremia in an adult intensive care unit. *Crit. Care Med.* 27:1421–1428, 1999.
15. Eichie, F., and R. Okor. Parameters to be Considered in the Simulation of Drug Release from Aspirin Crystals and their Microcapsules. *Trop. J. Pharm. Res.* 1:99–110, 2002.
16. Fetters, L. J., D. J. Lohse, and R. H. Colby. Chain Dimensions and Entanglement Spacings. In: Physical Properties of Polymers Handbook, edited by J. E. Mark. Springer New York, 2007, pp. 447–454.at <http://link.springer.com/chapter/10.1007/978-0-387-69002-5_25>
17. Fleckman, P., and J. E. Olerud. Models for the histologic study of the skin interface with percutaneous biomaterials. *Biomed. Mater.* 3:34006, 2008.
18. Fleckman, P., M. Usui, G. Zhao, R. Underwood, M. Maginness, A. Marshall, C. Glaister, B. Ratner, and J. Olerud. Cutaneous and inflammatory response to long-term percutaneous implants of sphere-templated porous/solid poly(HEMA) and silicone in mice. *J. Biomed. Mater. Res. A* 100A:1256–1268, 2012.
19. Fuchs, K., P. E. Bize, A. Denys, G. Borchard, and O. Jordan. Sunitinib-eluting beads for chemoembolization: Methods for in vitro evaluation of drug release. *Int. J. Pharm.* 482:68–74, 2015.
20. Hendriks, F. M., D. Brokken, J. T. W. M. Van Eemeren, C. W. J. Oomens, F. P. T. Baaijens, and J. B. a. M. Horsten. A numerical-experimental method to characterize the non-linear mechanical behaviour of human skin. *Skin Res. Technol.* 9:274–283, 2003.
21. Imai, Y., and E. Masuhara. Long-term in vivo studies of poly(2-hydroxyethyl methacrylate). *J. Biomed. Mater. Res.* 16:609–617, 1982.
22. Iwahashi, M., Y. Kasahara, H. Minami, H. Matsuzawa, M. Suzuki, and Y. Ozaki. Molecular Behaviors of n-Fatty Acids in Liquid State. *J. Oleo Sci.* 51:157–164, 2002.
23. Iwahashi, M., Y. Yamaguchi, Y. Ogura, and M. Suzuki. Dynamical Structures of Normal Alkanes, Alcohols, and Fatty Acids in the Liquid State as Determined by Viscosity, Self-Diffusion Coefficient, Infrared Spectra, and ¹³CNMR Spin-Lattice Relaxation Time Measurements. *Bull. Chem. Soc. Jpn.* 63:2154–2158, 1990.
24. Jetten, N., N. Roumans, M. J. Gijbels, A. Romano, M. J. Post, M. P. J. de Winther, R. R. W. J. van der Hulst, and S. Xanthoulea. Wound Administration of M2-Polarized Macrophages Does Not Improve Murine Cutaneous Healing Responses. *PLoS ONE* 9:, 2014.
25. Keepers, T. R., L. K. Gross, and T. G. Obrig. Monocyte Chemoattractant Protein 1, Macrophage Inflammatory Protein 1α, and RANTES Recruit Macrophages to the Kidney in a Mouse Model of Hemolytic-Uremic Syndrome. *Infect. Immun.* 75:1229–1236, 2007.
26. Khanna, S., S. Biswas, Y. Shang, E. Collard, A. Azad, C. Kauh, V. Bhasker, G. M. Gordillo, C. K. Sen, and S. Roy. Macrophage Dysfunction Impairs Resolution of Inflammation in the Wounds of Diabetic Mice. *PLoS ONE* 5:, 2010.
27. Korsmeyer, R. W., R. Gurny, E. Doelker, P. Buri, and N. A. Peppas. Mechanisms of solute release from porous hydrophilic polymers. *Int. J. Pharm.* 15:25–35, 1983.
28. Li, Y., G. A. Thouas, and Q.-Z. Chen. Biodegradable soft elastomers: synthesis/properties of materials and fabrication of scaffolds. *RSC Adv.* 2:8229–8242, 2012.
29. Liang, X., and S. A. Boppart. Biomechanical Properties of In Vivo Human Skin From Dynamic Optical Coherence Elastography. *IEEE Trans. Biomed. Eng.* 57:953–959, 2010.
30. Liu, Q., L. Jiang, R. Shi, and L. Zhang. Synthesis, preparation, in vitro degradation, and application of novel degradable bioelastomers—A review. *Prog. Polym. Sci.* 37:715–765, 2012.
31. Lustig, S. R., and N. A. Peppas. Solute diffusion in swollen membranes. IX. Scaling laws for solute diffusion in gels. *J. Appl. Polym. Sci.* 36:735–747, 1988.
32. Maki, D. G., D. M. Kluger, and C. J. Crnich. The Risk of Bloodstream Infection in Adults With Different Intravascular Devices: A Systematic Review of 200 Published Prospective Studies. *Mayo Clin. Proc.* 81:1159–1171, 2006.

33. Makita, N., Y. Hizukuri, K. Yamashiro, M. Murakawa, and Y. Hayashi. IL-10 enhances the phenotype of M2 macrophages induced by IL-4 and confers the ability to increase eosinophil migration. *Int. Immunol.* 27:131–141, 2015.
34. Mantovani, A., A. Sica, S. Sozzani, P. Allavena, A. Vecchi, and M. Locati. The chemokine system in diverse forms of macrophage activation and polarization. *Trends Immunol.* 25:677–686, 2004.
35. McCarthy, C., M. M. Duffy, D. Mooney, W. G. James, M. D. Griffin, D. J. Fitzgerald, and O. Belton. IL-10 mediates the immunoregulatory response in conjugated linoleic acid-induced regression of atherosclerosis. *FASEB J.* 27:499–510, 2013.
36. Nam, K., R. Matsushima, T. Kimura, T. Fujisato, and A. Kishida. In Vivo Characterization of a Decellularized Dermis-Polymer Complex for Use in Percutaneous Devices. *Artif. Organs* 38:1060–1065, 2014.
37. Novak, M. L., E. M. Weinheimer-Haus, and T. J. Koh. Macrophage Activation and Skeletal Muscle Healing Following Traumatic Injury. *J. Pathol.* 232:344–355, 2014.
38. O'Grady, N. P., M. Alexander, L. A. Burns, E. P. Dellinger, J. Garland, S. O. Heard, P. A. Lipsett, H. Masur, L. A. Mermel, M. L. Pearson, I. I. Raad, A. G. Randolph, M. E. Rupp, and S. Saint. Guidelines for the prevention of intravascular catheter-related infections. *Am. J. Infect. Control* 39:S1–S34, 2011.
39. Pholpabu, P., S. S. Yerneni, C. Zhu, P. G. Campbell, and C. J. Bettinger. Controlled Release of Small Molecules from Elastomers for Reducing Epidermal Downgrowth in Percutaneous Devices. *ACS Biomater. Sci. Eng.* , 2016.doi:10.1021/acsbiomaterials.6b00192
40. Pini, M., S. Touch, H. Poirier, E. Dalmas, I. Niot, C. Rouault, C. Druart, N. Delzenne, K. Clément, S. André, and M. Guerre-Millo. Adipose tissue adaptive response to trans-10,cis-12-conjugated linoleic acid engages alternatively activated M2 macrophages. *FASEB J. Off. Publ. Fed. Am. Soc. Exp. Biol.* 30:241–251, 2016.
41. Pittiruti, M., H. Hamilton, R. Biffi, J. MacFie, M. Pertkiewicz, and ESPEN. ESPEN Guidelines on Parenteral Nutrition: central venous catheters (access, care, diagnosis and therapy of complications). *Clin. Nutr. Edinb. Scotl.* 28:365–377, 2009.
42. von Recum, A. F. Applications and failure modes of percutaneous devices: A review. *J. Biomed. Mater. Res.* 18:323–336, 1984.
43. Rodrigues, H. G., M. A. R. Vinolo, J. Magdalon, K. Vitzel, R. T. Nachbar, A. F. M. Pessoa, M. F. dos Santos, E. Hatanaka, P. C. Calder, and R. Curi. Oral Administration of Oleic or Linoleic Acid Accelerates the Inflammatory Phase of Wound Healing. *J. Invest. Dermatol.* 132:208–215, 2012.
44. Schopfer, F. J., Y. Lin, P. R. S. Baker, T. Cui, M. Garcia-Barrio, J. Zhang, K. Chen, Y. E. Chen, and B. A. Freeman. Nitrolinoleic acid: An endogenous peroxisome proliferator-activated receptor γ ligand. *Proc. Natl. Acad. Sci. U. S. A.* 102:2340–2345, 2005.
45. Seidi, A., M. Ramalingam, I. Elloumi-Hannachi, S. Ostrovidov, and A. Khademhosseini. Gradient biomaterials for soft-to-hard interface tissue engineering. *Acta Biomater.* 7:1441–1451, 2011.
46. Sica, A., and A. Mantovani. Macrophage plasticity and polarization: in vivo veritas. *J. Clin. Invest.* 122:787–795, 2012.
47. Siepmann, J., R. A. Siegel, and F. Siepmann. Diffusion Controlled Drug Delivery Systems. In: Fundamentals and Applications of Controlled Release Drug Delivery, edited by J. Siepmann, R. A. Siegel, and M. J. Rathbone. Springer US, 2012, pp. 127–152.at <http://link.springer.com/chapter/10.1007/978-1-4614-0881-9_6>
48. Stringer, J. L., and N. A. Peppas. Diffusion of small molecular weight drugs in radiation-crosslinked poly(ethylene oxide) hydrogels. *J. Controlled Release* 42:195–202, 1996.
49. Sun, Z.-J., C. Chen, M.-Z. Sun, C.-H. Ai, X.-L. Lu, Y.-F. Zheng, B.-F. Yang, and D.-L. Dong. The application of poly (glycerol–sebacate) as biodegradable drug carrier. *Biomaterials* 30:5209–5214, 2009.
50. Viswanathan, P., M. Guvendiren, W. Chua, S. B. Telerman, K. Liakath-Ali, J. A. Burdick, and F. M. Watt. Mimicking the topography of the epidermal–dermal interface with elastomer substrates. *Integr. Biol.* 8:21–29, 2016.
51. Walboomers, X. F., and J. A. Jansen. Effect of microtextured surfaces on the performance of percutaneous devices. *J. Biomed. Mater. Res. A* 74A:381–387, 2005.
52. Wang, Y., G. A. Ameer, B. J. Sheppard, and R. Langer. A tough biodegradable elastomer. *Nat. Biotechnol.* 20:602–606, 2002.
53. Webb, A. R., J. Yang, and G. A. Ameer. Biodegradable polyester elastomers in tissue engineering. *Expert Opin. Biol. Ther.* 4:801–812, 2004.

54. Wenzel, R. P., and M. B. Edmond. The impact of hospital-acquired bloodstream infections. *Emerg. Infect. Dis.* 7:174–177, 2001.
55. Yoda, R. Elastomers for biomedical applications. *J. Biomater. Sci. Polym. Ed.* 9:561–626, 1998.
56. Yu, Y., P. H. Correll, and J. P. Vanden Heuvel. Conjugated linoleic acid decreases production of pro-inflammatory products in macrophages: evidence for a PPARγ-dependent mechanism. *Biochim. Biophys. Acta BBA - Mol. Cell Biol. Lipids* 1581:89–99, 2002.
57. Zhang, X.-Z., D.-Q. Wu, and C.-C. Chu. Synthesis, characterization and controlled drug release of thermosensitive IPN–PNIPAAm hydrogels. *Biomaterials* 25:3793–3805, 2004.
58. Zhu, C., S. R. Kustra, and C. J. Bettinger. Photocrosslinkable biodegradable elastomers based on cinnamate-functionalized polyesters. *Acta Biomater.* 9:7362–7370, 2013.
59. Handbook of Pharmaceutical Controlled Release Technology. New York: CRC Press, 2000, 902 pp.

CHAPTER 5 NON-FOULING ZWITTERIONIC HYDROGEL FOR PERCUTANEOUS DEVICES

The content in this chapter in whole or in part will be included in a manuscript for submission to *Interface Focus*.

5.1 Abstract

Indwelling catheters are major cause of nosocomial bloodstream infection, which leads to morbidity and potentially mortality. The main strategies are to reduce bacterial adhesion on device surface and epidermal regression. In this study, zwitterionic polycarboxybetaine (PCBMA) hydrogel is percutaneously implanted in mice to investigate host-device responses. PCBMA cylindrical hydrogels with different percentage of crosslinkers are simply prepared within 2 h at room temperature, yielding different mechanical properties of hydrogels. Histological analysis includes dermal downgrowth, density of macrophages, and thickness of fibrous capsule, comparing between PCBMA and polyhydroxyethylmethacrylate (PHEMA). Skin contraction over implants is also measured daily over 20 d of implantation.

5.2 Introduction

Catheters are one of the most necessary devices in modern healthcare. However, they commonly cause nosocomial catheter-related bloodstream infection that is costly and potentially lethal.[14,15] Attempts to reduce the infection usually either focus

on the reduction of biofilm formation or epidermal downgrowth since high bacterial loads and dermal downgrowth increase the risk of bloodstream infection.[9,14–16,20] Anti-bacterial coatings are typically achieved by grafting or incorporating antibiotics to the catheter surface.[10,13,20] The coating is very effective in reducing the bacterial adhesion and biofilm formation.[18,20] However, it tends to cause development of drug resistance.[2] The epidermal downgrowth that percutaneous devices induce along the skin-device interface can be attenuated using topographical cues that generate stable biointegration.[21] However, replacing the skin-integrating catheter will require a surgery.

Recently, zwitterionic materials have raised a great interest as an important biomaterial class that provides robust ultra-low-fouling property.[6–8,22] Polycarboxybetaine (PCBMA) adsorb <0.3 ng/cm^2 proteins from 100% human blood plasma or plasma.[11] The resistance of protein adsorption overcomes the non-fouling property of other currently used biomaterials, such as polyethyleneglycol (PEG) and polyhydroxyethylmethacrylate (PHEMA), leading to less cell adhesion and fibrous formation in both in vitro and in vivo studies.[4,5,22] PCBMA is an ideal material candidate for percutaneous devices because it provides both skin biocompatibility and resistance of bacterial adhesion.[6,22] Here, we investigate host responses to percutaneous device made from PCBMA hydrogel that is fabricated from simple radical polymerization. The hydrogel characterization and skin histological analysis will provide insight knowledge for a better design of percutaneous devices.

5.3 Materials and Methods

Materials and methods of this chapter are described in Chapter 2.

5.4 Results and Discussion

5.4.a Mechanical and Physical Properties of Hydrogels

PCBMA hydrogels with different initial concentrations of crosslinkers have mechanical properties, as shown in Figure 5.1. Since we would like to compare host responses using PHEMA and PCBMA by controlling the modulus, 15%X and 30%X PCBMA were selected to match the modulus of 3M and 5M PHEMA, respectively, for use in in vivo experiments. The compressive moduli of the selected hydrogels are $E_{3M\text{-}PHEMA}$ = 404 ± 61 Pa, $E_{5M\text{-}PHEMA}$ = 2,991 ± 474 Pa, $E_{15\%X\text{-}PCBMA}$ = 475 ± 105 Pa, and $E_{30\%X\text{-}PCBMA}$ = 3,355 ± 673 Pa. The differences between the means of 3M PHEMA and 15%X PCBMA, and 5M PHEMA and 30% PCBMA are not statistically significant (p > 0.05). The mechanical properties of PCBMA hydrogels were also further investigated using rheological measurements, as shown in Figure 5.2. At 0.5% strain, the storage moduli of PCBMA at both 15%X and 30%X are stable for all applied frequencies. The higher of storage modulus of 30% PCBMA, compared with 15%X PCBMA, in the rheological measurement agrees with the compressive modulus.

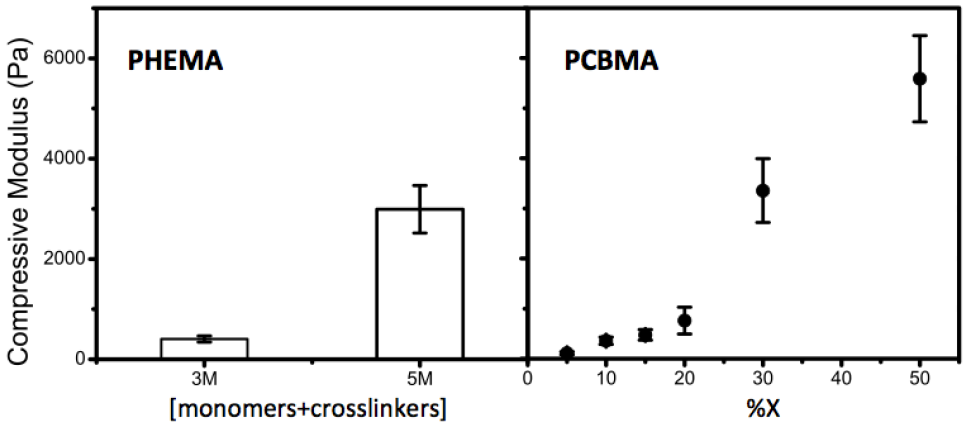

Figure 5.1 Compressive modulus of PHEMA and PCBMA hydrogels. Bars and points represent means. Error bars represent standard deviation. (n=8)

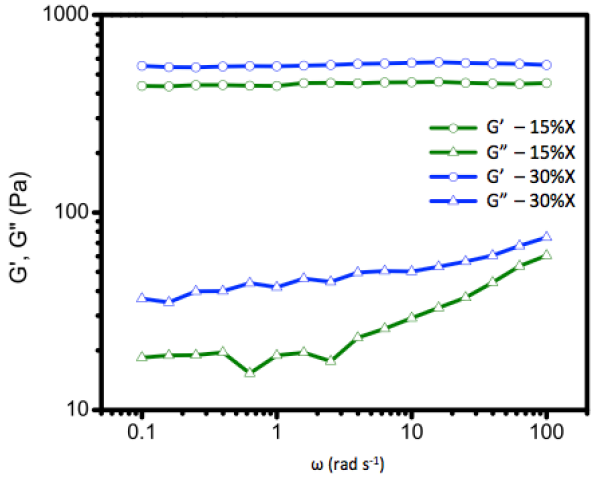

Figure 5.2 Representative storage and loss moduli of PCBMA hydrogels. The strain was fixed at 0.5% for all measurements.

The swelling ratios of PHEMA and PCBMA were reported here since it is an important property that is attributed to the degree of cross-linking and hydrophilicity of the hydrogel.[3,12,17] The swelling ratio of the hydrogels are $Q_{3M\text{-}PHEMA}$ = 2.66 ± 0.04, $Q_{5M\text{-}PHEMA}$ = 1.60 ± 0.05, $Q_{15\%X\text{-}PCBMA}$ = 4.62 ± 0.36, and $Q_{30\%X\text{-}PCBMA}$ = 3.30 ± 0.11. Both

PCBMA hydrogels have higher average welling ratios than PHEMA. This might suggest looser crosslinking networks of the PCBMA.

5.4.b Histological Analysis of Mouse Skin

PCBMA obviously induce less epidermal downgrowth, compared to PHEMA. Micrographs in Figure 5.3 represent dermal tissues that were collected from mice implanted with different hydrogels at 15 d. The downgrowth generated around PCBMA is even less than the one induced by CLA-eluting PGS-CinA matrices at 10 d.[19] However, the histology analysis is still under an ongoing process. Further quantification and statistical analysis of downgrowth and related-cell density will be performed to confirm the results.

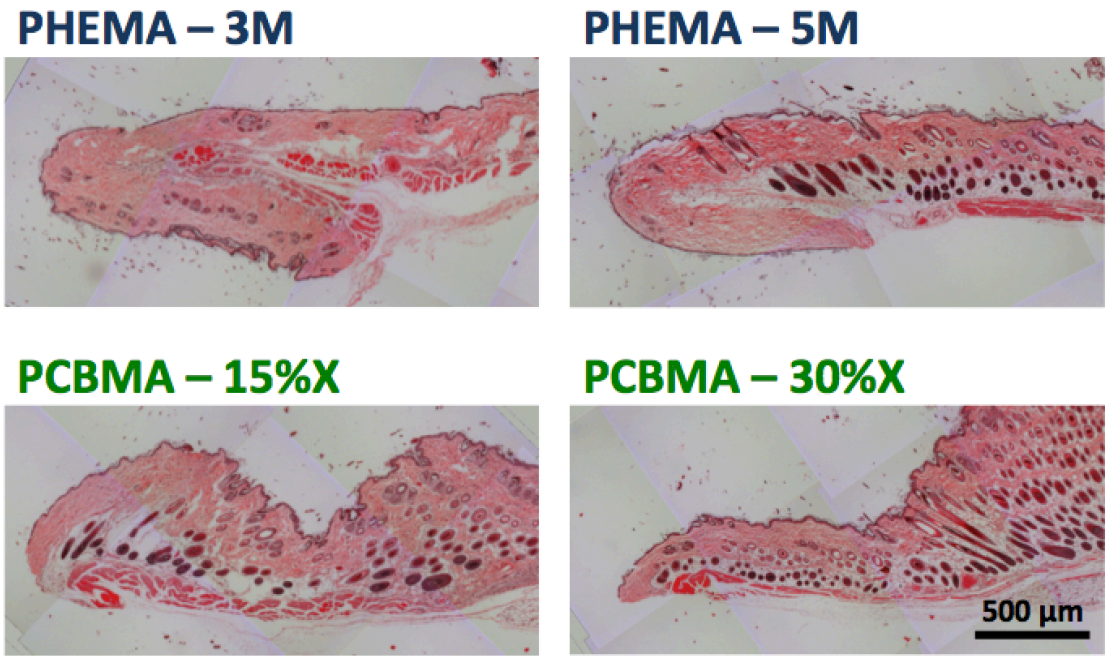

Figure 5.3 Representative H&E stained micrographs of mouse tissues at skin-device interface. All tissues were collected from implanted mice at 15 d.

The formation of fibrous capsule around all implanted hydrogels is very minimal at 20 d, as shown in Figure 5.4. Although the fibrous capsule did not occur for our experiments, PHEMA was previously reported to induce dense collagen 3 months after a subcutaneous implantation, while normal collagen density was found around PCBMA.[23] Longer percutaneous implantation might provide more information in the difference of fibrous capsule formation in PHEMA and PCBMA.

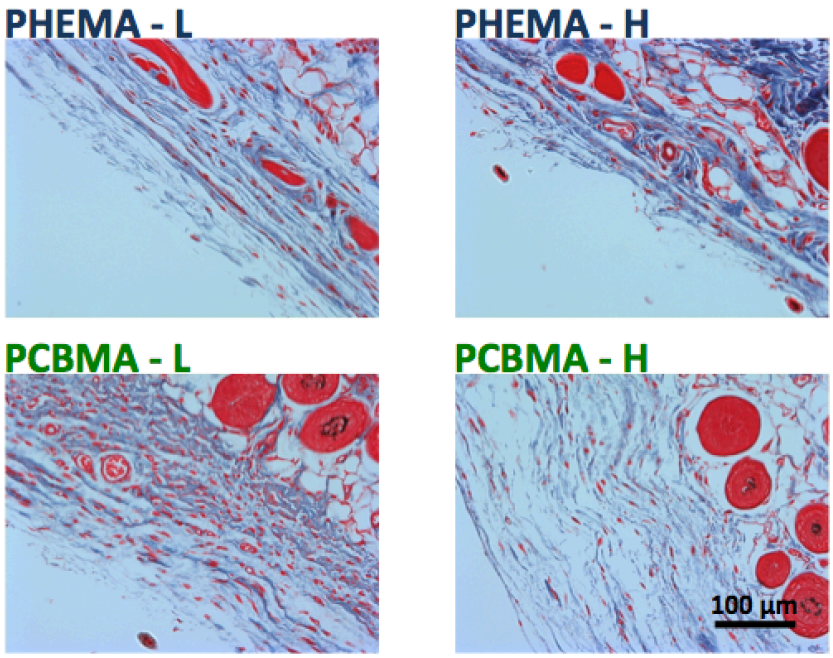

Figure 5.4 Representative Masson's trichrome stained micrographs of mouse tissues at skin-device interface. All tissues were collected at 20 d.

5.4.c Macroscopic Skin Contraction

The skin bridge contraction was observed and measured daily over 20 d after a surgery. Repeated measures ANOVA was used to analyze the bridge length data. The statistical analysis has to be performed for 4 different durations to have the same sample size each period (1-5 d, n=16; 6-10 d, n=12; 11-15 d, n=8; 16-20 d, n=4). From

1-15 d, both the types of hydrogels and time significantly influence the variance (p < 0.05), while only the types of hydrogels contribute to difference of the variance during 16-20 d (p < 0.05). Pairwise post-hoc tests confirm significant difference between the skin bridges with 3M and 5M PHEMA hydrogels on 6-15 d. The result suggests that the mechanical properties of PHEMA hydrogels are significant in skin bridge contraction, while the mechanical properties of PCBMA are not. During 6-10 d, the skin bridge with 5M PHEMA was significantly different to all other gels (p < 0.01), suggesting the least skin bridge contraction. Even though some differences among the reported skin bridges using different the types of hydrogels could be seen in Figure 5.6, the sample size was too small to confirm the difference in the statistic analysis.[1] In this study, the sample size was not increased since most of insight skin-device interactions should come from the histological analysis that has been being performed.

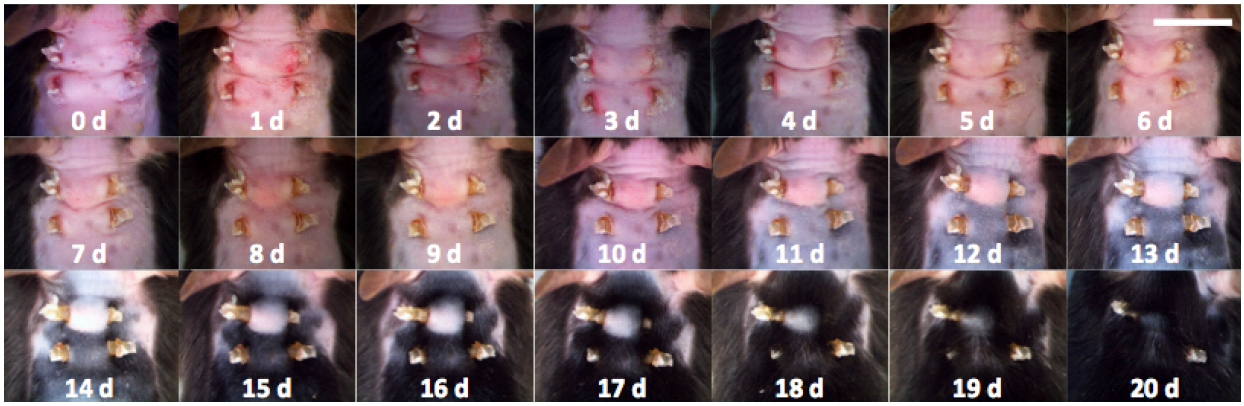

Figure 5.5 Representative images of mouse skin implanted with PCBMA at 15%X (top) and 30%X (bottom) over 20 d. Scale bar = 1 cm.

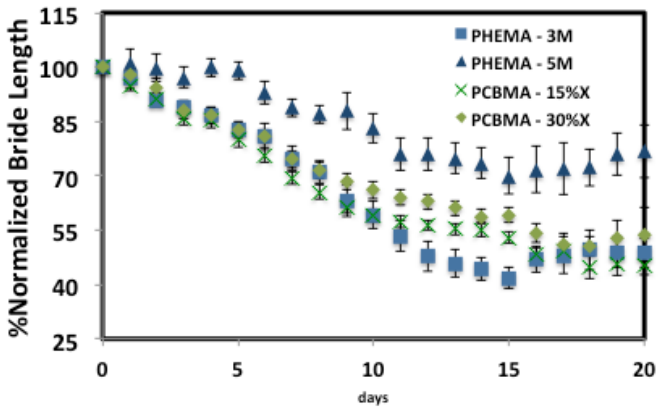

Figure 5.6 Normalized skin bridge length. The skin bridge length was recorded daily over 20 d after a surgery. Points and error bars represent means and standard errors, respectively.

5.5 Conclusions

In this study, we investigate host responses to percutaneous devices fabricated from zwitterionic materials. Our preliminary results show that the crosslinker concentration affect the mechanical properties of PCBMA, and the hydrogels prepared with at least 15% mol crosslinkers can be percutaneously implanted over 20 d. In contrast to PHEMA, the mechanical properties of PCBMA did not significantly influence the skin bridge contraction. Histological analysis should be further performed for more in-depth results and discussion.

References:

1. Bakeman, R. Recommended effect size statistics for repeated measures designs. *Behav. Res. Methods* 37:379–384.
2. Campoccia, D., L. Montanaro, and C. R. Arciola. A review of the biomaterials technologies for infection-resistant surfaces. *Biomaterials* 34:8533–8554, 2013.

3. Canal, T., and N. A. Peppas. Correlation between mesh size and equilibrium degree of swelling of polymeric networks. *J. Biomed. Mater. Res.* 23:1183–1193, 1989.
4. Carr, L. R., H. Xue, and S. Jiang. Functionalizable and nonfouling zwitterionic carboxybetaine hydrogels with a carboxybetaine dimethacrylate crosslinker. *Biomaterials* 32:961–968, 2011.
5. Carr, L. R., Y. Zhou, J. E. Krause, H. Xue, and S. Jiang. Uniform zwitterionic polymer hydrogels with a nonfouling and functionalizable crosslinker using photopolymerization. *Biomaterials* 32:6893–6899, 2011.
6. Cheng, G., G. Li, H. Xue, S. Chen, J. D. Bryers, and S. Jiang. Zwitterionic carboxybetaine polymer surfaces and their resistance to long-term biofilm formation. *Biomaterials* 30:5234–5240, 2009.
7. Chou, Y.-N., T.-C. Wen, and Y. Chang. Zwitterionic surface grafting of epoxylated sulfobetaine copolymers for the development of stealth biomaterial interfaces. *Acta Biomater.* 40:78–91, 2016.
8. Gao, C., G. Li, H. Xue, W. Yang, F. Zhang, and S. Jiang. Functionalizable and ultra-low fouling zwitterionic surfaces via adhesive mussel mimetic linkages. *Biomaterials* 31:1486–1492, 2010.
9. Hanna, H. A., I. I. Raad, B. Hackett, S. K. Wallace, K. J. Price, D. E. Coyle, and C. L. Parmley. ANtibiotic-impregnated catheters associated with significant decrease in nosocomial and multidrug-resistant bacteremias in critically ill patients*. *Chest* 124:1030–1038, 2003.
10. James, M. T., J. Conley, M. Tonelli, B. J. Manns, J. MacRae, and B. R. Hemmelgarn. Meta-analysis: Antibiotics for Prophylaxis against Hemodialysis Catheter–Related Infections. *Ann. Intern. Med.* 148:596–605, 2008.
11. Jiang, S., and Z. Cao. Ultralow-Fouling, Functionalizable, and Hydrolyzable Zwitterionic Materials and Their Derivatives for Biological Applications. *Adv. Mater.* 22:920–932, 2010.
12. Kim, S. J., S. J. Park, and S. I. Kim. Swelling behavior of interpenetrating polymer network hydrogels composed of poly(vinyl alcohol) and chitosan. *React. Funct. Polym.* 55:53–59, 2003.
13. Kohnen, W., C. Kolbenschlag, S. Teske-Keiser, and B. Jansen. Development of a long-lasting ventricular catheter impregnated with a combination of antibiotics. *Biomaterials* 24:4865–4869, 2003.
14. Maki, D. G., D. M. Kluger, and C. J. Crnich. The Risk of Bloodstream Infection in Adults With Different Intravascular Devices: A Systematic Review of 200 Published Prospective Studies. *Mayo Clin. Proc.* 81:1159–1171, 2006.
15. Mermel, L. A., B. M. Farr, R. J. Sherertz, I. I. Raad, N. O'Grady, J. S. Harris, and D. E. Craven. Guidelines for the Management of Intravascular Catheter-Related Infections. *Clin. Infect. Dis.* 32:1249–1272, 2001.
16. Noimark, S., C. W. Dunnill, M. Wilson, and I. P. Parkin. The role of surfaces in catheter-associated infections. *Chem. Soc. Rev.* 38:3435–3448, 2009.
17. Park, H., X. Guo, J. S. Temenoff, Y. Tabata, A. I. Caplan, F. K. Kasper, and A. G. Mikos. Effect of Swelling Ratio of Injectable Hydrogel Composites on Chondrogenic Differentiation of Encapsulated Rabbit Marrow Mesenchymal Stem Cells In Vitro. *Biomacromolecules* 10:541–546, 2009.
18. Park, J. H., Y. W. Cho, Y.-H. Cho, J. M. Choi, H. J. Shin, Y. H. Bae, H. Chung, S. Y. Jeong, and I. C. Kwon. Norfloxacin-releasing urethral catheter for long-term catheterization. *J. Biomater. Sci. Polym. Ed.* 14:951–962, 2003.
19. Pholpabu, P., S. S. Yerneni, C. Zhu, P. G. Campbell, and C. J. Bettinger. Controlled Release of Small Molecules from Elastomers for Reducing Epidermal Downgrowth in Percutaneous Devices. *ACS Biomater. Sci. Eng.* , 2016.doi:10.1021/acsbiomaterials.6b00192
20. Raad, I., R. Darouiche, R. Hachem, M. Sacilowski, and G. P. Bodey. Antibiotics and prevention of microbial colonization of catheters. *Antimicrob. Agents Chemother.* 39:2397–2400, 1995.
21. von Recum, A. F. Applications and failure modes of percutaneous devices: A review. *J. Biomed. Mater. Res.* 18:323–336, 1984.
22. Zhang, L., Z. Cao, T. Bai, L. Carr, J.-R. Ella-Menye, C. Irvin, B. D. Ratner, and S. Jiang. Zwitterionic hydrogels implanted in mice resist the foreign-body reaction. *Nat. Biotechnol.* 31:553–556, 2013.
23. Zhang, L., Z. Cao, T. Bai, L. Carr, J.-R. Ella-Menye, C. Irvin, B. D. Ratner, and S. Jiang. Zwitterionic hydrogels implanted in mice resist the foreign-body reaction. *Nat. Biotechnol.* 31:553–556, 2013.

CHAPTER 6 CONCLUSIONS AND FUTURE OUTLOOK

6.1 Conclusions

Percutaneous devices are necessary in modern healthcare, serving a multitude of clinical purposes. However, they are prone to bacterial adhesion and induce epidermal downgrowth, leading to high risk of infection. Nosocomial catheter-related bloodstream infections are common in ICU patients, causing higher medical cost, longer hospital stay, morbidity and potential mortality. Current techniques and technology in applying and developing percutaneous devices are not enough to solve the problem in long term.[3,5] This thesis aims to design biomaterials in different perspectives to use in percutaneous devices.

In Chapter 3, we focus on surface topography to study cell responses in vitro. We describe a lithography-free approach to fabricate dynamic substrate topography for measuring morphodynamics of cells during contact guidance.[8] This work represents a strategy to better isolate the effect of dynamic programmable topography on living cells. Although we found that the topographic cues might not work for controlling the epidermal migration in percutaneous devices, the programmable substrate topography is a promising strategy to elucidate cytoskeleton remodeling dynamics in many cell phenotypes in the context of cell-biomaterials interactions.

In Chapter 4, we focus on macrophage modulation to reduce epidermal downgrowth. We design cylindrical percutaneous matrices that provide a controlled release of small molecules to alter macrophage expressions.[9] We deliberately

investigate the PGS-CinA matrices' mechanical and physical properties. Our results show that PGS-CinA exhibits suitable properties of biomaterials for percutaneous devices: (1) a Young's modulus in the elastomeric regime that matches that of the native epidermis; (2) a crosslinked polymeric networks with a mesh size that controls the release of small molecules; and (3) an attenuated fibrous capsule response. Also, CLA-eluting PGS-CinA matrices can increase the local density of M2 macrophages, and reduce dermal downgrowth and skin contraction. We suggest that CLA-eluting PGS-CinA elastomers represent a viable coating strategy to reduce epidermal downgrowth in percutaneous devices.

In Chapter 5, we focus on anti-fouling property of biomaterials. We fabricate zwitterionic percutaneous devices from polycarboxybetaine to investigate host responses comparing to PHEMA. Our preliminary results show that the mechanical properties of PCBMA hydrogels can be controlled by the initial concentrations of monomers and crosslinkers during preparation. For in vivo study, PHEMA with the higher modulus can reduce skin bridge contraction, compared to other hydrogels, over 20 d. The complete results will be reported when the histological analysis is done.

6.2 Future Outlook

Percutaneous devices are apparently still open for new biomaterial designs that provide strategies in reducing device-related infections. A huge number of attempts over the past decades have focused on modification of catheter surface by either coating or impregnation with antimicrobials or antiseptics.[7,10,11] Recently, zwitterionic materials

have attracted a multitude of biomaterial research. They are incorporated to a number of medical devices due to the fact that they can well resist non-specific protein adsorption which is a common theme for biomaterials.[1,2,6] Preparation procedures of zwitterionic materials are also uncomplicated and can yield products with different mechanical properties.[13] Particularly, the chemical structure of polycarboxybetaine provides many carboxyl groups that is easily functionalized, making it well-suited for applications that require anti-fouling materials and additional functional groups.[6] The trend suggests that zwitterionic coating technology might become dominant in the field of biomaterials.

Some research have recently reported an incorporation of anti-fouling coatings and antibiotics on surface of percutaneous devices.[4,12] The anti-fouling coatings can increase biocompatibility by resisting protein adsorption, while the antibiotics assist in killing bacteria. The bi-functional coating is currently under investigated in vitro, and still needs more profound information in in vivo environments. Multifunctional materials, e.g. anti-fouling and antimicrobial coating, potentially becomes main technology for percutaneous devices.

References:

1. Anderson, J. M., A. Rodriguez, and D. T. Chang. Foreign body reaction to biomaterials. Semin. Immunol. 20:86–100, 2008.
2. Campoccia, D., L. Montanaro, and C. R. Arciola. A review of the biomaterials technologies for infection-resistant surfaces. *Biomaterials* 34:8533–8554, 2013.
3. Criddle, J. M., R. A. Hieb, S. B. White, P. J. Patel, E. J. Hohenwalter, S. M. Tutton, and W. S. Rilling. Evaluation of catheter infection rates in converted dialysis catheters versus de novo placement in the setting of chlorhexidine use. *J. Vasc. Access* 17:162–166, 2016.
4. Ding, X., C. Yang, T. P. Lim, L. Y. Hsu, A. C. Engler, J. L. Hedrick, and Y.-Y. Yang. Antibacterial and antifouling catheter coatings using surface grafted PEG-b-cationic polycarbonate diblock copolymers. *Biomaterials* 33:6593–6603, 2012.

5. Großhauser, J., K. Reiter, C. Große-Siestrup, J. Kikhney, U. Kertzscher, and K. Affeld. Bionic approach for the prevention of exit-site infections of percutaneous devices. *Biomed. Eng. Biomed. Tech.* 60:, 2015.
6. Jiang, S., and Z. Cao. Ultralow-Fouling, Functionalizable, and Hydrolyzable Zwitterionic Materials and Their Derivatives for Biological Applications. *Adv. Mater.* 22:920–932, 2010.
6. Nickel, J. C., J. B. Wright, I. Ruseska, T. J. Marrie, C. Whitfield, and J. W. Costerton. Antibiotic resistance of Pseudomonas aeruginosa colonizing a urinary catheter in vitro. Eur. J. Clin. Microbiol. 4:213–218.
8. Pholpabu, P., S. Kustra, H. Wu, A. Balasubramanian, and C. J. Bettinger. Lithography-free fabrication of reconfigurable substrate topography for contact guidance. *Biomaterials* 39:164–172, 2015.
9. Pholpabu, P., S. S. Yerneni, C. Zhu, P. G. Campbell, and C. J. Bettinger. Controlled Release of Small Molecules from Elastomers for Reducing Epidermal Downgrowth in Percutaneous Devices. *ACS Biomater. Sci. Eng.* , 2016.doi:10.1021/acsbiomaterials.6b00192
10. Raad, I., R. Darouiche, R. Hachem, M. Sacilowski, and G. P. Bodey. Antibiotics and prevention of microbial colonization of catheters. *Antimicrob. Agents Chemother.* 39:2397–2400, 1995.
11. Ramritu, P., K. Halton, P. Collignon, D. Cook, D. Fraenkel, D. Battistutta, M. Whitby, and N. Graves. A systematic review comparing the relative effectiveness of antimicrobial-coated catheters in intensive care units. *Am. J. Infect. Control* 36:104–117, 2008.
12. Vaterrodt, A., B. Thallinger, K. Daumann, D. Koch, G. M. Guebitz, and M. Ulbricht. Antifouling and Antibacterial Multifunctional Polyzwitterion/Enzyme Coating on Silicone Catheter Material Prepared by Electrostatic Layer-by-Layer Assembly. *Langmuir ACS J. Surf. Colloids* 32:1347–1359, 2016.
13. Zhang, L., Z. Cao, T. Bai, L. Carr, J.-R. Ella-Menye, C. Irvin, B. D. Ratner, and S. Jiang. Zwitterionic hydrogels implanted in mice resist the foreign-body reaction. *Nat. Biotechnol.* 31:553–556, 2013.